CONTROLLING SUPEROSCILLATION BASED IMAGING WITH POLARIZATION AND COHERENCE

by

Rui Qi

A dissertation submitted to the faculty of
The University of North Carolina at Charlotte
in partial fulfillment of the requirements
for the degree of Doctor of Philosophy in
Optical Science and Engineering

Charlotte

2024

Approved by:

Dr. Gregory J. Gbur

Dr. Vasily Astratov

Dr. Thomas J. Suleski

ABSTRACT

RUI QI. Controlling Superoscillation Based Imaging with Polarization and Coherence. (Under the direction of DR. GREGORY J. GBUR)

Superoscillation is a physical phenomenon, in which the local oscillations of a band-limited signal fluctuate faster than the fastest Fourier component of the signal. In recent years, superoscillation had lead to a method of super-resolution imaging, named superoscillatory imaging, and it now plays an important role in many areas, such as remote sensing and biomedical research. This dissertation investigated a key lens element for achieving superoscillatory imaging. Then, a vector-superoscillatory field provided a solution to a major problem associated with superoscillatory imaging. Lastly, the partial coherence effect, specifically circular coherence, was studied for vortex beam propagation in free space and can be considered in the quality of super-oscillatory imaging.

This dissertation work began by studying the existing methods for designing filters to create superoscillatory fields in the image plane. A design method by Smith and Gbur tailors a superoscillatory field in two dimensions, from which a filter is calculated with both an amplitude profile and a phase profile (a complex filter). Accordingly, the first study of this dissertation aimed to simplify a complex filter into a filter with only one profile: an amplitude profile or a phase profile, which make the filters fabrication-friendly. This study derived the mathematical formula for generating simplified filter profiles (leading to the same superoscillatory field by complex filters). A step-by-step example of creating such simplified filters was demonstrated by following this approach. Performance criteria of the designed filters were discussed, including but not limited to energy efficiency. The designed phase-only filter showed an energy efficiency same as that of the complex filter.

The second study of this dissertation provided a method to eliminate the sidelobes

that are inevitable in superoscillatory fields and that causes problems in superoscillatory imaging. As light is a transverse electromagnetic wave, the orientation of scattering patterns of Rayleigh scatterers is polarization-dependent. Then, superoscillatory fields with two polarization states (referred to as vector superoscillatory fields) were created, so that the sidelobes can be avoided in the imaging process. This study proposed an imaging system with vector superoscillatory illumination. Super-resolved scattering images of Rayleigh scatterer patterns were simulated under a vector superoscillatory illumination, whose resolution surpassed those obtained from a conventional imaging system. A device was proposed for generating a vector-superoscillatory field.

Light sources with circular coherence have perfectly coherent points on any concentric rings of their transverse planes. In the third study, we investigated various properties of these beams, from their ability to carry optical vortices in free space to the self-focusing effect. Circular coherence was imposed onto vortex beams (with spiral phase structures). The free-space propagation of circularly coherent vortex beams showed that optical vortices remained their positions on free-space propagation and the beams revealed a focal region. This study also provided a model for propagating rotationally symmetric beams using two-dimensional Hankel transforms. The self-focusing effect of circular coherence can be considered for further reducing the spot size of a superoscillatory field.

These three studies together make the superoscillatory imaging technique more potential in implementation.

DEDICATION

To:

My dear parents

Wenquan Qi and Cailing Liu

My dear sister

Jingyi Qi

ACKNOWLEDGEMENTS

I would like to extend my gratitude to people who support my dissertation work:

I would like to express my deepest appreciation to Prof. Greg Gbur for his mentoring and patient instructions through numerous discussions. Prof. Gbur's creative ways of thinking and his open mind for allowing results to challenge existing findings and conventions have always inspired me. His enormous knowledge in physics and optics continuously helped me to improve this dissertation, not only in the research approach but also in the constructive suggestions for both contents and writing. In addition, I want to thank Prof. Gbur for his support during the global COVID-19 pandemic, which was an extremely difficult time for me. Prof. Gbur bore all the burdens by himself during the pandemic without saying a word and let me complete my dissertation.

I want to thank Prof. Astradov and Prof. Suleski who serve as committee members and Prof. Nguyen to serve as the graduate faculty representative.

Members in Prof. Gbur's group: Arash Shiri, Wenrui Miao, Ray Abney, Joseph May, Matt Smith, Elisa Hurwitz, and William Raburn for discussions and the friendship.

Renee Johnson and Kate Cruz for administrative support.

My parents, Wenquan Qi and Cailing Liu, and my sister, Jingyi Qi for all the love, support, and understanding to me.

Finance support from GASP fund, Air Force Office of Scientific Research (Grant No. FA9550-21-1-0171), Office of Naval Research (MURI N00014-20-1-2558), GSSF fellowship, and Frontiers in Optics travel fund.

TABLE OF CONTENTS

LIST OF TABLES xii

LIST OF FIGURES xiii

LIST OF ABBREVIATIONS xx

CHAPTER 1: INTRODUCTION 1

1.1. Resolution of Imaging Systems 1

1.2. Existing Super-resolution Imaging Techniques 4

1.2.1. Confocal microscopy 4

1.2.2. Fluoresence microscopy 5

1.2.3. Near field microscopy 5

1.2.4. Polarization techniques for super-resolution imaging 6

1.2.5. Label-free super-resolution microscopy 8

1.2.6. Other super-resolution techniques 9

1.3. Superoscillation Theories 10

1.3.1. Electromagnetism of antennas and super-resolution imaging 11

1.3.2. The first superoscillation 13

1.3.3. Simple mathematical methods of superoscillation 13

1.3.4. Prolate spheroidal wave functions and superoscillation 17

1.4. Superoscillation for Imaging Application 18

1.4.1. Optical superoscillation 18

1.4.2. Superoscillation-based super-resolution imaging 19

1.5. Spatial Coherence and Image Resolution 20

1.5.1. Coherence effect in imaging 21

1.5.2. Superoscillation in coherence condition 22

1.6. Chapter Overviews 22

CHAPTER 2: SIMPLIFIED SUPEROSCILLATORY LENSES 24

2.1. Introduction 24

2.2. Complex Filter 26

2.2.1. Amplitude and phase profile 26

2.2.2. Superoscillatory image field 29

2.2.3. Estimation of the minimum number of pixels 31

2.3. Amplitude-only Filtering Device 32

2.3.1. Amplitude profile 33

2.3.2. Superoscillatory image field 35

2.4. Phase-only Filtering Device 38

2.4.1. Phase profile 38

2.4.2. Superoscillatory image field 42

2.4.3. Estimation of the minimum number of pixels 47

2.5. Step-wise Phase-only Filtering Device 48

2.5.1. Phase profile 48

2.5.2. Superoscillatory image field 50

2.6. Comparison Between the Designed Filters 51

2.6.1. Complex filter 51

2.6.2. Amplitude-only filter 52

2.6.3. Phase-only filter 53

2.7. Discussion and Conclusion 55

CHAPTER 3: VECTOR SUPEROSCILLATORY FIELD ILLUMINATION 58

3.1. Introduction 58

3.2. Transverse Nature and Polarization of Light 58

3.2.1. Direction of polarization 59

3.2.2. Stokes parameters 60

3.2.3. Jones vector and matrix 61

3.3. Rayleigh Scattering and Concept of Sidelobe Suppression 62

3.3.1. Polarization dependence of Rayleigh scattering 62

3.3.2. Sidelobe suppression under vector field illumination 62

3.4. A Super-resolution System with Vector Superoscillatory Field Illumination 64

3.5. Images with Vector Superoscillatory Field Illumination 65

3.5.1. Foldy-Lax method for calculating multi-scattering 65

3.5.2. Scattering pattern of a single scatterer 68

3.5.3. Super-resolved images of Rayleigh scatterer patterns 69

3.5.4. Factors affecting super-resolved image quality 72

3.6. Creation of Vector Superoscillatory Field 75

3.6.1. Vector superoscillatory field in image plane 76

3.6.2. Vector field in aperture plane 77

3.6.3. Calculation of polarization distribution in aperture 78

3.6.4. Device for generating vector superoscillatory field 80

3.7. Discussion and Conclusion 82

CHAPTER 4: CIRCULARLY COHERENT VORTEX BEAMS 84

4.1. Introduction 84

4.2. Partial Coherence and Optical Vortices 84

4.2.1. Second-order coherence properties 84

4.2.2. Coherent optical vortex 86

4.2.3. Optical vortices in partially coherent fields 87

4.3. Circularly Coherent Vortex Beam at Source Plane 88

4.3.1. Creation of circularly coherent vortex beam 88

4.3.2. Spectral degree of coherence 89

4.3.3. Cross-spectral density 90

4.3.4. Amplitude and phase under a fixed observing point 91

4.4. Paraxial Propgation of Circularly Coherent Vortex Beam 93

4.4.1. Cross-spectral density 93

4.4.2. Spectral degree of coherence 96

4.4.3. Amplitude and phase under a fixed observing point 98

4.5. Self-focusing Effect of Circular Coherence 101

4.5.1. Self-focusing of circularly coherent vortex beams 101

4.5.2. Self-focusing of superimposed LG±04 beams 102

4.5.3. Comparison of focal regions by a lens and a circular coherence beam 103

4.5.4. Focal spot of superimposed circularly coherent LG±04 beams 104

4.6. Experiment for Measuring Circularly Coherent Vortex Beams 106

4.7. Discussion and Conclusion 108

CHAPTER 5: SUMMARY AND FUTURE WORK 110

5.1. Summary 110

5.2. List of Contributions 111

5.3. List of Related Publications 112

5.4. Future Work 112

REFERENCES 114

APPENDIX A: DERIVATION OF TWO-DIMENSIONAL INTENSITY DISTRIBUTION AT THE IMAGE PLANE 121

APPENDIX B: SCATTERING CALCULATION WITH FOLDY-LAX METHOD FOR THREE PARTICLES 125

APPENDIX C: VECTOR FIELD TRANSMITTED BY A LIQUID CRYSTAL CELL 131

APPENDIX D: DERIVATION OF A FAR-FIELD CSD 134

APPENDIX E: FAR-FIELD CSD WITH LEVIN METHOD 136

APPENDIX F: SPECTRAL DENSITY PROFILE WITH NUMERICAL HANKEL TRANSFORM 139

LIST OF TABLES

TABLE 2.1: **Energy efficiency of the complex filter** 52

TABLE 2.2: **Energy efficiency of the designed amplitude-only filter** 53

TABLE 2.3: **Energy efficiency of the designed phase-only filter** 54

LIST OF FIGURES

FIGURE 1.1: A lens system with parameters that describe (a) a diffraction-limited spot and (b) the Rayleigh criterion. 3

FIGURE 1.2: A confocal microscopy system. 4

FIGURE 1.3: Experimental conditions for achieving (a) TIR and (b) Frustrated TIR. 6

FIGURE 1.4: Focal region of fields of (a) radially polarized beam leading to a longitudinally polarized focal spot and (b) azimuthally polarized beam leading to an on-axis none. 7

FIGURE 1.5: A plasmonic structured illumination microscopy system. 8

FIGURE 1.6: Relation between (a) geometric pattern of an antenna array and (b) the field of the antenna array on a complex plane. The root, z_n, also lie on the unit circle in the complex plane. The field, z, is located in the range of the orange arc on the unit circle with the length determined by the configurations of the antenna array. The super-gain antennas theory suggests that by squeezing the roots into a shorter arc of the unit circle, the antennas field can have a narrower peak. 12

FIGURE 1.7: Superoscillatory waveform by moving first two zero rings closer. (a) $f(x)$ before moving first two zero rings closer, (b) $g(x)$, with superoscillatory waveform, by moving first two zero rings of $f(x)$ closer and (c) $g(x)$ under zoomed in condition. 15

FIGURE 1.8: Superoscillations created by product of polynomials with their zeros and an envelope function: (a) an envelope function, $e(t)$, (b)superoscillatory waveform, and (c) the superoscillatory region after zooming in. 16

FIGURE 1.9: Prolate spheroidal functions forming superoscillatory waveforms: (a) angular spheroidal wave functions, (b) superoscillatory waveform by linear combination of angular spheroidal wavefunctions. 17

FIGURE 1.10: Real and imaginary parts of $f(x)$ of (a) $a = 5$, (b) $a = 5$ under zoomed in condition, (c) $a = 20$, and (d) $a = 20$ under zoomed in condition, with $\mathrm{N} = 10$. 19

FIGURE 2.1: Experimental setup for obtaining the transmittance of a superoscillatory filter: (a) a superoscillatory filter, (b) a lens, and (c) a detector. The orange lines show the wavefront of the optical field 26

FIGURE 2.2: A superoscillatory field (radius, r_{spot}=0.94λ) located in the center of large sidelobes: (a) a cross-sectional view and (b) a top view. 28

FIGURE 2.3: Designed transmittance of a complex filter: (a) cross-sectional amplitude, (b) cross-sectional phase, (c) three-dimensional amplitude, and (d) three-dimensional phase, with $M = 151$, $\Delta x = 0.4\,\text{mm}$. 29

FIGURE 2.4: Image spots formed by (a) a regular lens (r_{spot}=1.46λ), (b) a complex filter with the same aperture size of the regular lens (r_{spot}=0.94λ), (c) the amplitude profile of the complex filter ($r_{\text{spot}}\approx$1.46λ), (d) the phase profile of the complex filter ($r_{\text{spot}}\approx$1.46λ); and comparison of spots with intensity normalized at the central peak (e), with $M = 151$, $\Delta x = 0.4\,\text{mm}$. 30

FIGURE 2.5: Complex filter transmittance with different pixel numbers and the corresponding superoscillatory fields: (a) amplitude transmittance with $M = 11$, $\Delta x = 5.7\,\text{mm}$, and the corresponding (b) superoscillatory field, and (c) amplitude transmittance with $M = 31$, $\Delta x = 2\,\text{mm}$, and the corresponding (d) superoscillatory field. 32

FIGURE 2.6: Proposed system for creating superoscillatory field with an amplitude-only filter: (a) an amplitude-only filter, (b) a lens, and (c) a detector. 33

FIGURE 2.7: Designed amplitude of an amplitude-only filter, with $\alpha_0 = 0$, $\Delta\alpha = 1$, $\beta = 1$, $a = 284\ \text{m}^{-1}$, $M = 151$, and $\Delta x = 0.4\,\text{mm}$, (a) one-dimensional amplitude profile and (b) three-dimensional amplitude profile. 35

FIGURE 2.8: Intensity distribution of a superoscillatory field in the image plane formed by an amplitude-only filter with $\alpha_0 = 0$, $\Delta\alpha = 1$, $\beta = 1$, $a = 284\,\text{m}^{-1}$, $M = 151$, and $\Delta x = 0.4\,\text{mm}$: (a) cross-sectional profile in full scale, (b) perspective view in full scale, (c) cross-sectional profile of a truncated 0^{th} order and $\pm1^{\text{st}}$ orders, (d) top view of a truncated 0^{th} order and $\pm1^{\text{st}}$ orders, and (e) top view of 1^{st} order, with (r_{spot}=0.94λ). 37

FIGURE 2.9: Proposed system for creating a superoscillatory field with a phase-only filter: (a) a phase-only filter, (b) a lens, and (c) a detector. 38

FIGURE 2.10: Phase of the designed phase-only filter, with $\Delta x = 2$ mm, $M = 31$, $b = 1$, and $a = 3116.5$ mm^{-1}, (a) one-dimensional phase profile, (b) three-dimensional phase profile, (c) three-dimensional phase profile within (-10,10) mm, and (d) three-dimensional phase profile within (-5,5) mm. 41

FIGURE 2.11: Setup and parameters for the window Fourier transform. 42

FIGURE 2.12: Reproduced superoscilllatory field by a phase-only filter with (a) $M = 31$, $\Delta x = 2$ mm, $b = 1$ and (b) $M = 61$, $\Delta x = 1$ mm, $b = 1$; with superoscillatory spot size, r_{spot}=0.94λ. 44

FIGURE 2.13: Superoscillatory field formed by a phase-only filter in the image space with (a) M=31, $\Delta x = 2$ mm, b=1 in two dimensions and (b) in one dimension, (c) M=31, $\Delta x = 1$ mm, b=2 in two dimensions, and (d) in one dimensio; with 0^{th} order superoscillatory spot size, r_{spot}=0.94λ. 46

FIGURE 2.14: A wide superoscillatory field formed by a phase-only filter in the image space with $M = 31$, $\Delta x = 2$ mm, $b = 1$ in one dimension. 47

FIGURE 2.15: Phase-only filter with (a) smooth sinusoidal phase profile of $M = 31$, $\Delta x = 2$ mm, $b = 1$, (b) step-wise phase profile of 9 steps in each sinusoidal period, (c) smooth sinusoidal phase profile zoomed in for the central area, and (d) step-wise phase profile of 9 steps in each sinusoidal period zoomed in for the central area. 49

FIGURE 2.16: Three orders of superoscilllatory field formed by a step-wise phase-only filter in two-dimensional image space with $M = 31$, $\Delta x = 2$ mm, and $b = 1$; with superoscillatory spot size, r_{spot}=0.94λ. 50

FIGURE 2.17: Cross section ($y' = 0$) of superoscillatory field formed by a step-wise phase-only filter of (a) three orders, (b) the 1^{st} order and the 2^{nd}, with $M = 31$, $\Delta x = 2$ mm, and $b = 1$. 51

FIGURE 2.18: Energy efficiency distribution of phase-only filters with different order to carry superoscillatory field, with $M = 151$, $\Delta x = 0.4$ mm 55

FIGURE 3.1: Polarization-dependent Rayleigh scattering pattern: scattering pattern of a scatterer by interacting with an electromagnetic wave. 63

FIGURE 3.2: Scattering patterns of scatterers under the illumination of the central spot and the sidelobes in a superoscillatory field with orthogonal linear polarization states. 64

FIGURE 3.3: A proposed super-resolution imaging system, with (a) the front view and (b) the perspective view. 65

FIGURE 3.4: Scattering of two Rayleigh particles 66

FIGURE 3.5: Images of Rayleigh scatterers under different illumination conditions: (a) ground truth of a single scatterer ($a = 50\,\text{nm}$=0.1λ and $n = 1.5$), (b) $\langle \boldsymbol{S} \rangle_x$ of the scatterer illuminated by a VSF, and (c) $\langle \boldsymbol{S} \rangle_x$ as illuminated by a superoscillatory field polarized in y direction; with superoscillatory spot radius, $\mathrm{r_{sp}} = 0.94\lambda$. 69

FIGURE 3.6: Images of Rayleigh scatterers under different illumination conditions: (a) ground truth of two scatterers separated by $d_0 = 610\,\text{nm}$, (b) $\langle \boldsymbol{S} \rangle_x$ of the two scatterers illuminated by a VSF with $r_s = 470\,\text{nm}$=0.94λ, and (c) $\langle \boldsymbol{S} \rangle_x$ when illuminated by the diffraction-limited spot with $r_d = 732\,\text{nm}$=1.46λ. 70

FIGURE 3.7: Images of Rayleigh scatterers under different illumination: (a) ground truth of five scatterers with a "Λ" shape ($a = 50\,\text{nm}$=0.1λ, $n = 1.5$, and $d_0 = 610\,\text{nm}$=1.22λ) (b) $\langle \boldsymbol{S} \rangle_x$ of the scatterers illuminated by a VSF, and (c) $\langle \boldsymbol{S} \rangle_x$ of the scatterers illuminated by a diffraction-limited spot. 71

FIGURE 3.8: Images of Rayleigh scatterers under different illumination: (a) ground truth of nanoparticles with different shapes,with n=1.5, (b) $\langle \boldsymbol{S} \rangle_x$ of the scatterers illuminated by a VSF, and (c) $\langle \boldsymbol{S} \rangle_x$ as illuminated by a diffraction-limited spot. 72

FIGURE 3.9: Images of Rayleigh scatterers under different illumination: (a) $\langle \boldsymbol{S} \rangle_x$ as illuminated by the VSF for five scatterers with a refractive index ratio of $n_1 : n_2 : n_3 : n_4 : n_5 = 1 : 2 : 3 : 4 : 1$ and (b) $\langle \boldsymbol{S} \rangle_x$ as illuminated by the VSF for five scatterers with a size of $a = 200\,\text{nm}$=0.4λ. 73

FIGURE 3.10: Multi-scattering due to scatterers pattern: $\langle \boldsymbol{S} \rangle_x$ of five scatterers with a cross shape illuminated by a VSF; scatterers' size and refractive index are the same as those of the Λ system. 74

FIGURE 3.11: Imaging system and an obtained image with a detector facing y direction: (a) experimental setup and (b) $\langle \boldsymbol{S} \rangle_x$ of five scatterers illuminated by a VSF. 75

FIGURE 3.12: Vector superoscillatory field in the image plane: (a) amplitude of $\boldsymbol{E}'_x(\boldsymbol{r}_\mathrm{I})$, (b) phase of $\boldsymbol{E}'_x(\boldsymbol{r}_\mathrm{I})$, (c) amplitude of $\boldsymbol{E}'_y(\boldsymbol{r}_\mathrm{I})$, and (d) phase of $\boldsymbol{E}'_y(\boldsymbol{r}_\mathrm{I})$. 77

FIGURE 3.13: Vector field in the aperture plane: (a) amplitude of $\boldsymbol{E}_x(\boldsymbol{r}_\mathrm{L})$, (b) phase of $\boldsymbol{E}_x(\boldsymbol{r}_\mathrm{L})$, (c) amplitude of $\boldsymbol{E}_y(\boldsymbol{r}_\mathrm{L})$, and (d) phase of $\boldsymbol{E}_y(\boldsymbol{r}_\mathrm{L})$. 78

FIGURE 3.14: Polarization states in the aperture plane. 79

FIGURE 3.15: Orientation angle in the aperture plane in the range of (a) [-π/2,π/2] and (b) [0,2π]. 80

FIGURE 3.16: Rotation of polarization states by liquid crystal cells. 82

FIGURE 4.1: Amplitude and phase profiles of LG beams with an azimuthal order of (a) $m=1$ and (b) $m=3$, with $\sigma_s=0.02\,\mathrm{m}$. 87

FIGURE 4.2: Component fields of $H(\mathbf{r},v)$ with different radii of curvatures: (a) v<0, (b) v=0, and (c) v>0. 88

FIGURE 4.3: Absolute spectral degree of coherence,$\mu(r_1,r_2)$, of (a) a circularly coherent source, with $\delta_\mu=0.044\,\mathrm{m}$,(b) with perfect coherence along any ring concentric to the beam axis. 90

FIGURE 4.4: CSDs of circularly coherent LG beams at the source plane: CSD as function of r_1 and r_2, with an azimuthal order of $m=0$, $m=1$, and $m=3$, with $\sigma_s=0.02\,\mathrm{m}$ and $\delta_\mu=0.044\,\mathrm{m}$. 91

FIGURE 4.5: Circularly coherent LG beams at the source plane: (a) amplitude , and (c) phase of CSDs under a fixed observing point, r_1, with an azimuthal order of $m=0$, $m=1$, and $m=3$, with $\sigma_s=0.02\,\mathrm{m}$ and $\delta_\mu=0.044\,\mathrm{m}$. Observing points are $r_1=0.18\,\mathrm{mm}$, $0.27\,\mathrm{mm}$, and $0.44\,\mathrm{mm}$, respectively. 92

FIGURE 4.6: Cross-spectral densities of circularly coherent LG beams on propagation with an azimuthal order of m=0, m=1, and m=3, with $\sigma_s=0.02\,\mathrm{m}$, $\delta_\mu=0.044\,\mathrm{m}$, and $\lambda=632.8\,\mathrm{nm}$ at the source plane, $1\,\mathrm{km}$, $2\,\mathrm{km}$, and $3\,\mathrm{km}$, respectively. 95

FIGURE 4.7: Spectral degree of coherence of circularly coherent LG beams on propagation with an azimuthal order of m=0, m=1, and m=3, with $\sigma_s = 0.02\,\mathrm{m}$, $\delta_\mu = 0.044\,\mathrm{m}$, and $\lambda = 632.8\,\mathrm{nm}$ at the source plane, 1 km, 2 km, and 3 km, respectively. 97

FIGURE 4.8: Amplitude of CSDs of circularly coherent LG beams on propagation with an azimuthal order of m=0, m=1, and m=3 under a fixed observing point, r_1, with $\sigma_s = 0.02\,\mathrm{m}$, $\delta_\mu = 0.044\,\mathrm{m}$, and $\lambda = 632.8\,\mathrm{nm}$ at the source plane, 1 km, 2 km, and 3 km, respectively. Observing points are $r_1 = 0.18\,\mathrm{mm}$, $0.27\,\mathrm{mm}$, and $0.44\,\mathrm{mm}$, respectively. 99

FIGURE 4.9: Phase of CSDs of circularly coherent LG beams on propagation with an azimuthal order of m=0, m=1, and m=3 under a fixed observing point, r_1, with $\sigma_s = 0.02\,\mathrm{m}$, $\delta_\mu = 0.044\,\mathrm{m}$, and $\lambda = 632.8\,\mathrm{nm}$ at the source plane, 1 km, 2 km, and 3 km, respectively. Observing points are $r_1 = 0.18\,\mathrm{mm}$, $0.27\,\mathrm{mm}$, and $0.44\,\mathrm{mm}$, respectively. 100

FIGURE 4.10: Propagation profiles of (a) coherent LG01, (b) circularly coherent LG01, and (c) coherent LG03, and (d) circularly coherent LG03, with $\sigma_s = 0.02\,\mathrm{m}$ and $\delta_\mu = 0.044\,\mathrm{m}$. 101

FIGURE 4.11: Comparison of (a) intensity of a coherent beam and (b) spectral density of the beam with circular coherence, constructed by the superposition of LG beams with an azimuthal order of $m = 4$ and $m =$ -4, with $\sigma_s = 0.02\,\mathrm{m}$, $\delta_\mu = 0.044\,\mathrm{m}$, and $\lambda = 632.8\,\mathrm{nm}$, propagating from the source plane upto 3 km. 102

FIGURE 4.12: Comparison of focal regions of (a) a coherent beam focused by a lens and (b) a self-focusing circular coherence beam, with $\delta_\mu = 0.0017\,\mathrm{m}$, and $\lambda = 632.8\,\mathrm{nm}$. 104

FIGURE 4.13: Comparison of focal regions of (a) the superposition of coherent LG$\pm$04 beam focused by a lens and (b) self-focusing circularly coherent counterpart beam, with $\delta_\mu = 0.0025\,\mathrm{m}$, and $\lambda = 632.8\,\mathrm{nm}$. 105

FIGURE 4.14: Experiment setup for measuring circularly coherent vortex beams. A circularly coherent field is created by (a) a laser and (b) a moving lens and a fixed lens and reflected by (c) a SLM to impose the circular coherence upon a vortex beam. The circularly coherent vortex beam goes through (d) a Young's pinhole mask with adjustable pinholes to measure the spectral degree of coherence of any concentric rings. The interference fringe is projected by (e) an objective onto (f) a CCD. 107

FIGURE B.1: Construction of a G matrix 128

FIGURE C.1: Relation between U and E_x and E_y. 132

LIST OF ABBREVIATIONS

CSD cross-spectral density

EM electromagnetic

FFT fast Fourier transform

LG Laguerre-Gauss

NA numerical aperture

OPD optical path difference

PSF point spread function

STED stimulated emission depletion

STORM stochastic optical reconstruction microscopy

TIR total internal reflection

TIRM total internal reflection microscopy

VSF vector superoscillatory field

CHAPTER 1: INTRODUCTION

Super-resolution optical imaging, which permits observers to visualize subwavelength features of objects, plays an important role in pure scientific investigations as well as applications such as medical imaging and diagnosis. For decades, tremendous efforts have been made to enhance the resolution of imaging systems. This thesis is focused on utilizing the phenomenon of superoscillations to perform super resolution imaging, which is referred to as superoscillatory imaging. The goal of this thesis is to investigate methods to achieve super-resolution imaging based on the superoscillation technique under specified polarization and partial coherence conditions.

In the introduction, the Rayleigh criterion that characterizes the resolution of imaging systems is explained, and a significant amount of research conducted in super-resolution imaging is reviewed. Although it is impossible to discuss all approaches, the principles of major technologies on super-resolution imaging are described in this thesis. A summary of theories of superoscillation using various mathematical approaches and levels of complexity are provided, and previous studies on utilizing polarization techniques and partial coherence to achieve super-resolution are reviewed.

1.1 Resolution of Imaging Systems

The resolution of an imaging system is defined as its ability to resolve two separated points. Both lens systems and detectors affect resolutions; however, this thesis focuses on lens systems-related resolution.

As a light field passes through a lens system, the image of a point object evolves into a spread of light, instead of a point, due to the diffraction and aberrations of the wavefront. The distribution of the spread of light defines a point spread function

(PSF). For a lens system with a circular aperture and without aberrations, the PSF is an Airy disk. The central spot of an Airy disk is called the diffraction-limited spot, which provides the measure of optical resolution, referred to as the Rayleigh criterion. This criterion was proposed by Lord Rayleigh as [1]

$$\theta_{\min} = 1.22\frac{\lambda}{D}, \tag{1.1}$$

where λ is the wavelength of light field, D is the diameter of the aperture stop, and $\theta_{\min}$ is the angular separation between two resolvable points on the image. According to Eq. (1.1), the minimal resolvable angular separation lies between two Airy disks with the center of one Airy disk overlapping the first zero intensity of the other. Unfortunately, for a traditional lens system, two image points with angular separation smaller than $\theta_{\min}$ cannot be resolved. However, with super-resolution techniques, this Rayleigh criterion can be beaten. Fig. 1.1 shows the lens system parameters that describe the diffraction-limited spot and Rayleigh criterion. Fig.1.1a shows a diffraction-limited spot generated by a traditional lens system. As shown in Fig. 1.1b, the minimum spatial separation of two image points, $d_{\min}$, is the radius of the first zero ring a diffraction-limited spot.

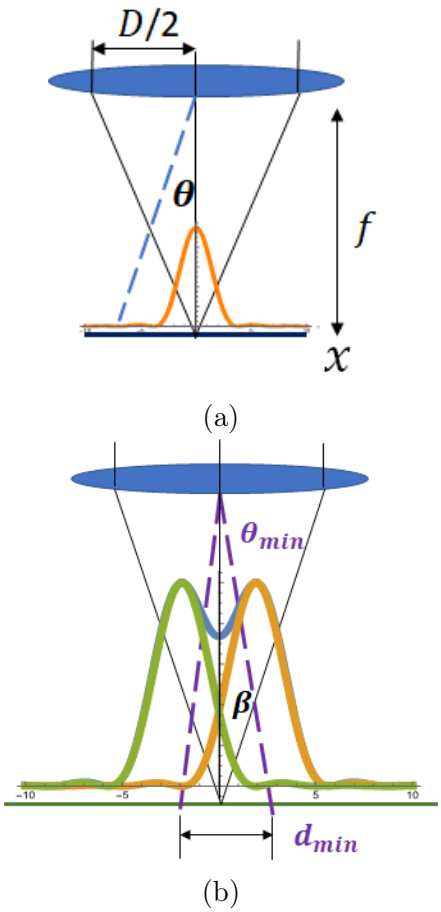

Figure 1.1: A lens system with parameters that describe (a) a diffraction-limited spot and (b) the Rayleigh criterion.

Although there are many factors in a lens system affecting the resolving power, the formula of resolution limit, proposed by Ernst Abbe, reveals that the resolution is ultimately limited by diffraction and is inversely proportional to the aperture size [2]:

$$d = \lambda/(2\mathrm{NA}), \tag{1.2}$$

where NA is the numerical aperture (NA) of the system. In terms of the relation between the Rayleigh criterion and the Abbe condition, the former defines a quantity to quantify the resolution of any imaging system which can be slightly modified and used by modern imaging systems. The latter demonstrates that it is the wavelength and the numerical aperture that eventually limit the resolution of traditional lens

systems, which might apply to modern imaging systems.

1.2 Existing Super-resolution Imaging Techniques

To surpass the diffraction limit, several super-resolution methods have been developed in the field of microscopy and have been widely applied. We review some of the most popular of these methods here.

1.2.1 Confocal microscopy

It is observed that when a detector is aimed at a single point of a three-dimensional specimen, the rays of light deflected or scattered from other points are also detected. Accordingly, an approach is needed to remove those rays that are not originally aimed at the point of interest [3]. This idea led to the invention of confocal microscopy and scanning confocal microscopy by Marvin Minsky in 1955. It applies a pinhole aperture-objective lens set in front and back of a specimen, respectively, to remove the extraneous rays and beat the Rayleigh criterion [3]. Fig. 1.2 shows a confocal microscopy system, in which pinholes are applied to eliminate the extraneous rays.

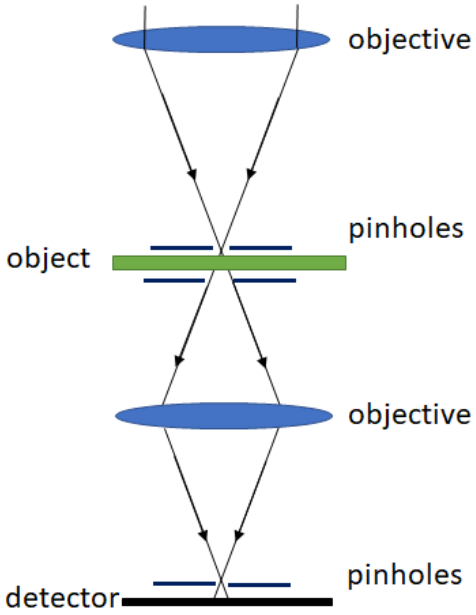

Figure 1.2: A confocal microscopy system.

1.2.2 Fluoresence microscopy

The idea of the confocal microscopy also led to the invention of super-resolution fluorescence microscopy, such as stimulated emission depletion (STED) microscopy and stochastic optical reconstruction microscopy (STORM). In addition to adding the pinholes as in confocal microscopy, these fluorescence microscopy techniques eliminate the scattered light from other points by using the molecules' nonlinear responses to light. STED microscopy is based on a two-photon excitation technique, which creates a narrower PSF by overlapping two separated photon-induced regular PSFs [4]. In practical setups, STED fluorescence scanning microscope applies an additional high intensity laser beam to inhibit the fluorescence in the outer stimulated region based on a nonlinear effect [5]. The STORM technique turns on a portion of the fluorophores at a specific time, without overlapping with fluorescence from the turned-off neighboring parts [6].

All these fluorescence microscopies are far field microscopies that can create three-dimensional images. Accordingly, the reconstruction of the image of the whole fluorophores is needed by the STORM technique. However, they also have disadvantages: for example, the two-photon excitation used by the STED technique may cause larger sidelobes in the PSF as the central peak becomes narrower and the high intensity laser might damage the tissue.

1.2.3 Near field microscopy

Another technique, based on the idea of coupling evanescent waves, is called near field microscopy. An evanescent wave is a wave that is closely bound to an interface between materials and propagates along the surface, such as produced in total internal reflection. The amplitude of an evanescent wave drops exponentially as it propagates away from the surface; thus, it cannot be detected more than a few wavelengths away. According to the theory of Fourier optics, the lack of angular spectrum components

in the detecting field (with their direction cosines in the transverse plane satisfying $\alpha^2 + \beta^2 > 1$, which correspond to evanescent waves), is the fundamental reason why imaging systems have limited resolutions. To solve the problem, near field microscopy introduces a probe very close to the object's surface to couple some evanescent waves into the probe or scatter them to the far field for measurement [7].

Total internal reflection microscopy (TIRM), a little different from near field microscopy, explicitly uses a physical phenomenon, referred to as a frustrated total internal reflection (TIR), to capture an evanescent wave produced by TIR for measurement. Fig. 1.3 shows the experimental conditions to obtain a TIR and a frustrated TIR. However, it is difficult to accurately build the experimental setup and conduct the scanning robustly. Also, this technique cannot be used to measure three-dimensional structures. In recent years, lenses made of metamaterials with negative refractive index have been created to cancel the decay of evanescent waves [8].

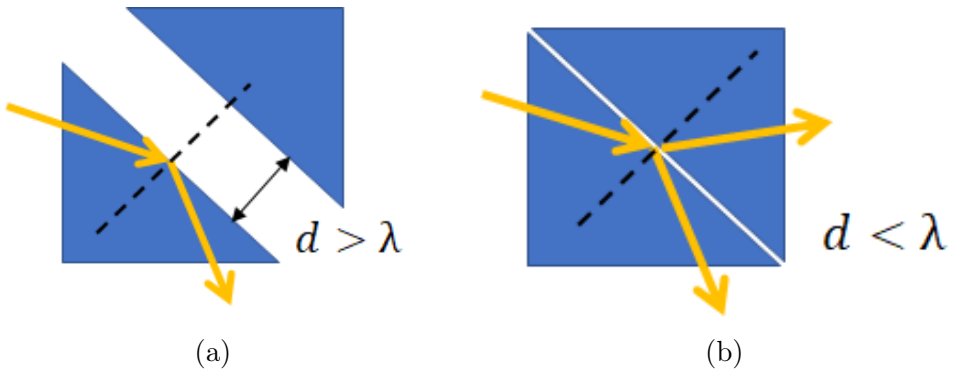

Figure 1.3: Experimental conditions for achieving (a) TIR and (b) Frustrated TIR.

1.2.4 Polarization techniques for super-resolution imaging

Most studies of superoscillations look at scalar waveforms, even though light is a transverse vector wave. However, for a system with very high NA (NA<1), the field distribution at the image plane cannot be well approximated by using Fourier analysis. Instead, the vector nature of the focused beams becomes significant. Youngworth

and Brown showed that a radially polarized beam leads to a focal region consisting of an on-axis longitudinal field and an anulus-shaped transverse field (radially polarized). In contrast, the azimuthally polarized beam only leads to an anulus-shaped transverse field (azimuthally polarized) with an on-axis null, for high NA cylindrical-vector beams [9]. Fig. 1.4 shows the focal region fields of radially polarized beam and azimuthally polarized beam.

Subsequently, a series of studies developed methods to create a sub-wavelength focus by using radially polarized beams, under the condition of high NA [10, 11, 12, 13]. For example, a radially polarized vortex beam can lead to nonzero on-axis intensity [14]. By modulating the longitudinal focal spot by using polarization, phase, and amplitude pupil masks, the spot size is further reduced [15]. However, this technique only provides super-resolution in one dimension.

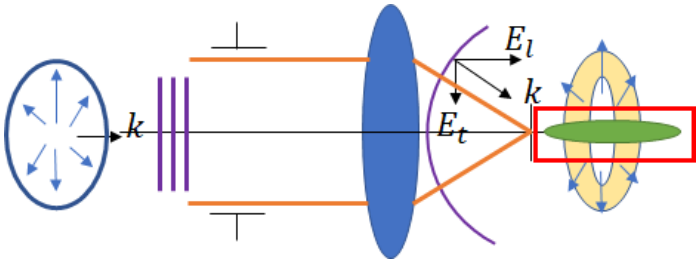

(a)

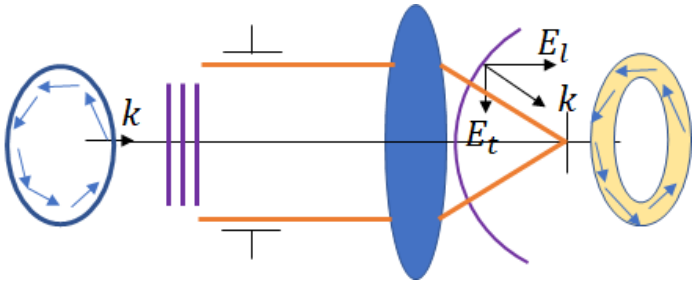

(b)

Figure 1.4: Focal region of fields of (a) radially polarized beam leading to a longitudinally polarized focal spot and (b) azimuthally polarized beam leading to an on-axis none.

1.2.5 Label-free super-resolution microscopy

Label-free microscopy is a type of microscopy technique, in which imaging signals are light scattered by nanostructures of objects, instead of fluorescence of stained fluorophores. Several methods have pushed the resolution of label-free microscopy beyond the Rayleigh criterion, named label-free super-resolution (LFSR) imaging. In deep learning based super-resolution microscopy, high resolution images can be reconstructed from multiple scattering images at different distances under different illumination conditions by using an inverse problem solver. The reconstruction of high-resolution images is also performed by trained neural network based artificial intelligence using large physical or virtual image datasets with high resolution [16, 17].

Plasmonic structured illumination microscopy is another technique, which has achieved super-resolution and might be applied for LFSR by utilizing metamaterials and interference [18]. In one of the studies, plasmonic structures, which consist of narrow Ag slit arrays made by a lithography technique (7.6 μm period), generate surface plasma with a wavenumber greater than that of structured illumination. In the experiment, fluorescent beads are placed on top of the plasmonic structures as objects, as shown in Figure 1.5.

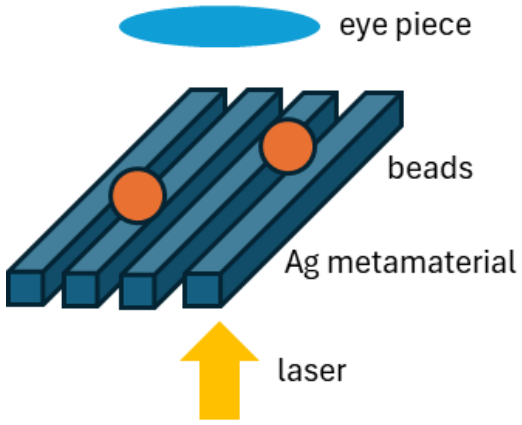

Figure 1.5: A plasmonic structured illumination microscopy system.

Solid immersion lens (SIL) is a kind of lens, which is created by immersing several

layers of dielectric nano particles in liquid, is applied to reduce the diffraction-limited spot size of label-free microscopy [19]. Another type of lens (named micro-spherical superlens), which attaches dielectric microspheres to objects, has experimentally demonstrated higher resolution than that of SIL. The experimental apparatus is simpler than those of other LFSR microscopy techniques, such as plasmonic structured illumination microscopy. These dielectric microspheres typically have large focusing power, and a higher refractive index can further enhance the resolution of super-resolved images [20, 21, 22].

More studies and methods on label-free microscopy for super-resolution imaging are detailed in a review paper and the book of "Label-Free Super-Resolution Microscopy" for further reading [23, 24].

1.2.6 Other super-resolution techniques

Another idea for improving resolution is to predict positions of image points by using statistical models. In early studies, the PSFs were approximated by Gaussian functions from which the positions of image points were predicated by a least-square estimator [25]. Later, PSFs, approximated by Airy functions, were used as inputs of a statistical estimator based on maximum-likelihood for predicting an ideal image, resulting in better accuracy [26]. This approach has been extended to reconstruct high resolution images through atmospheric turbulence, which typically distorts an image [27].

Similar to this idea, Fisher information has been applied as a statistical tool to estimate the separation of two spatially incoherent sources, and it has been combined with quantum metrology to achieve super-resolution imaging for incoherent point sources [28]. In general, a process to form an image from multiple measurements (reconstruction) is necessary for this approach.

Super-resolution imaging is also investigated in phase space [29]. The space bandwidth information of an imaging system can be presented in phase space, such as

Wigner space. In phase space, multiple parameters related to a system, such as spatial resolution, spectral bandwidth, and field of view, are considered as a multi-dimensional hyper-dimensional geometry with an invariant volume. An increase of spatial resolution is seen as a squeezing of the size of the volume in the spatial coordinate and extensions of lengths in other dimensions. Each optical element in the system, such as lenses, apertures, and gratings, leads to a geometric transformation operation on the multi-dimensional geometry. Therefore, by knowing the optical elements in the system, the output multi-dimensional geometry can be calculated. Conversely, by knowing the target output multi-dimensional geometry, including resolution, the optical elements needed can be identified.

1.3 Superoscillation Theories

As mentioned in the sections of each technique, inherent limitations and disadvantages exist in the process of forming super-resolution images, for instance, the potential damage to tissues due to high intensity laser beam of STED and the difficulty in building accurate experimental setup of TIRM, so researchers have continued to invent new techniques.

Superoscillation is a physical phenomenon in which the local oscillations of a band-limited signal (a signal that has negligible energy outside a finite frequency range) that fluctuate faster than the fastest Fourier component of the signal. A band-limited signal usually has a maximum rate of oscillation at its maximum or (negative) minimum frequency. A method of super-resolution imaging, utilizing superoscillatory waves, was originated in research conducted in the field of electromagnetic radiation by antennas by Schelkunoff. The research work on antennas was a precursor to the modern studies of superoscillation and related theories and also paved an alternative way to improve the resolution of imaging systems based on the mathematical methods for antennas.

1.3.1 Electromagnetism of antennas and super-resolution imaging

In 1943, Schelkunoff provided the mathematical theory of linear arrays of antennas and investigated the mathematical formulas of a narrower far field central peak. The instantaneous field is represented with complex numbers as

$$U(\theta) = \Sigma_{n=0}^{N-1} a_n e^{in(kl\cos\theta - \Delta\phi)} = \Sigma_{n=0}^{N-1} a_n z^n = (z - z_1)...(z - z_{N-1}), \qquad (1.3)$$

where θ is the direction of the emitted signal, l is the distance between antennas, the term $kl\cos\theta$ is the phase delay between each element, $\Delta\phi$ is the oscillating phase of signal emitted by each antenna. The equation is further expressed in the factored form in which the roots represent the zero intensity of the field, where $z = x + iy$ is the complex number representing the field of antennas.

Fig. 1.6 illustrates the relation between (a) geometric pattern of an antenna array and (b) the field of the antenna array on a complex plane. Since z is complex, it is located in the range of an arc on the unit circle with the length determined by the configurations of the antenna array. The root, z_n, also lies on the unit circle in the complex plane. The super-gain antennas theory, which is about a phenomenon of obtaining high directionality from small antennas, suggests that by squeezing the roots into a shorter arc of the unit circle, the antenna field can have a narrower peak.

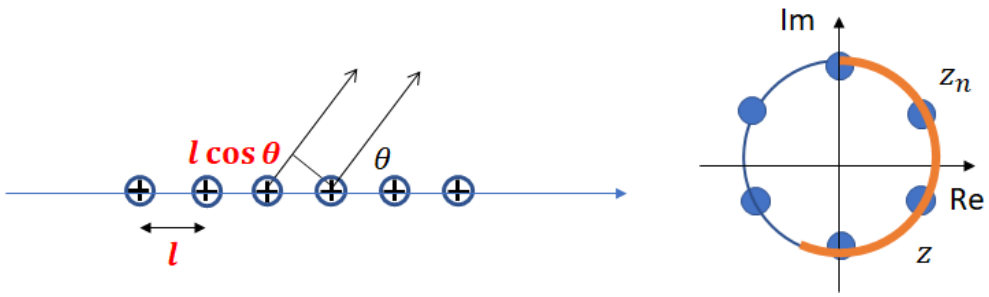

(a) (b)

Figure 1.6: Relation between (a) geometric pattern of an antenna array and (b) the field of the antenna array on a complex plane. The root, z_n, also lie on the unit circle in the complex plane. The field, z, is located in the range of the orange arc on the unit circle with the length determined by the configurations of the antenna array. The super-gain antennas theory suggests that by squeezing the roots into a shorter arc of the unit circle, the antennas field can have a narrower peak.

The intensity or directionality of the field is expressed by the norm of a polynomial with complex variables. Zeros of polynomials also specify the location of zero intensity. A radiation peak narrower than that of uniformly distributed antenna arrays is demonstrated by manipulating the zeros of polynomials [30].

Woodward and Lawson further pointed out that the change of directionality might be at the cost of having a large amount of evanescent wave power. In other words, the directionality is enhanced by moving the zero points from the evanescent wave region to the propagating wave region [31].

Toraldo applied the mathematical formula of antenna radiated power for imaging systems because of the similar radiation patterns of A.C. antennas and an electric dipole. According to Toraldo, each zero of the polynomials corresponds to a cone or a ring of zero intensity in the radiation patterns at the image plane. In addition, Toraldo created a super-resolved field at the image plane by overlapping multiple Bessel functions (PSFs of ring-shaped apertures), whose amplitudes are calculated using the specified zero positions [32].

1.3.2 The first superoscillation

In 1990, Aharonov *et al.* conducted a study titled "Superpositions of Time Evolutions of a Quantum System and a Quantum Time-Translation Machine"[33]. Following a suggestion of this study, in 1994, Berry introduced the concept of a superoscillation: a portion of a band-limited signal can oscillate faster than the fastest Fourier component of the signal [34, 35]. In another study, Berry pointed out that "it constitutes two-dimensional generalization of 'superoscillatory' functions of a single variable, which oscillate over arbitrarily long ranges arbitrarily faster than any of their Fourier components. I have recently investigated the properties of these curious functions (Berry 1994) following a suggestion of Aharonov et al (1990)." [36]. Furthermore, Berry provided the first mathematical construction of superoscillation given by [34]

$$g(x) = \frac{1}{a\sqrt{2\pi}} \int_{-\infty}^{\infty} e^{ik(u)x} e^{-\frac{1}{2a^2}(u-iu_c)^2} du, \tag{1.4}$$

where $k(u) = \frac{1}{1+u^2}$, u is real, and u_c is a constant. The term $e^{ik(u)x}$ behaves like a Fourier kernel and the maximum frequency, $k(u)_{\max} = 1$. When a approaches 0, $e^{-\frac{1}{2a^2}(u-iu_c)^2}$ approximates to a delta function, $\delta(u)$. As a result, $g(x) \approx \frac{1}{a\sqrt{2\pi}} e^{ik(iu_c)x}$. Then, $k(u) = \frac{1}{1-u_c^2} > 1$, when $u_c < 1$. Therefore, a local frequency $k(u) > 1$ that exceeds the bandlimit is achieved.

1.3.3 Simple mathematical methods of superoscillation

The Berry methods either involve complicated stationary phase methods or the canonical function, which is obviously just one function. To use superoscillations in applications, more methods of making superoscillations are needed. In 1996, a simplified form of superoscillation was addressed by Qiao, showing that moving local zeros closer together will not affect the overall bandwidth but will obtain a higher local frequency [37]. According to the Paley-Winer theorem, a bandlimited function in k space is entirely analytic in x space. For instance, the Fourier transform of a

rectangular function, $f(x)$, is a sinc function and is bandlimited. The sinc function can be expressed as the infinite factorial form and each of the polynomials in the function creates a zero point.

$$\mathrm{sinc}(\pi x) = \frac{1}{2\pi}\int_{-\pi}^{\pi} e^{-ikx}dk = \Pi_{n=1}^{\infty}(1-\frac{x^2}{n^2}). \tag{1.5}$$

Then, the Qiao method moves zeros of the first few polynomial terms closer to form a superoscillatory waveform:

$$g(x) = \Pi_{n=1}^{2}(1-\frac{a^2x^2}{n^2})\Pi_{m=3}^{\infty}(1-\frac{x^2}{m^2}). \tag{1.6}$$

Fig. 1.7 shows superoscillatory waveform, $g(x)$, after moving the first two zero points of $f(x)$ closer. It shows that, although superoscillatory waveforms are created, there are significant strong sidelobes next to it. Thus, it can be seen that superoscillations almost always come with sidelobes. Typically, sidelobes get relatively bigger the more superoscillatory the waveform becomes, which is a major problem.

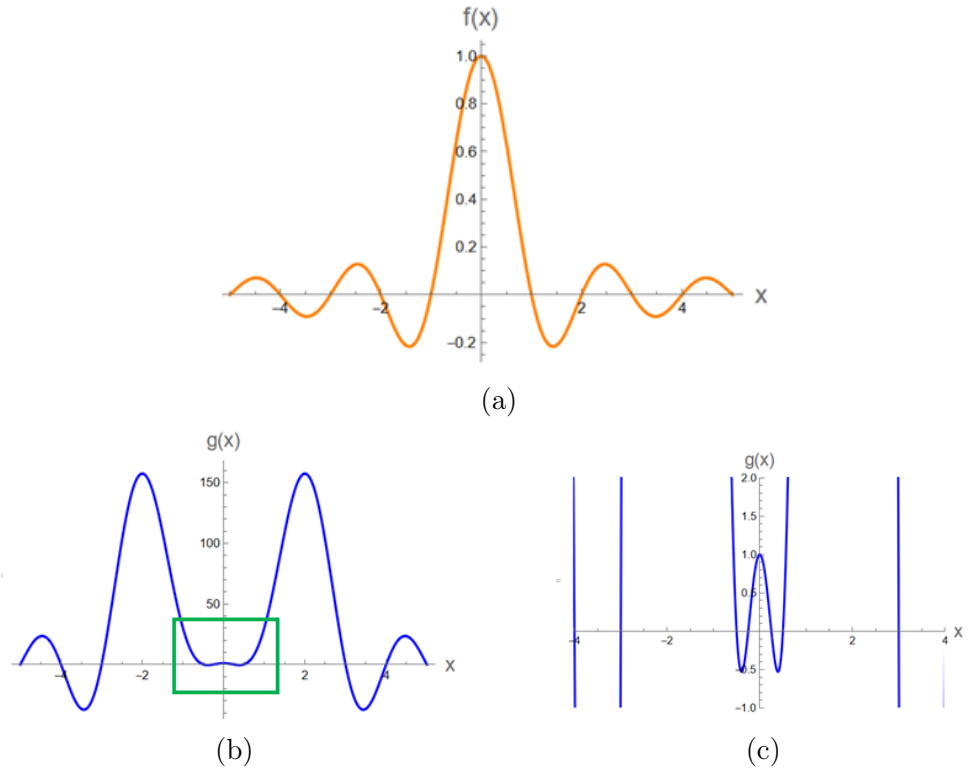

Figure 1.7: Superoscillatory waveform by moving first two zero rings closer. (a) $f(x)$ before moving first two zero rings closer, (b) $g(x)$, with superoscillatory waveform, by moving first two zero rings of $f(x)$ closer and (c) $g(x)$ under zoomed in condition.

Another simple mathematical representation is based on a straightforward application of polynomials and their zeros [38]. We consider a polynomial that is given by

$$P_N(t) = \sum_{n=0}^{N} a_n t^n. \tag{1.7}$$

We also introduce a band-limited envelope function, $e(t)$, with its Fourier transform of

$$E(\omega) = \int_{-\infty}^{\infty} e(t) e^{-i\omega t} dt, \tag{1.8}$$

where $|\omega| \leq a$ and $e(t)$ has at least N - 1 derivative and has a N^{th} derivative of bounded variant. A new function is given by the product of the envelope function and the polynomial function as

$$g\left(t\right)=e(t)P_N\left(t\right). \tag{1.9}$$

According to the derivative property of a Fourier transform,

$$F'(\omega)=\frac{1}{2\pi}\int f(t)\frac{d}{d\omega}e^{i\omega t}dt=\frac{1}{2\pi}\int itf(t)e^{i\omega t}dt, \tag{1.10}$$

the superoscillatory function $g\left(t\right)$ can be created by properly choosing a_n and its Fourier transform has the same bandlimit of $e(t)$. Fig. 1.8 shows a superoscillatory function created from the product of the envelope, $e(t)=\mathrm{sinc}(\frac{t}{4})^4$, and the polynomial,$P(t)=\frac{3\sqrt{3}}{2}(\frac{t^2}{0.1^3}-8)$[38], and the superoscillatory region after zooming in.

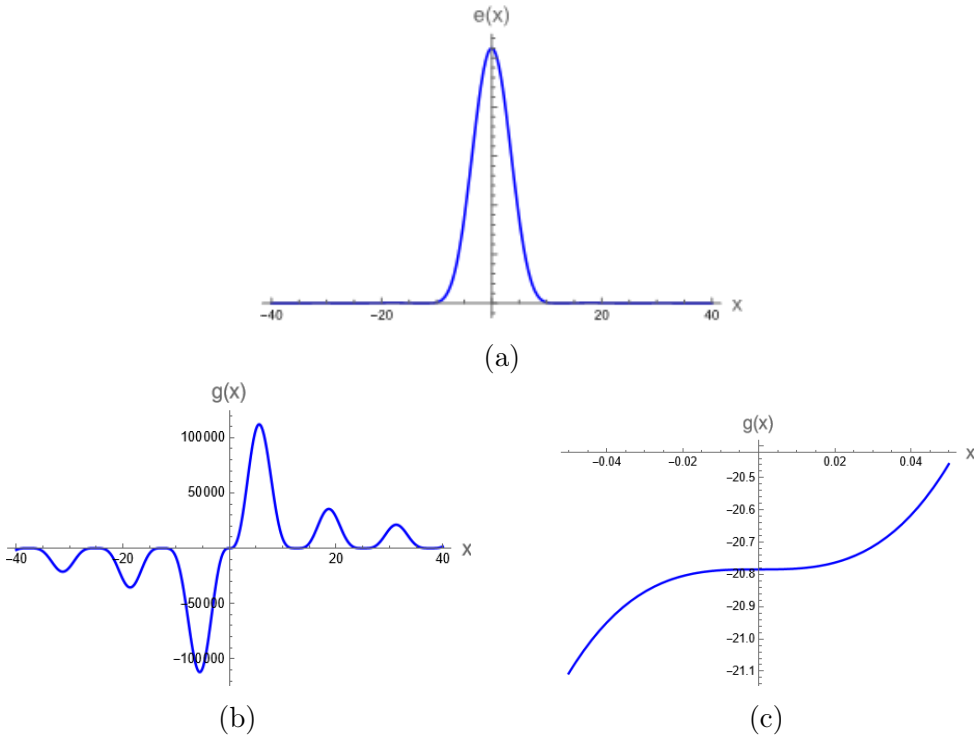

Figure 1.8: Superoscillations created by product of polynomials with their zeros and an envelope function: (a) an envelope function, $e(t)$, (b)superoscillatory waveform, and (c) the superoscillatory region after zooming in.

1.3.4 Prolate spheroidal wave functions and superoscillation

Another approach for mathematically constructing superoscillations is through the use of prolate spheroidal wavefunctions, which are inherently bandlimited [39]. These functions are orthonormal and form a complete set over $-\infty$ to ∞. Also, the functions are orthogonal and form a complete set over $-T/2$ to $T/2$:

$$\lambda_i \psi_i(t) = \int_{-T/2}^{T/2} \frac{\sin \Omega(t-s)}{\pi(t-s)} \psi_i(s) ds, \tag{1.11}$$

where T is a positive real number and λ_n is an eigenvalue of the function for a sinc operator. The solution of the prolate spheroidal wave equations is angular prolate spheroidal functions, as plotted in Fig. 1.9. As the number of oscillations in a finite interval increases with order, n, a linear combination allows you to make a super-oscillatory spot, like in Fig. 2.4d. Another paper for the signal processing application shows how the energy needed to fix superoscillatory fields that are formed by prolate spheroidal wave functions will increase as the band limit increases. In other words, for certain bandlimited signals to have a narrower superoscillatory wave, it is inevitable to increase the total signal level by using stronger normal waveforms [40].

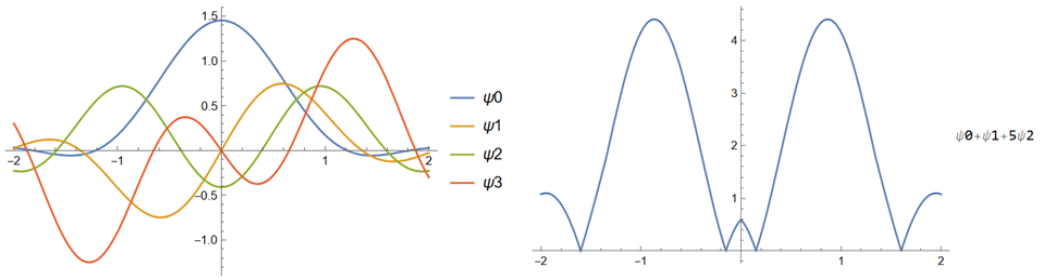

(a) (b)

Figure 1.9: Prolate spheroidal functions forming superoscillatory waveforms: (a) angular spheroidal wave functions, (b) superoscillatory waveform by linear combination of angular spheroidal wavefunctions.

Although some of the papers were written many decades ago and theories are deep, a recent review paper analyzes all the theories in the literature thoroughly, which is

very helpful to read [41].

1.4 Superoscillation for Imaging Application

1.4.1 Optical superoscillation

In 2006, Berry and Popescu introduced superoscillation in optics and investigated how it evolves in space and time [42]. The superoscillation is given by the function

$$f(x) = (\cos x + i\ a \sin x)^N, \tag{1.12}$$

where $a > 1$ and $N \gg 1$ and $f(x)$ is superoscillatory near $x = 0$. This function is often referred to as the "canonical function" for superoscillation. The Fourier series of the function is expressed by

$$f(x) \approx \sum_{m=0}^{N} c_m e^{iNk_m x}, \tag{1.13}$$

where $k_m = 1 - \frac{2m}{N}$ and

$$c_m = \frac{N!}{2^N} (-1)^m \frac{(a^2-1)^{N/2} [(a-1)(a+1)]^{Nk_m/2}}{\left[\frac{N(1+k_m)}{2}\right]! \left[\frac{N(1-k_m)}{2}\right]!}. \tag{1.14}$$

Thus, the maximum wave number of the function is N. However, the near zero approximation of $f(x)$ is given by

$$f(x) = e^{iaNx}, \tag{1.15}$$

which shows that the local wavenumber of $f(x)$ near $x = 0$ is determined by a, and thus demonstrates a superoscillation phenomenon. Fig. 1.10 shows the real parts of the example function under different zoomed in conditions with $a = 5$ and $a = 20$, respectively. As a increases, the degree of superoscillation will increase. The superoscillatory waveforms are demonstrated in Fig.1.10b and Fig.1.10d under zoomed in

conditions. It can be seen that the amplitude is very small at the superoscillatory wave region and is surrounded by huge sidelobes. These sidelobes is a problem for utilizing superoscillatory waves.

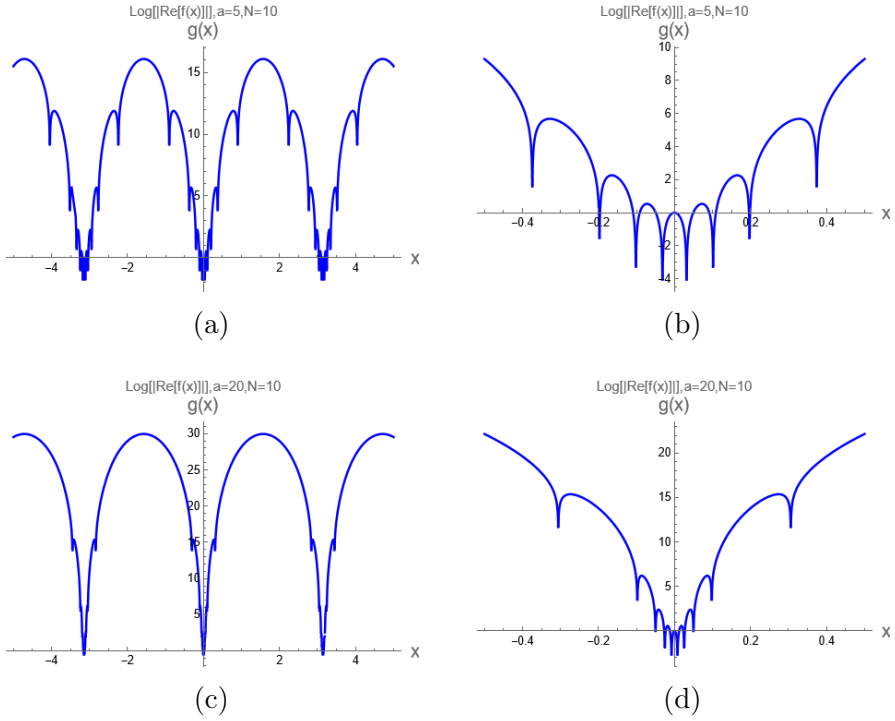

Figure 1.10: Real and imaginary parts of $f(x)$ of (a) $a = 5$, (b) $a = 5$ under zoomed in condition, (c) $a = 20$, and (d) $a = 20$ under zoomed in condition, with N = 10.

1.4.2 Superoscillation-based super-resolution imaging

Based on Berry and Popescu's study, optical superoscillations have several basic properties: they are rapid, sub-wavelength spatial variations of light's amplitude, phase, and intensity, which occur in electromagnetic fields and are formed by interference of several coherent waves; optical superoscillations can be arbitrarily fast and come with large sidelobes [42].

Since optical waves can be arbitrarily narrow based on optical superoscillation theories, optical superoscillations stimulated ideas of a new super-resolution technique, named superoscillatory imaging. There are multiple concepts on superoscillation-based super-resolution imaging. Zheludev reported superoscillation-based imaging by

conceptualizing superoscillatory fields as topologically structured light, as topologically structured light is considered more effective in scattering nanostructures (react to nanostructures stronger than plane waves). This technique has been developed into deeply sub-wavelength topological microscopy, which can localize positions of subwavelength object features through the light matter interaction, and the research methods share similarities to those of the near fields of plasmonic nanostructures [43].

It should be noted that in most cases, the superoscillatory imaging technique points a superoscillatory focal spot directly on objects or tissues and detects the scattered or transmitted optical fields from sub-wavelength structures to form an image. This approach is similar to that of near field optics and optical microscopy, but different from that of traditional camera systems.

One of the important properties of superoscillatory imaging is that it is a coherent imaging process, since a superoscillatory field is created by coherent interference. Hence, the superoscillatory imaging technique needs to be distinguished from some of the optical microscopy techniques, such as the bright field microscopy, which applies incoherent illumination. Accordingly, we further investigate the interference effect caused by closely positioned Rayleigh particles under a vector-superoscillatory field illumination in Chapter 3.

Regarding the resolution of the superoscillatory imaging technique, the Rayleigh criterion no longer applies to this technique. Instead, the resolution is primarily specified by the size of a superoscillatory spot, which is used for resolution analysis in the following chapters. Theoretically, a superoscillatory imaging system's resolution is expected to be limited by the detector of the system.

1.5 Spatial Coherence and Image Resolution

Coherence theory was traditionally about studying the observable characteristics of "natural" light, which is very random. Many studies investigated optical coherence by treating optical field fluctuations as a stochastic process. Important quantities, such

as mutual coherence, degree of coherence, and the cross-spectral densities (CSD), were defined and applied in the fields of microscopy and interferometry [44, 45, 46, 47, 48]. Further formulations of the propagation of coherence properties through Huygens' principle, as well as the generalized wave equations, paved the ways for understanding their characteristics in space and time domains [49, 50, 51].

1.5.1 Coherence effect in imaging

More recent work has investigated how structuring the statistical properties of light can change its behavior in radical ways. A study by Visser and Gbur investigated the effect of the state of coherence on the three-dimensional spectral intensity distribution in the focal region [52]. In the study, a Gaussian-Schell model for partial coherence was applied, which characterizes the CSD function in the form of

$$W_0(\rho_1, \rho_2, \omega) = S_0(\omega) e^{-(\rho_2 - \rho_1)^2 / 2\sigma_g^2}, \tag{1.16}$$

where $S_0(\omega)$ is the spectral density and σ_g denotes the effective spectral coherence length of the field in the aperture. $\rho = (x, y)$ is a two-dimensional vector in the transverse plane of the partial coherent field. The study shows that the maximum spectral intensity at the geometrical focus decreases with decreasing spectral coherence length, and the size of the focal spot increases as the spectral coherence length decreases. Finally, with decreasing spectral coherence length, the spectral intensity distribution becomes smoother. A follow-up study, however, showed that an appropriate choice of spatial can produce a local minimum of intensity at focus. This is one of the first to note that coherence can have a huge effect on properties of light [53].

Among the coherent quantities, cross-spectral density significantly simplifies mathematical calculation and is related to other quantities in space-time domain via Fourier transform [54]. Cross-spectral density (CSD) is defined as the two-point correlation

function of an ensemble of space-frequency realizations for any pair of points in the field given by

$$W(\boldsymbol{r}_1, \boldsymbol{r}_2; \omega) = \langle U^*(\boldsymbol{r}_1; \omega) U(\boldsymbol{r}_2; \omega) \rangle, \tag{1.17}$$

where $U(\boldsymbol{r}_i; \omega)$, with $i = 1, 2$ represents a member of a statistical ensemble of monochromatic realizations of the field and the angular brackets denote an average over an ensemble of monochromatic fields [54].

1.5.2 Superoscillation in coherence condition

Superoscillations in coherence functions have just begun to be studied [55]. It has been demonstrated that superoscillations can propagate to far field under partial spatial coherence condition. Furthermore, superoscillation behaviors might be strengthened under a decreased spatial coherence condition through the use of the Talbot effect.

1.6 Chapter Overviews

The remainder of this thesis is structured as follow:

Chapter 2 : Simplified superoscillatory lenses

Superoscillations have become a new method for creating superresolution imaging systems. However, the design of superoscillatory wavefronts and their corresponding lenses can be a complicated process. In the first study, we extend a recently-developed method for designing complex superoscillatory filters to the creation of phase-only and amplitude-only filters and compare their performance. These three types of filters can generate nearly identical superoscillatory fields at the image plane.

Chapter 3 : Vector superoscillatory field illumination

Although spatial superoscillations show great potential for performing super-resolution imaging, the superoscillatory waveforms are inevitably surrounded by high intensity

sidelobes that severely limit the usable super-resolved area of an image. In the second study, we demonstrate how polarization engineering can be used in some circumstances to suppress superoscillation sidelobes, taking advantage of the transverse wave nature of light. We illustrate the principle by a model super-resolution imaging system that can image Rayleigh scatterers with separations smaller than the classic Rayleigh criterion.

Chapter 4 : Circularly coherent Gaussian and vortex beams

Circular coherence sources are perfectly coherent along any ring that is concentric to the beam center. As circularly coherent beams demonstrate a focal region as a result of the self-focusing property of circular coherence, it has the potential to provide a narrower focal spot than that of its coherent counterpart. In addition, circular coherence sources have the potential to preserve the spiral phase structures of optical vortices on propagation. In the third study, we create circularly coherent Gaussian beam and vortex beams by imposing circular coherence on Laguerre-Gaussian (LG) beams. Subsequently, the second order coherence properties and coherence singularities of the circularly coherent Gaussian beam and vortex beams are investigated in free-space propagation. The results show that the spiral phase structures of optical vortices remain intact and stable in the transverse plane in free-space propagation.

Chapter 5 : Conclusion and future work

The main results of the thesis and potential future work are provided.

CHAPTER 2: SIMPLIFIED SUPEROSCILLATORY LENSES

2.1 Introduction

Developing practical superoscillatory field generation methods is important for superoscillatory imaging; the calculated amplitude and phase are required to encode optical field modulation devices, such as liquid crystal and spatial light modulators.

In 2016, Smith and Gbur extended the method by Chremmos and Fikioris, allowing the creation of tailored superoscillatory fields consisting of closely-spaced optical vortices in an image plane [56]. In 2020, this method was modified to design a superoscillatory filter for imaging [57], in which zero rings were used to generate a superoscillatory spot and to adjust the position of the sidelobes. Based on this method, the Smith and Gbur filter was designed as a continuous complex transmission filter, referred to as complex filters.

According to the Smith and Gbur method, for the first step, the optical field formed by an objective lens in the image plane is the Fourier transform of the objective lens transmittance multiplying two quadratic phase terms related to the object plane and the image plane coordinates and a phase term related to image distance, then scaled by the source amplitude, the wavelength, and the image distance:

$$U_{\mathrm{I}}(\mathbf{r}_{\mathrm{I}}) = \frac{iU_o e^{ikd_{\mathrm{I}}}}{\lambda d_{\mathrm{I}}} e^{\frac{ik}{2}\left(\frac{|\mathbf{r}_o|^2}{d_o}+\frac{|\mathbf{r}_{\mathrm{I}}|^2}{d_{\mathrm{I}}}\right)} \iint_A t(\mathbf{r}_{\mathrm{L}}) e^{-ik\left(\frac{\mathbf{r}_o}{d_o}+\frac{\mathbf{r}_{\mathrm{I}}}{d_{\mathrm{I}}}\right)\cdot\mathbf{r}_{\mathrm{L}}} d^2\mathbf{r}_{\mathrm{L}}, \tag{2.1}$$

where U_o is the object-field amplitude, λ is the wavelength of the optical field, and k is the wave number. $\mathbf{r}_o$, $\mathbf{r}_{\mathrm{I}}$, and $\mathbf{r}_{\mathrm{L}}$ are the position vectors of the object, the image, and the lens plane.

For the second step, a polynomial function is proposed in the form of

$$h(\mathbf{r}_\mathrm{I}) = \prod_{n=1}^{N} (|\mathbf{r}_\mathrm{I}|^2 - r_n^2), \tag{2.2}$$

where r_n is the radius of the n^{th} zero ring, and N is the total number of rings. Here, $h(\mathbf{r}_\mathrm{I})$ are zero rings in a two-dimensional space instead of zero points in a one-dimensional space. If the diameter of the smallest zero ring is less than a wavelength, the product of $h(\mathbf{r}_\mathrm{I})$ and the Fourier transform of the lens transmittance, $\tilde{t}(\mathbf{r}_\mathrm{I})$, forms a superoscillatory field. It is worth noting that if $h(\mathbf{r}_\mathrm{I})$ consists of a single zero ring, the superoscillatory field will have a small central lobe and a large ring sidelobe. Nevertheless, the large sidelobes can be pushed further away from the central lobe by adding additional rings beyond the innermost zero ring.

For the third step, the inverse Fourier transform of the superoscillatory field gives the transmittance needed by the lens to obtain the superoscillatory field, expressed as

$$t'(\mathbf{r}_\mathrm{L}) = \mathcal{F}^{-1}[\tilde{t}(\mathbf{r}_\mathrm{I}) h(\mathbf{r}_\mathrm{I})]. \tag{2.3}$$

This method will generally produce a transmittance function $t'(\mathbf{r}_\mathrm{L})$ that has a nontrivial phase and amplitude variance: a complex spatial filter. Such a filter is usually difficult to achieve in practice and significantly reduces the transmitted field intensity, a problem for superoscillations that inherently possess a low intensity image spot.

This chapter modifies the complex filter to generate individual amplitude (section 2.3) profile and phase (section 2.4) profile from a complex one, and investigate the effect of these modifications on the superoscillations and the light throughput. These changes indicate how the superoscillatory filter of Smith and Gbur can be modified for practical use.

Other techniques for the realization of superoscillation can be found in a number

of review articles [58, 41, 59].

2.2 Complex Filter

A complex superoscillatory filter is first created by using the method above. Then this complex filter is modified to be phase-only or amplitude-only, and determine whether the superoscillations are affected by the modification. The applied lens system is accessible to laboratory environment. The lens has a diameter of 62.5 mm and a focal length of 50 mm (F/#=1.25). The object distance is 150 mm, and the image distance is 75mm. The wavelength of light is 500 nm. Here, the designed filters are in two dimensions, though the complex filter is azimuthally symmetric, and the transforms related to it were calculated as Fourier-Bessel transforms.

The design process of the complex filter is a straightforward implementation of the Smith and Gbur method. The system setup is shown in Fig. 2.1.

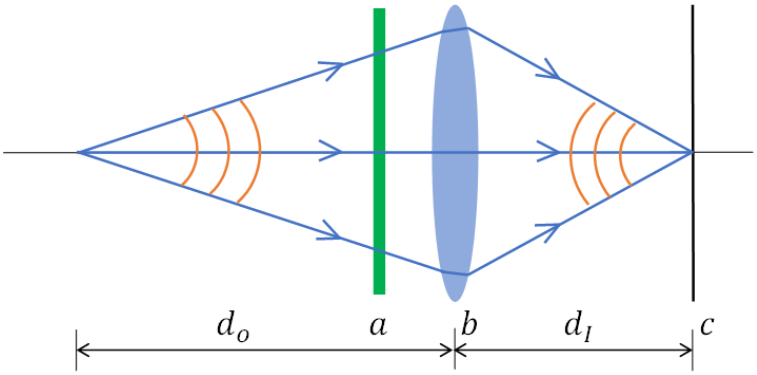

Figure 2.1: Experimental setup for obtaining the transmittance of a superoscillatory filter: (a) a superoscillatory filter, (b) a lens, and (c) a detector. The orange lines show the wavefront of the optical field

2.2.1 Amplitude and phase profile

The expression for the transmittance of a complex filter is in the form,

$$C(\mathbf{r}_\mathrm{L}) = W(\mathbf{r}_\mathrm{L})e^{i\phi(\mathbf{r}_\mathrm{L})}, \tag{2.4}$$

where $W(\mathbf{r}_\mathrm{L})$ is the amplitude transmittance, $\phi(\mathbf{r}_\mathrm{L})$ is the phase transmittance, and $\mathbf{r}_\mathrm{L}$ is the coordinate vector in the filter plane.

According to the method proposed by Smith and Gbur, an example of a complex filter is obtained as follows. For the first step, a windowed filter plane transmittance is introduced as

$$t(\mathbf{r}_\mathrm{L}) = \cos^8(\frac{\mathbf{r}_\mathrm{L}}{L}) \sqcap (\frac{\mathbf{r}_\mathrm{L}}{L}), \tag{2.5}$$

where $\cos^8(\frac{\mathbf{r}_\mathrm{L}}{L})$ is the lens transmittance. According to section 2.1, it is necessary to have enough zero rings to create sufficient separation between the central and sidelobes. As a result, we include 4 zero rings and choose $\cos^8(\frac{\mathbf{r}_\mathrm{L}}{L})$ as the lens transmittance because we need a field that is 8-fold differentiable in order to include 4 zero rings. $\sqcap(\frac{\mathbf{r}_\mathrm{L}}{L})$ is a two-dimensional function that defines a circular aperture, and L is the diameter of the lens. For the second step, the Fourier Bessel transform of this lens transmittance at the image plane, $\mathcal{F}[t(\mathbf{r}_\mathrm{L})]$ is calculated as,

$$\mathcal{F}[t(\mathbf{r}_\mathrm{L})] = \int_0^{L/2} \cos^8(\frac{\mathbf{r}_\mathrm{L}}{L}) \sqcap (\frac{\mathbf{r}_\mathrm{L}}{L}) J_0(r\frac{k\mathbf{r}_\mathrm{I}}{d_i})\mathbf{r}_\mathrm{L} d\mathbf{r}_\mathrm{L}. \tag{2.6}$$

For third step, four zero rings are introduced to this plane to give a superoscillatory field,

$$S(\mathbf{r}_\mathrm{I}) = \mathcal{F}[t(\mathbf{r}_\mathrm{L})](\mathbf{r}_\mathrm{I}^2 - \Delta_1^2)(\mathbf{r}_\mathrm{I}^2 - \Delta_2^2)(\mathbf{r}_\mathrm{I}^2 - \Delta_3^2)(\mathbf{r}_\mathrm{I}^2 - \Delta_4^2), \tag{2.7}$$

where the Δ_i, the radius of a zero ring, have been taken as Δ_1 =0.47 μm (0.94λ), Δ_2=1.0μm, Δ_3 =1.48μm, and Δ_4 = 2.0μm. The first zero ring at radius Δ_1 defines the radius of the superoscillatory spot; the second to the fourth rings push the sidelobes further from this spot. For the objective lens alone without the superoscillatory filter, the radius of the Airy disc, and thus the Rayleigh resolution limit, is 0.73μm (1.46 λ), which is about twice of that of the superoscillatory spot. Figure 2.2 shows the intensity distribution of the superoscillatory field in the image plane with a small superoscillatory wave located in the center surrounded by a large ring sidelobe with

four zero rings in between. As expected, the large sidelobe is roughly three times the size of the subwavelength central spot.

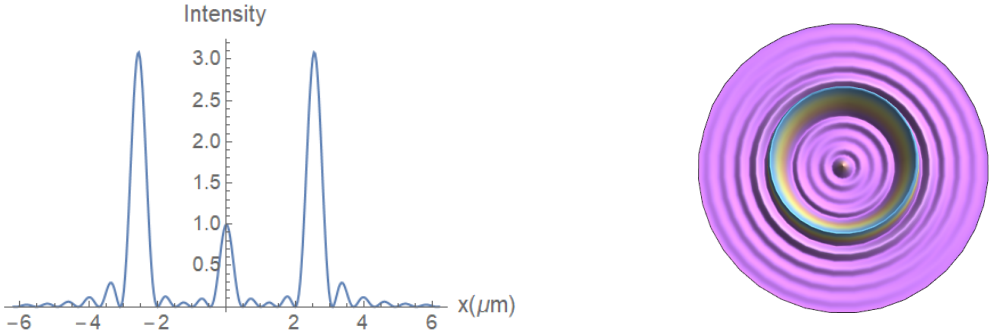

(a) (b)

Figure 2.2: A superoscillatory field (radius, r_{spot}=0.94λ) located in the center of large sidelobes: (a) a cross-sectional view and (b) a top view.

For the fourth step, the complex transmittance of the filter is given by the inverse Fourier Bessel transform of $S(\mathbf{r}_{\text{I}})$. Since the superoscillatory field is a non-trivial function, the inverse Fourier Bessel transform is achieved numerically, instead of analytically as

$$t'(\mathbf{r}_{\text{L,m}}) = \Sigma_{n=0}^{N} S(\mathbf{r}_{\text{I,n}}) J_0(r_{\text{I,n}} \frac{k r_{\text{L,m}}}{d_i}) r_{\text{I,n}} \Delta r_{\text{I}}. \tag{2.8}$$

Figure 2.3 shows both the cross-sectional and three-dimensional amplitude transmittance and the phase of the complex filter calculated for the two-dimensional superoscillatory field, with the total number of pixels $M = 151$ and pixel size $\Delta x = 0.4\,\text{mm}$. It can be seen that it has a nontrivial structure, with significant amplitude and phase changes. The phase distribution is a circularly symmetric function, and its value is either 0 or π. A relative phase delay of π causes an optical path difference (OPD) of $\lambda/2$. The shape of the amplitude profile and phase profile of the complex filter show that they function as a Fresnel zone plate and a Fresnel phase plate, respectively. Both types of Fresnel plates provide a single diffraction order at the image center. The interference of the two fields formed by the two plates leads to a superoscillatory spot.

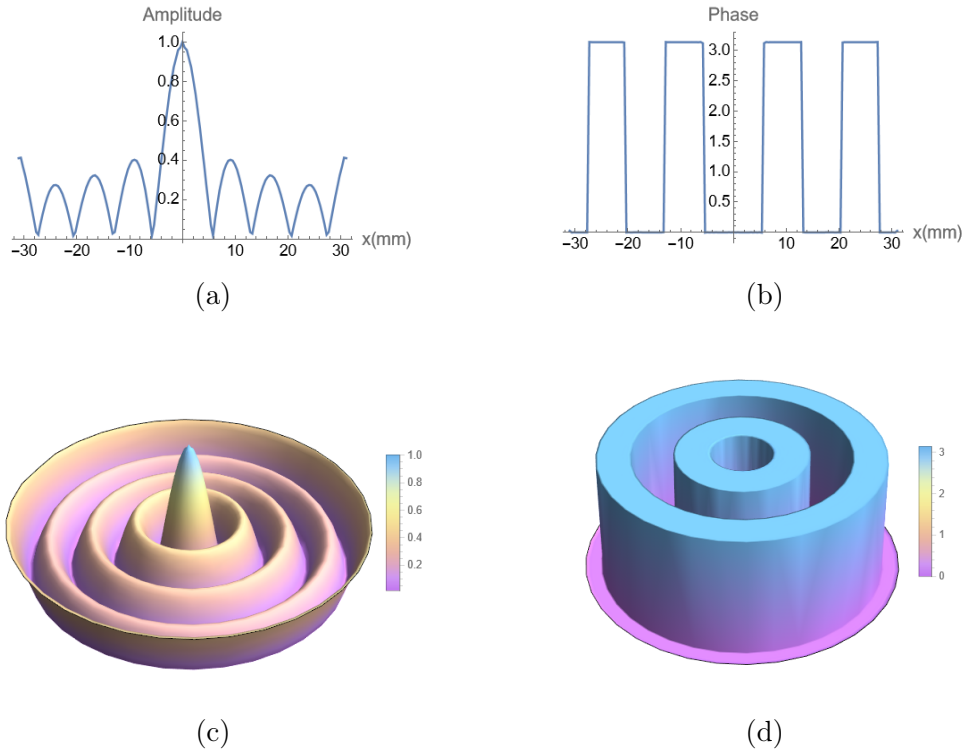

Figure 2.3: Designed transmittance of a complex filter: (a) cross-sectional amplitude, (b) cross-sectional phase, (c) three-dimensional amplitude, and (d) three-dimensional phase, with $M = 151$, $\Delta x = 0.4\,\mathrm{mm}$.

2.2.2 Superoscillatory image field

The superoscillatory image field is calculated by a numerical Fourier Bessel transform as

$$U_{\mathrm{img},n} = \Sigma_{m=0}^{M} t'(\mathbf{r}_{\mathrm{L},m}) J_0(r_{\mathrm{I},n} \frac{k r_{\mathrm{L,m}}}{d_i}) r_{\mathrm{L,m}} \Delta r_{\mathrm{L}}. \tag{2.9}$$

Figure 2.4 shows the image spots created by a regular lens, the designed complex filter, the amplitude profile of the complex filter, and the phase profile of the complex filter. The images in the figure demonstrate a tradeoff between the central peak width and the relative energy contained in the central spot. Although the combination of the amplitude profile and the phase profile produces a superoscillatory field, it is difficult to fabricate such a filter. Therefore, we look into the device with only an amplitude profile that can produce the identical superoscillatory spot.

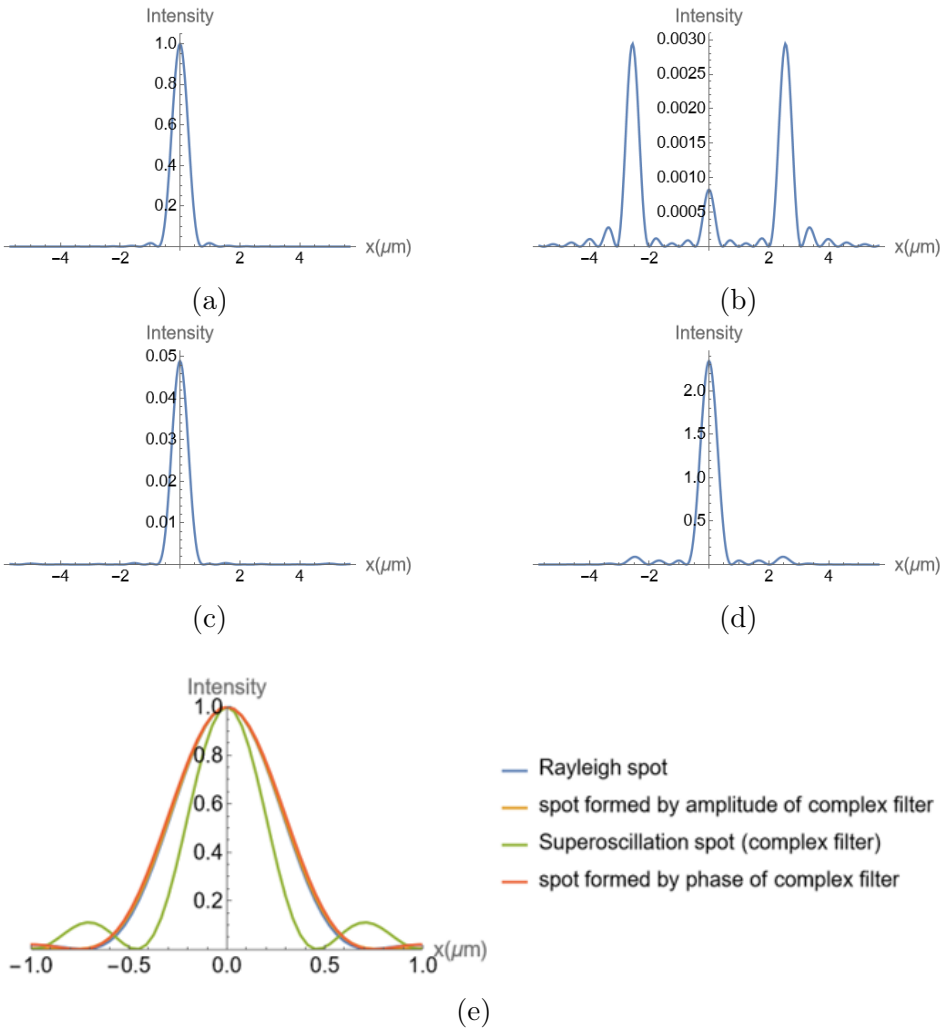

Figure 2.4: Image spots formed by (a) a regular lens (r_{spot}=1.46λ), (b) a complex filter with the same aperture size of the regular lens (r_{spot}=0.94λ), (c) the amplitude profile of the complex filter (r_{spot}≈1.46λ), (d) the phase profile of the complex filter (r_{spot}≈1.46λ); and comparison of spots with intensity normalized at the central peak (e), with $M = 151$, $\Delta x = 0.4\,\text{mm}$.

It is noted that the calculation of the filter transmittance and the image field is achieved by a one-dimensional numerical Fourier Bessel transform. The reasons of using this method are: (1) transmittance is rotationally symmetric, thus the results by using one-dimensional numerical Fourier Bessel transform is identical to that by using two-dimensional Fourier transform, (2) the superoscillatory field function is non-trivial, for which is difficult to perform an analytical Fourier Bessel transform, and

(3) numerical Fourier Bessel transform provides the flexibility to set the number of points in the object and the image field, respectively, which can avoid the limitations on the range and the resolution of images by using fast Fourier transform (FFT).

2.2.3 Estimation of the minimum number of pixels

As the pixel size increases and the pixel number M correspondingly decreases, it is expected that the superoscillatory pattern will inevitably break down. One of the effects of this change is that as the pixel number M decreases, the transmittance curve of the filter will increasingly deviate from the shape of the ideal transmittance. As a result, the central peak of the superoscillatory field will get smaller and eventually cannot be resolved.

The complex filter profile with a limited number of pixels is obtained from the interpolation of an approximated filter profile function. The interpolated amplitude and phase is assumed to be constant across the window of the pixel, which leads to a step-wise profile. The superoscillatory image field is calculated by a numerical Fourier Bessel transform.

As a criterion for the minimum pixel number, the intensity ratio, r, of the sidelobe to the central lobe is used as the first criterion for the minimum pixel number. For example, if $r \leq 4$ is required, then the minimum pixel number is $M = 23$. Figure 2.5 shows the amplitude transmittance of complex filters with different pixel numbers and the corresponding superoscillatory fields.

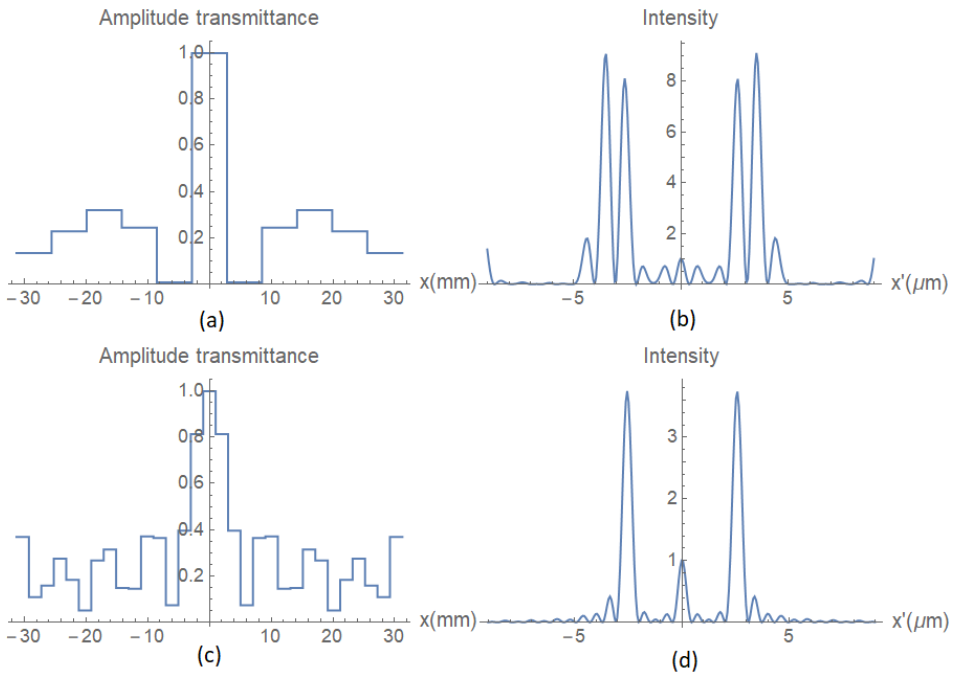

Figure 2.5: Complex filter transmittance with different pixel numbers and the corresponding superoscillatory fields: (a) amplitude transmittance with $M = 11$, $\Delta x = 5.7\,\text{mm}$, and the corresponding (b) superoscillatory field, and (c) amplitude transmittance with $M = 31$, $\Delta x = 2\,\text{mm}$, and the corresponding (d) superoscillatory field.

2.3 Amplitude-only Filtering Device

A method for designing an amplitude-only filter was detailed by Adzhalov et al. [60]. This method has also been applied in an earlier study on binary computer-generated holograms [61]. The complex exponential of Eq. (2.4) is replaced with a cosine function, resulting in two images of the field; a baseline transmittance, often called the DC term, is added to make the total transmittance real and positive. We now investigate how a change from a complex filter to an amplitude filter affects the superoscillation structure.

Figure 2.6 shows the proposed system for creating a superoscillatory field with an amplitude-only filter, which has a sinusoidal amplitude profile that leads to three diffraction orders, labeled the 0^{th} order and $\pm 1^{\text{st}}$ orders. The 0^{th} order is the transmitted light from the DC term.

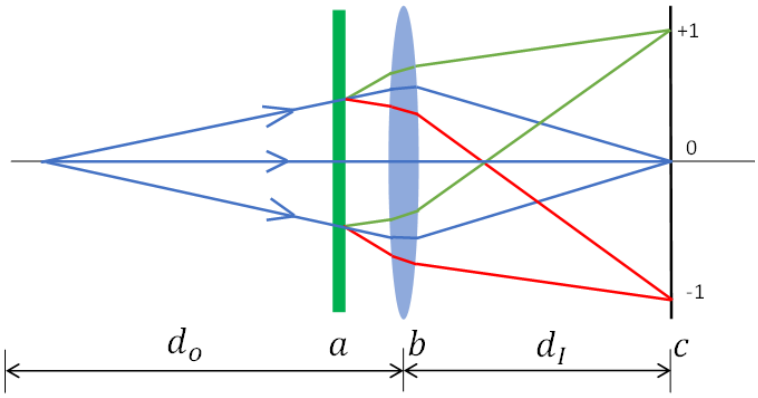

Figure 2.6: Proposed system for creating superoscillatory field with an amplitude-only filter: (a) an amplitude-only filter, (b) a lens, and (c) a detector.

2.3.1 Amplitude profile

The transmittance of the amplitude-only filter is given by

$$A(\mathbf{r}_\mathrm{L}) = A_0 + 2\Delta A(|W(\mathbf{r}_\mathrm{L})|/W_\mathrm{max})\cos\{2\pi ax + \phi(\mathbf{r}_\mathrm{L})\}, \tag{2.10}$$

where A_0 is the DC term, and $A_0 = \alpha_0 + \frac{\Delta\alpha}{2}$, with $0 < \alpha_0 \leq 1$ and $0 < \Delta\alpha \leq 1 - \alpha_0$. ΔA is a free parameter that controls the amplitude of the sinusoidal function. Here, we take $\Delta A = \beta\Delta\alpha/4$, with $0 < \beta \leq 1$. The quantity $|W(\mathbf{r}_\mathrm{L})|$ is the amplitude of the complex filter calculated in section 2.2.1, W_max is the maximum amplitude of the complex filter, and $\phi(\mathbf{r}_\mathrm{L})$ is the phase of the complex filter. The additional term $2\pi ax$ in the cosine function creates a transverse shift of the $\pm 1^{\mathrm{st}}$ orders from the 0^{th} order; therefore, a determines the separation of the three orders.

Taking into account the aperture size, the DC term is a two-dimensional circ function. Thus, under a Fourier relation, the 0^{th} order diffraction produces an Airy pattern expressed as the absolute square of a Jinc function whose cross-sectional distribution is given by

$$I(x') = I_0\left[\frac{2J_1(\frac{kLx'}{2R})}{\frac{kLx'}{2R}}\right]^2, \tag{2.11}$$

where x' is a point in the image plane, and R is the distance between the center of the aperture stop and x'. In the design, a must be chosen so that the $\pm 1^{\text{st}}$ orders lie outside the central lobe of this function. In addition, since the Airy pattern is not monotonic but oscillatory, the superoscillatory spot might interfere with the sidelobes of the Airy pattern. Therefore, the sidelobe of the Airy pattern that superimposes with the superoscillatory spot needs to be significantly smaller than that of the superoscillatory spot. Here, we estimate the minimum shift of a as the position where the Airy pattern has the maximum peak intensity I_{jp} less than 1/10 of that of the central lobe of the superoscillatory field, I_{c}. Then, a is calculated by finding the value of x' such that

$$I_{\text{jp}}(x') = I_0 \left| \frac{2J_1\left(\frac{k_0 L x'}{2\sqrt{x'^2+d_{\text{I}}^2}}\right)}{\frac{k_0 L x'}{2\sqrt{x'^2+d_{\text{I}}^2}}} \right|^2 \leq \frac{1}{10} I_{\text{c}}, \tag{2.12}$$

where I_{jp} is the sidelobe intensity of the Jinc function, L is the aperture diameter, I_0 is the intensity of the central peak of the Jinc function and I_{c} is the intensity of the central peak of the superoscillatory spot. To determine x', a series of sidelobe intensities are calculated by using the peak positions of the oscillating Jinc function, x'_{p}, which lie roughly between two adjacent zero points. Then, we find the largest $I_{\text{jp}}(x') \leq \frac{1}{10} I_c$. Finally, the shift parameter a in spatial frequency domain is converted from the estimated separation in space domain, x', based on the well-known relation $x = f_x \lambda z$, by

$$a = \frac{x'}{\lambda d_{\text{I}}}, \tag{2.13}$$

where d_{I} is the image distance, and x' is the desired shift of the $\pm 1^{\text{st}}$ orders in the image plane.

The amplitude filter and the resulting image were calculated by inputting the complex filter values into Eq. (2.10). Figure 2.7 shows the amplitude of the amplitude-only filter, with $\alpha_0 = 0$, $\Delta\alpha = 1$, $\beta = 1$, $a = 284\,\text{m}^{-1}$, $M = 151$, and $\Delta x = 0.4\,\text{mm}$. According to Eq. (2.13), $a = 284\ \text{m}^{-1}$ leads to a separation of $\Delta_{x'} = 10.6\,\mu\text{m}$ between

the $\pm 1^{st}$ orders and the 0^{th} order. The amplitude profile is essentially the that of the complex filter enveloped by a cosine function.

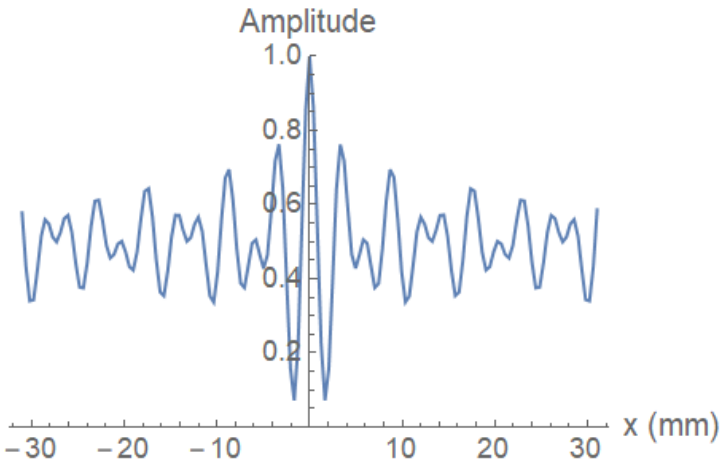

(a)

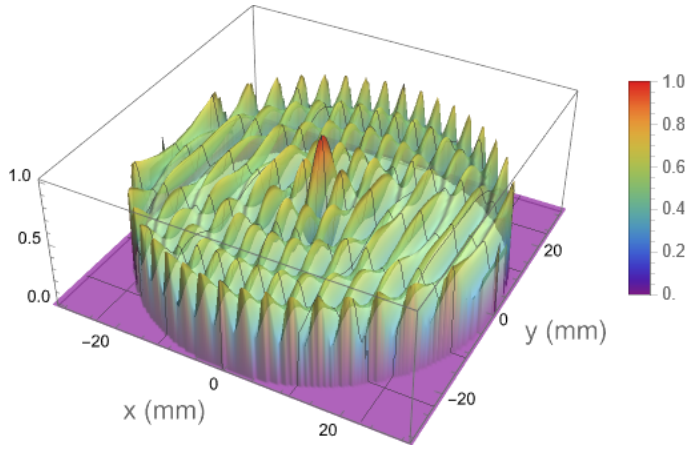

(b)

Figure 2.7: Designed amplitude of an amplitude-only filter, with $\alpha_0 = 0$, $\Delta\alpha = 1$, $\beta = 1$, $a = 284\ \mathrm{m}^{-1}$, $M = 151$, and $\Delta x = 0.4\,\mathrm{mm}$, (a) one-dimensional amplitude profile and (b) three-dimensional amplitude profile.

2.3.2 Superoscillatory image field

Since the transmittance of the amplitude-only filter is non-symmetric, the super-oscillatory field was calculated by use of FFT. In Mathematica, the transmittance arrays are shifted so that the central element is located as the first element. Then, the function Fourier is applied to conduct the FFT. Finally, the array is shifted back to its original order.

Figure 2.8 shows the intensity distribution of a superoscillatory field in the image plane formed by the amplitude-only filter using the above parameters. It can be seen from the cross-sectional plot (Fig. 2.8a) and the perspective view in full scale (Fig. 2.8b) that the majority of the energy of the incident field is concentrated in the 0^{th} order. In the cross-sectional profile with a truncated 0^{th} order (Fig. 2.8c), superoscillatory spots of the $\pm 1^{\text{st}}$ orders are visible, though the shapes are distorted by the underlying 0^{th} order spot. From the zoomed-in top view of the $+1^{\text{st}}$ order (Fig. 2.8e), other peaks exist in the xy plane near the desired superoscillatory spot due to interference.

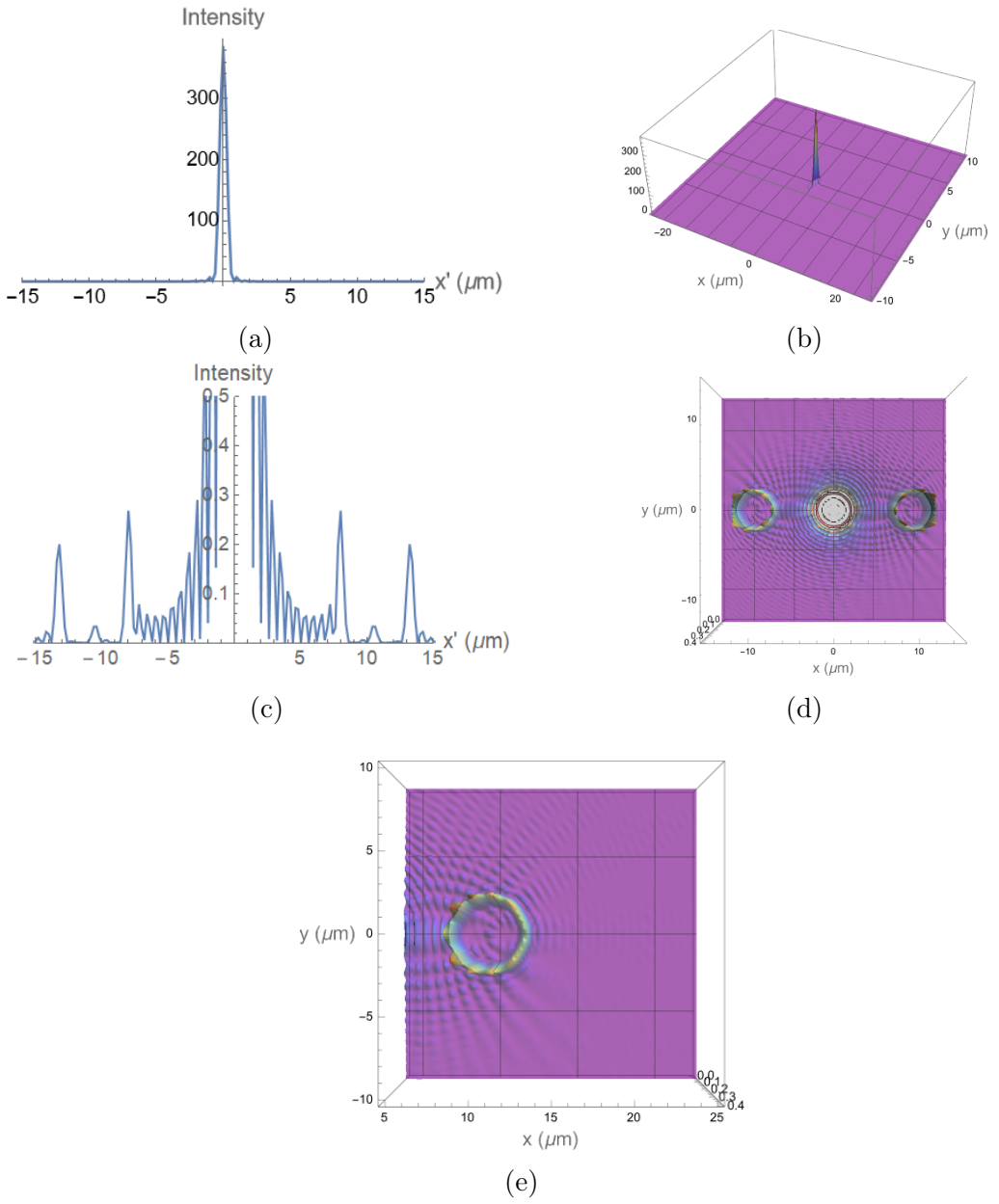

Figure 2.8: Intensity distribution of a superoscillatory field in the image plane formed by an amplitude-only filter with $\alpha_0 = 0$, $\Delta\alpha = 1$, $\beta = 1$, $a = 284\,\mathrm{m}^{-1}$, $M = 151$, and $\Delta x = 0.4\,\mathrm{mm}$: (a) cross-sectional profile in full scale, (b) perspective view in full scale, (c) cross-sectional profile of a truncated 0^{th} order and $\pm 1^{\mathrm{st}}$ orders, (d) top view of a truncated 0^{th} order and $\pm 1^{\mathrm{st}}$ orders, and (e) top view of 1^{st} order, with (r_{spot}=0.94λ).

A larger separation between the superoscillatory spot and the Airy pattern can help to reduce their interference effect. However, it will lead to a larger parameter a and a more oscillatory amplitude profile of the filter, which is harder to achieve in a

fabrication process.

In addition, it is clear from the figure that the vast majority of the intensity goes into the 0^{th} order spot; though the superoscillations are maintained, this loss of energy and large 0^{th} order background are significant disadvantages of this filter. With this in mind, we move on to the phase-only filter.

2.4 Phase-only Filtering Device

A method for designing the phase distribution of a phase-only filter was detailed by Kirk and Jones [62]. Figure 2.9 shows the proposed setup for creating a superoscillatory field with a phase-only filter. As described below, the conversion to be a phase-only filter results in an infinite number of transverse diffraction orders, only one of which will precisely reproduce the desired superoscillatory field.

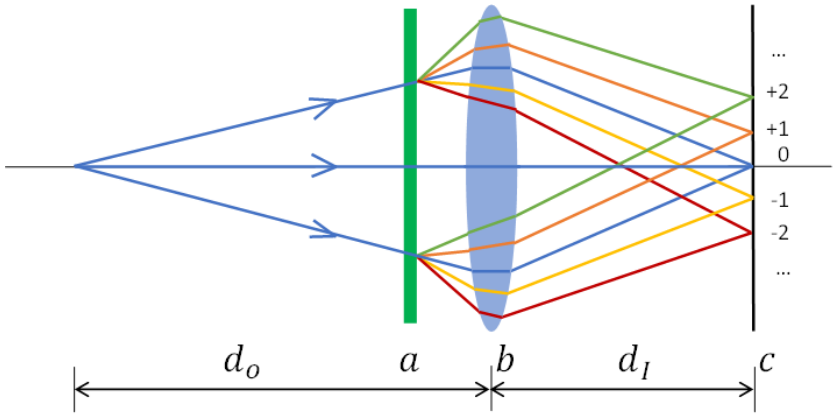

Figure 2.9: Proposed system for creating a superoscillatory field with a phase-only filter: (a) a phase-only filter, (b) a lens, and (c) a detector.

2.4.1 Phase profile

The transmittance of the phase-only filter is written as

$$T(\mathbf{r}_{\text{L}}) = e^{i[\phi(\mathbf{r}_{\text{L}}) + h(\mathbf{r}_{\text{L}})\cos(ax)]}, \tag{2.14}$$

where $\phi(\mathbf{r}_{\text{L}})$ is the phase of the designed complex filter and a is again a carrier frequency used to separate orders. Generally speaking, the higher the carrier frequency

is, the better an approximation of the ideal superoscillatory field will be. In a practical device, the filter will consist of finite-sized pixels, and the size and number of pixels will also affect the structure of the superoscillatory pattern. We write the carrier frequency in the form of $a = 2\pi b/\Delta x$, where Δx is the pixel size of the filter in the x direction, and b is the number of sinusoidal cycles in each pixel. The quantity $h(\mathbf{r}_\mathrm{L})$ is taken as the form $h(\mathbf{r}_\mathrm{L}) = J_{n'}^{-1}[W(\mathbf{r}_\mathrm{L})]$, where n' is the order of the inverse of a Bessel function, and $W(\mathbf{r}_\mathrm{L})$ is the amplitude transmittance of the complex filter.

The transmittance can be rewritten using the Jacobi-Anger expansion in the form,

$$\begin{aligned} T(\mathbf{r}_\mathrm{L}) &= e^{i\phi(\mathbf{r}_\mathrm{L})} \sum_{n=-\infty}^{\infty} i^n J_n[h(\mathbf{r}_\mathrm{L})] e^{inax} \\ &= e^{i\phi(\mathbf{r}_\mathrm{L})} \sum_{n=-\infty}^{\infty} i^n J_n[J_{n'}^{-1}[W(\mathbf{r}_\mathrm{L})]] e^{inax}. \end{aligned} \tag{2.15}$$

This expression indicates that the phase-only transmission function results in a large number of diffraction orders with carrier frequencies na. It can be seen that only the order $n = n'$ will reproduce the transmittance of the designed complex filter, with carrier frequency $n'a$. In other words, only one of the diffraction orders will reproduce the designed superoscillatory field. For example, if $h(\mathbf{r}_\mathrm{L})$ is the inverse of the 1^{st} order Bessel function, then the 1^{st} order term in Eq. (2.15) will reproduce the designed superoscillatory field.

Unlike the amplitude-only case, the 0^{th} order of a phase-only filter may also be used for imaging. In the calculations that follow, we set $h(\mathbf{r}_L) = J_0^{-1}[W(\mathbf{r}_\mathrm{L})]$ and thus let the filter's 0^{th} order carry the superoscillatory field.

Since the Bessel function is non-injective, it is impossible to obtain its inverse directly. Instead, we approximate the Bessel function by the first fifty terms of its power series expansion and calculate the inverse of each term respectively. Here, for

simplicity's sake, $h(\mathbf{r}_{\mathrm{L}})$ with its first three terms is expressed by

$$h(\mathbf{r}_{\mathrm{L}}) = -2\sqrt{1 - W(\mathbf{r}_{\mathrm{L}})} + \frac{1}{4}(1 - W(\mathbf{r}_{\mathrm{L}}))^{3/2} - \frac{47}{576}(1 - W(\mathbf{r}_{\mathrm{L}}))^{5/2}, \tag{2.16}$$

where $W(\mathbf{r}_{\mathrm{L}})$ is the amplitude of the complex filter and $W(\mathbf{r}_{\mathrm{L}}) < 1$.

Figure 2.10 shows the phase distribution of a phase-only filter, with pixel size $\Delta x = 2\,\mathrm{mm}$, $M = 31$, $b = 1$, and $a = 3116.5\ \mathrm{mm}^{-1}$. The phase distribution is calculated from Eq. (2.14). The zoomed in figures show the sinusoidal profile within each pixel.

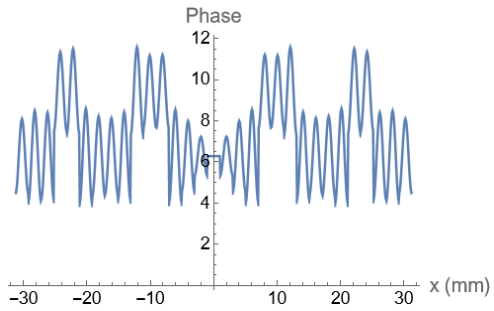

(a)

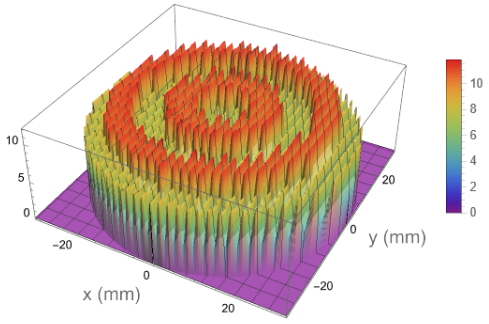

(b)

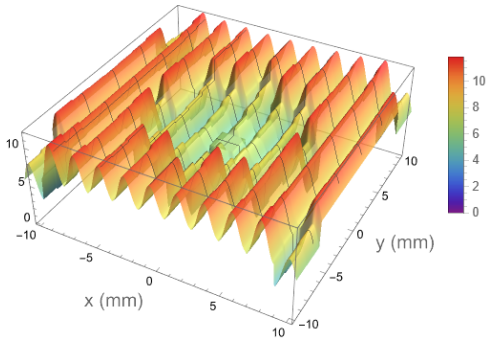

(c)

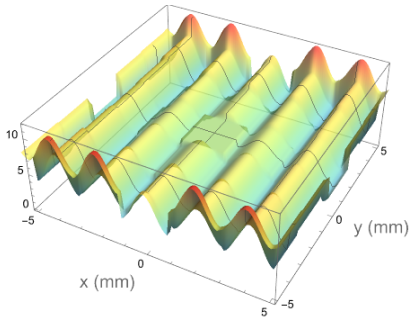

(d)

Figure 2.10: Phase of the designed phase-only filter, with $\Delta x = 2$ mm, $M = 31$, $b = 1$, and $a = 3116.5$ mm^{-1}, (a) one-dimensional phase profile, (b) three-dimensional phase profile, (c) three-dimensional phase profile within (-10,10) mm, and (d) three-dimensional phase profile within (-5,5) mm.

2.4.2 Superoscillatory image field

The intensity distribution of a point source at the image plane can be calculated through a window Fourier transform. Fig.2.11 shows the geometry and parameters related with the calculation.

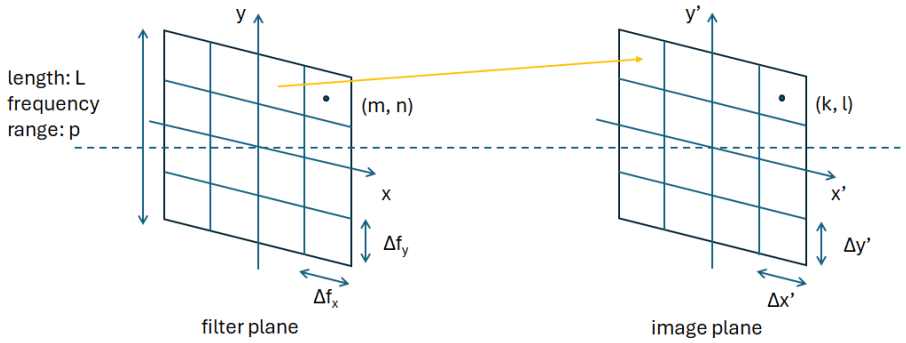

Figure 2.11: Setup and parameters for the window Fourier transform.

The window Fourier transform is expressed as

$$\begin{aligned} I_{k,l} =& |A_{k,l}|^2 \\ =& |L^2 \Delta x' \Delta y' \int_0^p \int_0^p T(f_x, f_y) e^{-2\pi i (k f_x \Delta x' + l f_y \Delta y')} \mathrm{d}f_x \mathrm{d}f_y|^2, \end{aligned} \tag{2.17}$$

where $A_{k,l}$ is the field at a sampled point (k, l) in the image plane, L and p are the lengths of the filter in the space domain and the spatial frequency domain, respectively, f_x and f_y are coordinates of the filter in spatial frequency domain, and $\Delta x'$ and $\Delta y'$ are the sampling steps in the x' and y' directions at the image plane. By substituting the phase of Eq. (2.14) into Eq. (2.19) and then discretizing the filter transmittance, the field is expressed as

$$\begin{aligned} A_{k,l} =& L^2 \Delta x' \Delta y' \sum_{n=0}^{N-1} \sum_{m=0}^{M-1} \int_{(n-\frac{1}{2})\Delta f_y}^{(n+\frac{1}{2})\Delta f_y} \int_{(m-\frac{1}{2})\Delta f_x}^{(m+\frac{1}{2})\Delta f_x} \exp\{i\phi_{m,n} + \\ & i h_{m,n} \cos\left(\frac{2\pi b f_x}{\Delta f_x}\right)\} \exp\{-2\pi i (k f_x \Delta x' + l f_y \Delta y')\} \mathrm{d}f_x \mathrm{d}f_y, \end{aligned} \tag{2.18}$$

where M and N are the total number of filter pixels in the x and y directions, and

Δf_x and Δf_y are the pixel sizes of the filter in the f_x and f_y directions. The integrals can be evaluated independently of the sums, resulting in the expression for the field in the image plane,

$$A_{k,l} = \frac{L^2}{MN} \sum_{n=0}^{N-1} \sum_{m=0}^{M-1} \exp\{i[\phi_{m,n} - 2\pi(mk/M + nl/N)]\} S_{m,n}(k,l), \tag{2.19}$$

where $\phi_{m,n}$ is the discretized phase of the complex filter of the pixel (m,n). $S_{m,n}(k,l)$ is a scattering function of both the filter position and the image position. According to Eq. (2.19), $S_{m,n}$ acts as the amplitude transmittance, $W(\mathbf{r})$, which is expressed as

$$\begin{aligned} S_{m,n}(k,l) &= \frac{1}{4\pi^2} \int_{-\pi}^{\pi} \int_{-\pi}^{\pi} \exp\{i[h_{m,n}\cos(bu) - ku/M - lv/N]\} \mathrm{d}u\mathrm{d}v \\ &= \frac{1}{4\pi^2} \int_{-\pi}^{\pi} \exp\{i[h_{m,n}\cos(bu) - ku/M]\} \mathrm{d}u \int_{-\pi}^{\pi} \exp\{-ilv/N\} \mathrm{d}v, \end{aligned} \tag{2.20}$$

where $u = 2\pi f_x/\Delta f_x$ and $v = 2\pi f_y/\Delta f_y$. Appendix A gives a full step-by-step derivation of these formulas. Here, the scattering function $S_{m,n}$ is further simplified. According to Hansen-Bessel Formula, $J_n(x) = \frac{1}{2\pi}\int_{-\pi}^{\pi} e^{in(\tau - \frac{\pi}{2})} e^{ix\cos\tau} d\tau = \frac{i^{-n}}{2\pi}\int_{-\pi}^{\pi} e^{i(n\tau + x\cos\tau)} d\tau$,

$$\int_{-\pi}^{\pi} \exp\{i[h_{m,n}\cos(bu) - ku/M]\} \mathrm{d}u = J_{-k/M}(h_{m,n}) = (-1)^{n'} J_{n'}(h_{m,n}), \quad if\ n' = k/M \in integer, \tag{2.21}$$

and

$$\int_{-\pi}^{\pi} \exp\{-ilv/N\} \mathrm{d}u = -2\frac{\sin(\pi l/N)}{l/N} = -2\pi \mathrm{sinc}(\pi l/N). \tag{2.22}$$

Thus, $S_{m,n} = (-1)^{n'}(-2\pi) J_{n'}(h_{m,n})\mathrm{sinc}(\pi l/N)$ when k/M is an integer. Therefore, the intensity of the superoscillatory spot, located at point k, is exactly the same as the designed order ($h_{m,n} = J_{n'}^{-1}(W(\mathbf{r}_L))$ when $k/M = n'$ and l/N is 0. We can expect infinite diffraction orders along x axis, among which again only one diffraction order

matches that of the complex filter but no multiple diffraction orders along y axis.

According to the relation of $a = 2\pi b/\Delta x = 2\pi Mb/L$, we can adjust the carrier frequency through both b and the total number of pixels, M. Figure 2.12 shows the intensity distributions of a superoscillatory field created by a phase-only filter, with $M = 31$ and $M = 61$, and $b = 1$ for both cases. Since the ratio of the central lobe and the side lobe is closer to that of the designed superoscilllatory field for the filter with a larger number of pixels, we can say that the superoscillation is better preserved with a higher carrier frequency, a.

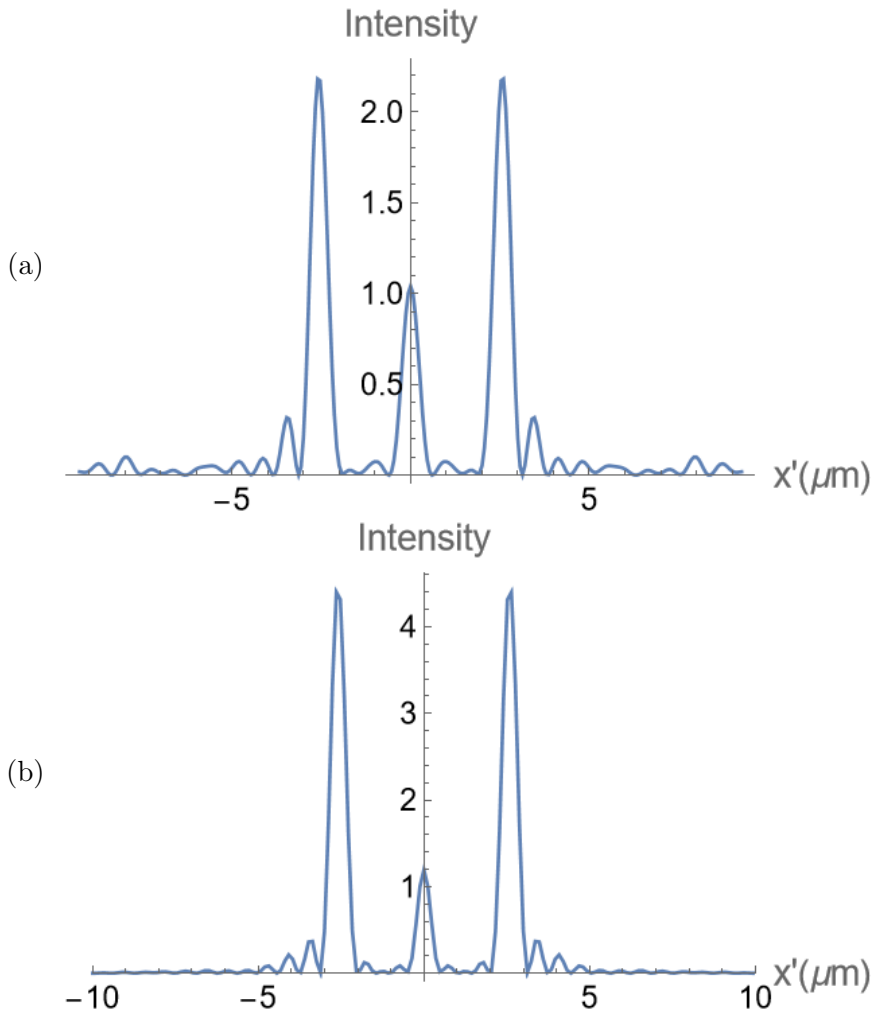

Figure 2.12: Reproduced superoscilllatory field by a phase-only filter with (a) $M = 31$, $\Delta x = 2\,\text{mm}$, $b = 1$ and (b) $M = 61$, $\Delta x = 1\,\text{mm}$, $b = 1$; with superoscillatory spot size, r_{spot}=0.94λ.

Our images so far have been cross-sections of the total field along the axis of diffraction x; it is also useful to see what the full two-dimensional intensity structure looks like. Fig.2.13 shows the image field formed by a filter 31 pixels with one sinusoidal period and two sinusoidal periods within each pixel, respectively. Doubling sinusoidal cycles is equivalent to doubling the pixel number, and leads to a doubled separation between each order.

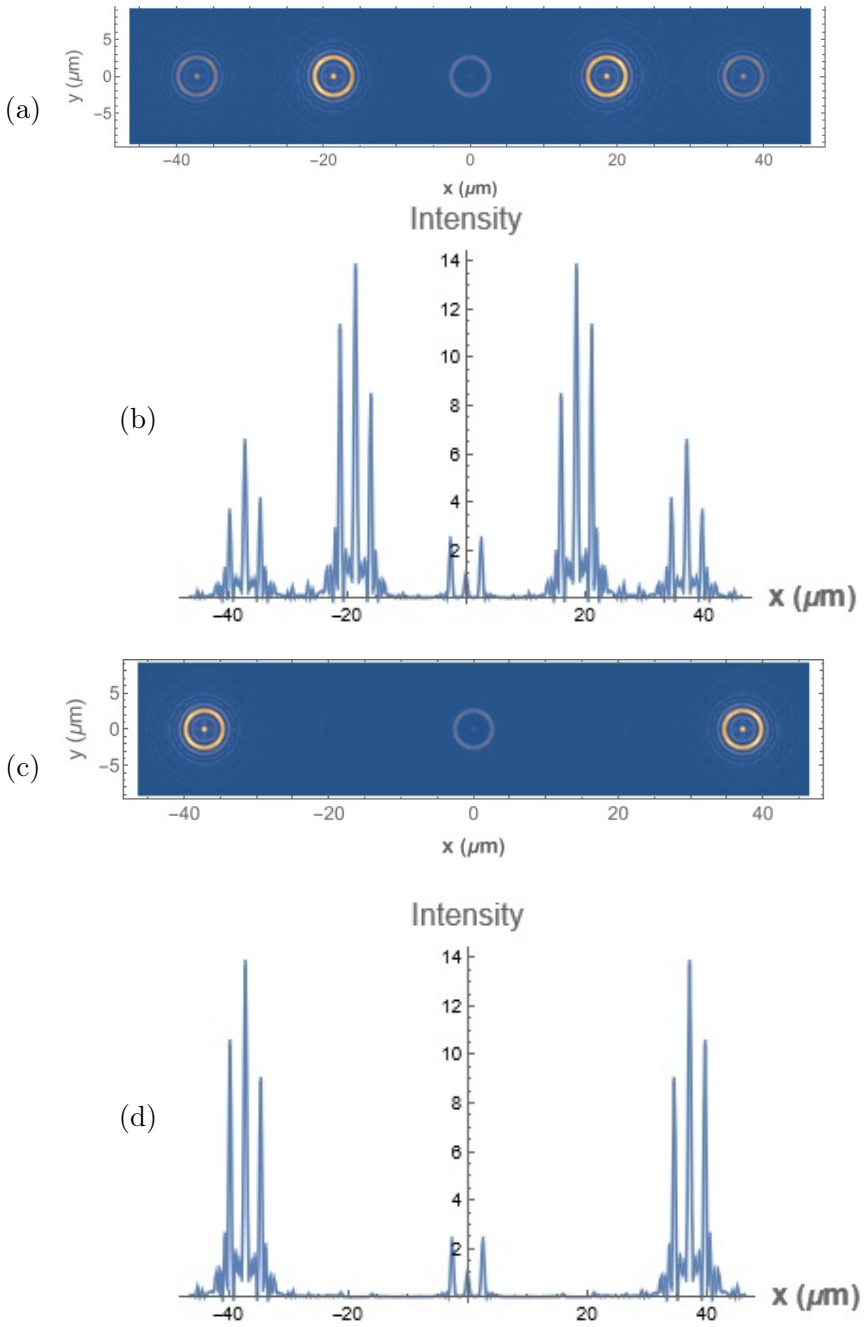

Figure 2.13: Superoscillatory field formed by a phase-only filter in the image space with (a) M=31, $\Delta x = 2\,\mathrm{mm}$, b=1 in two dimensions and (b) in one dimension, (c) M=31, $\Delta x = 1\,\mathrm{mm}$, b=2 in two dimensions, and (d) in one dimensio; with 0^{th} order superoscillatory spot size, r_{spot}=0.94λ.

Fig. 2.14 shows a wide superoscillatory field formed by a phase-only filter in the image space with $M = 31$, $\Delta x = 2\,\mathrm{mm}$, $b = 1$ in 1D. It is noted that most of the energy is distributed to the first four orders.

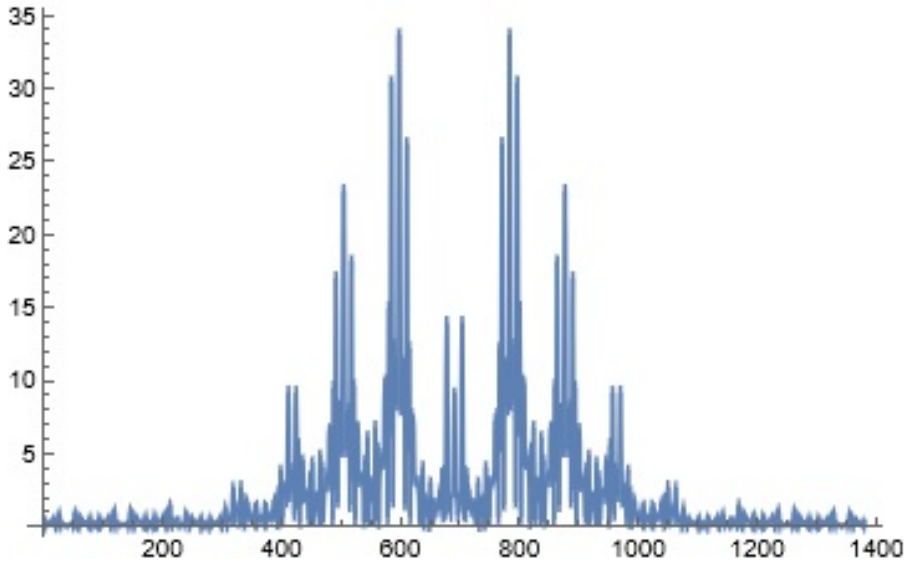

Figure 2.14: A wide superoscillatory field formed by a phase-only filter in the image space with $M = 31$, $\Delta x = 2\,\mathrm{mm}$, $b = 1$ in one dimension.

It is to be noted that the calculation takes very long time by using this method. As for a filter with $M * N$ pixels, to calculate the two-dimensional field with $K * L$ points, M*N*K*L integrals associated with the scattering function $S_{m,n}(k, l)$ need to be calculated. For a filter with $31 * 31$ pixels, the field points are $31 * 31 * 5$ in order to cover $0, \pm 1, \pm 2$ orders which involves $5 * 31^4 = 4,617,605$ integrals. Therefore, the following method which approximates the phase profile by a step-wise binary filter is applied for achieving a faster computation.

2.4.3 Estimation of the minimum number of pixels

As there are multiple orders in the image field, another effect of the change in pixel number, and corresponding change in a, is that the different diffraction orders move closer together and eventually overlap. The minimum pixel number needed to keep the orders separate can be estimated by

$$M = \frac{L}{\Delta x} = \frac{L}{\Delta f_x \lambda d_{\mathrm{I}}} = \frac{L \times L_{\mathrm{img}}}{\lambda d_{\mathrm{I}}}, \tag{2.23}$$

where L_{img} is the range of the designed superoscillatory field, L is the length of the filter, Δx is the pixel size, Δf_x is the pixel size in spatial frequency domain, and d_I is the image distance. In this study, the minimum range of the superoscillatory field is the distance between the two side lobes is about $6\,\mu$m. Thus, the minimum number of pixels is calculated to be 10. In other words, when $\mathrm{M} \leq 10$, the side lobes of the adjacent orders will start colliding into each other. Apparently, when $M = 10$, the central lobe will not be resolved according to the pixel size criterion. Therefore, the pixel size criterion is more stringent than the order separation criterion.

2.5 Step-wise Phase-only Filtering Device

2.5.1 Phase profile

A step-wise phase-only filter is step-wise approximation to the sinusoidal phase profile of the phase-only filter. Fig.2.15 shows the profile of the step-wise filter with each sinusoidal period approximated by 9 steps.

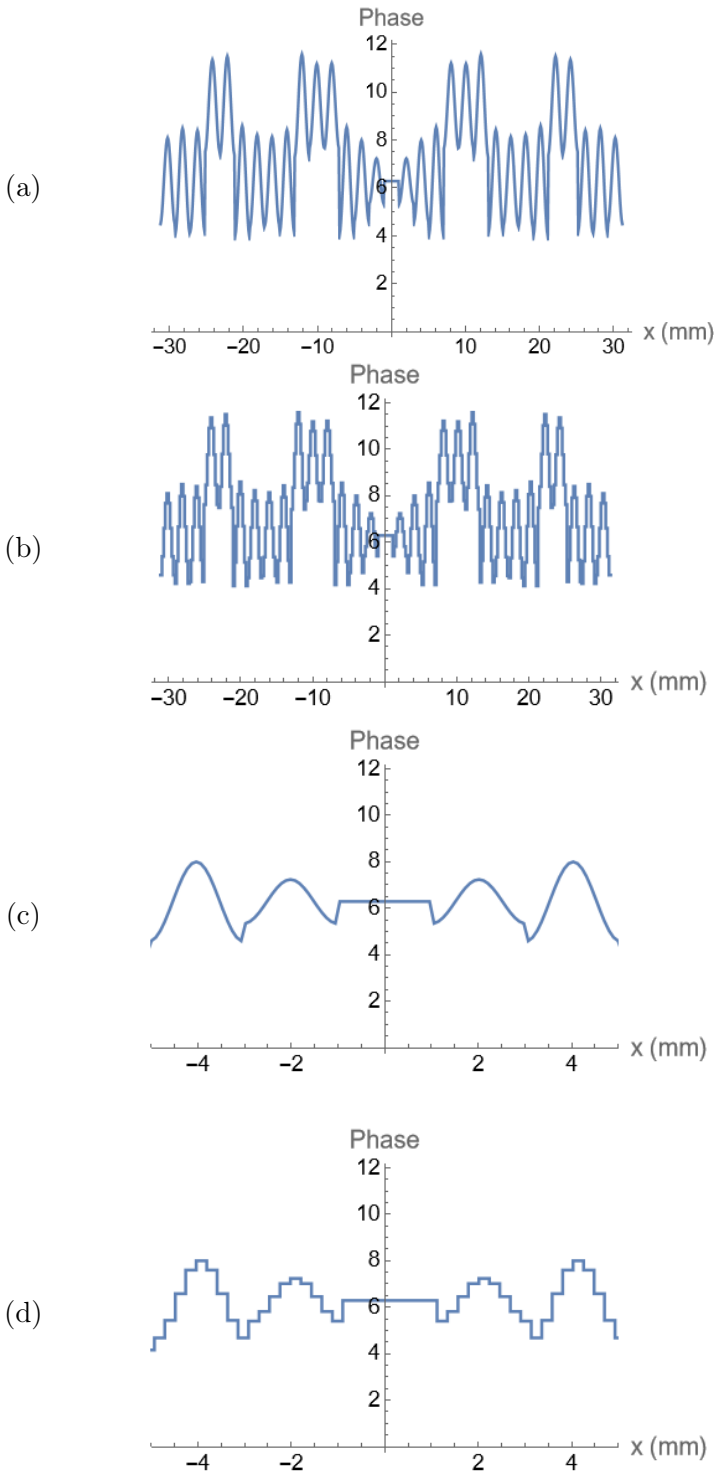

Figure 2.15: Phase-only filter with (a) smooth sinusoidal phase profile of $M = 31$, $\Delta x = 2\,\text{mm}$, $b = 1$, (b) step-wise phase profile of 9 steps in each sinusoidal period, (c) smooth sinusoidal phase profile zoomed in for the central area, and (d) step-wise phase profile of 9 steps in each sinusoidal period zoomed in for the central area.

2.5.2 Superoscillatory image field

For a step-wise phase-only filter, the field emitted from each step is considered uniform across the window of a single step. Therefore, the two-dimensional superoscillatory field distribution is calculated using the Fast Fourier transform (FFT), which is much more efficient than the window Fourier transform. Fig. 2.16 shows the intensity distribution of the five lowest diffraction orders for a binary phase-only filter approximated by 21 steps. As expected, only the 0^{th} order reproduces the designed superoscillatory pattern. Figure 2.17 shows the cross section of the intensity distribution ($y' = 0$) of (a) five orders and (b) the 1^{st} order and 2^{nd} order in more detail, in the direction of x'. It can be seen that these higher orders do not possess an isolated superoscillatory spot and are therefore unsuitable for imaging. It is noted that the ± 1 order and ± 2 order has different field distributions from that of the phase-only filter, which might caused by the step-wise profile of the step-wise phase-only filter.

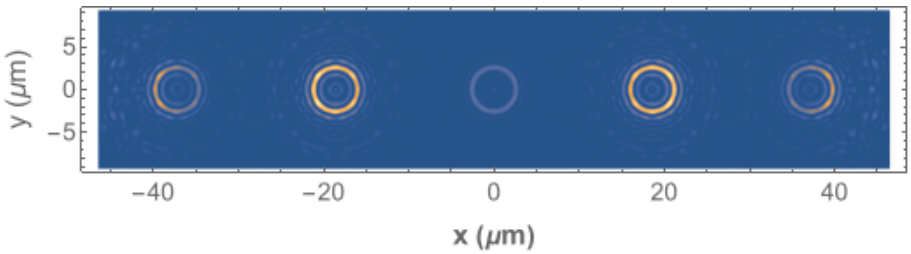

Figure 2.16: Three orders of superoscilllatory field formed by a step-wise phase-only filter in two-dimensional image space with $M = 31$, $\Delta x = 2\,\text{mm}$, and $b = 1$; with superoscillatory spot size, r_{spot}=0.94λ.

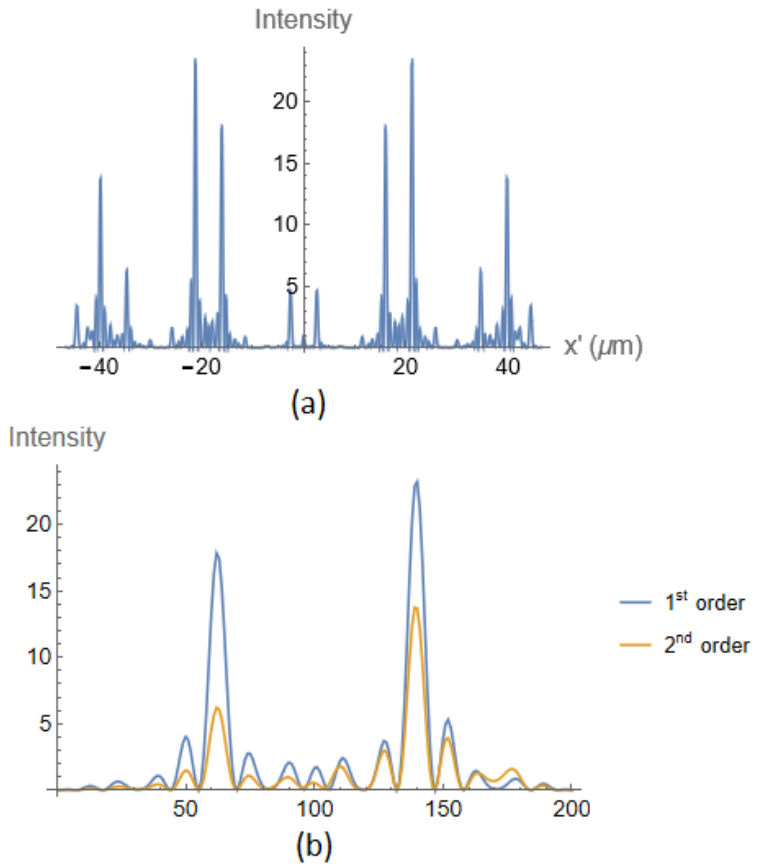

Figure 2.17: Cross section ($y' = 0$) of superoscillatory field formed by a step-wise phase-only filter of (a) three orders, (b) the 1st order and the 2nd, with $M = 31$, $\Delta x = 2\,\text{mm}$, and $b = 1$.

2.6 Comparison Between the Designed Filters

Though a phase-only filter transmits 100% of the energy incident upon it, and would in principle seem to be more efficient than the complex filter, Figure 2.16 indicates that a significant amount of energy goes into the unused diffraction orders. Therefore, we compare the energy efficiency of the complex filter, amplitude filter, and phase filter.

2.6.1 Complex filter

The total energy efficiency of a filter is given by the ratio of the total transmitted energy and the total input energy. By assuming the input energy is uniform across the complex filter, the total energy efficiency is the integration of the amplitude

transmittance in 2D divided by the filter area. For a pixelated complex filter, the total energy efficiency is simply the numerical summation of the amplitude transmittance of each pixel. As the complex filter produces a single 0^{th} order without other diffraction orders, the total energy efficiency is also that of the 0^{th} order. Here, η_c is referred to as the total efficiency and η_{c0} is referred to as the "0^{th} order" efficiency, which is given by

$$\eta_c = \eta_{c0} = \frac{\int_L |W(\mathbf{r}_\text{L})|^2 \, \mathrm{d}\mathbf{r}_\text{L}^2}{\int_L \mathrm{d}\mathbf{r}_\text{L}^2} = \Sigma_n^N \Sigma_m^M W_{m,n}, \tag{2.24}$$

where the integral is over the area of the lens L, $W_{m,n}$ is the amplitude transmittance of a single pixel. Table 1 lists the energy efficiency of the complex filter.

Table 2.1: **Energy efficiency of the complex filter**

Order	Energy efficiency (%)
0	6.3
Total	6.3

2.6.2 Amplitude-only filter

For an amplitude-only filter, as the cosine term is expressed as the sum of two exponential terms, it has 3 orders: 0^{th} order, and $\pm 1^{\text{st}}$ orders.

Based on the expression of the transmittance of an amplitude-only filter:

$$A(\mathbf{r}_\text{L}) = A_0 + 2\Delta A(|W(\mathbf{r}_\text{L})|/W_{\max}) \cos\{2\pi a x + \phi(\mathbf{r}_\text{L})\}, \tag{2.25}$$

the energy efficiency of the $\pm 1^{\text{st}}$ orders is given by

$$\eta_{a1} = \frac{\varepsilon_{a1}}{\varepsilon_{in}} = C_a^2 \frac{\int_L |W(\mathbf{r}_\text{L})|^2 \, \mathrm{d}^2\mathbf{r}_\text{L}}{\int_L \mathrm{d}^2\mathbf{r}_\text{L}}, \tag{2.26}$$

where ε_1 is the energy of the 1^{st} order and $C_a = \Delta A/W_{\max}$, $\Delta A = \beta\Delta\alpha/4$, $0 < \beta \leq 1$.

Then, the total energy efficiency of an amplitude-only filter is given by

$$\begin{aligned}\eta_a =& A_0^2 + 2C_a^2 \frac{\int_L |W(\mathbf{r}_\mathrm{L})|^2 \,\mathrm{d}^2\mathbf{r}_\mathrm{L}}{\int_L \mathrm{d}^2\mathbf{r}_\mathrm{L}} \\ =& (\alpha_0 + \frac{\Delta\alpha}{2})^2 + 2C_a^2 \frac{\int_L |W(\mathbf{r}_\mathrm{L})|^2 \,\mathrm{d}^2\mathbf{r}_\mathrm{L}}{\int_L \mathrm{d}^2\mathbf{r}_\mathrm{L}},\end{aligned} \tag{2.27}$$

where $A_0 = \alpha_0 + \frac{\Delta\alpha}{2}$, $0 < \alpha_0 \leq 1$, $0 < \Delta\alpha \leq 1 - \alpha_0$.

The energy efficiency depends on α_0, $\Delta\alpha$, and β; overall, we expect the energy efficiency of an amplitude filter to be low. To estimate the maximum possible efficiency, we discretize the three parameters into three sequences, then calculate the energy efficiency for all combinations of the three parameters. Table 2 lists the α_0, $\Delta\alpha$, and β, which lead to the maximum energy efficiency of the $\pm 1^{\mathrm{st}}$ order and the corresponding total energy efficiency and the $\pm 1^{\mathrm{st}}$ order efficiency. As can be seen from the table, the vast majority of energy goes into the unusable 0^{th} order spot.

Table 2.2: **Energy efficiency of the designed amplitude-only filter**

α_0	0
$\Delta\alpha$	1
β	1
Total energy efficiency (%)	25.7
Maximum 1^{st} order efficiency (%)	0.37

2.6.3 Phase-only filter

Since phase-only filters transmit all incident light, they have a total energy efficiency of one. As introduced in Section 2.4, the transmittance of a phase-only filter is given by

$$T(\mathbf{r}_\mathrm{L}) = e^{i\phi(\mathbf{r}_\mathrm{L})} e^{ih(\mathbf{r}_\mathrm{L})\cos(ax)}. \tag{2.28}$$

By applying the property $e^{iz\cos(x)} = \sum_{n=-\infty}^{\infty} i^n J_n(z) e^{inx}$, we have

$$T(\mathbf{r}_\mathrm{L}) = e^{i\phi(\mathbf{r}_\mathrm{L})} \sum_{n=-\infty}^{\infty} i^n J_n[h(\mathbf{r}_\mathrm{L})] e^{inax}, \tag{2.29}$$

where $h(\mathbf{r}_\mathrm{L})$ is again taken to be $h(\mathbf{r}_\mathrm{L}) = J_0^{-1}[W(\mathbf{r}_\mathrm{L})]$; thus the superoscillatory field is carried by the 0^{th} order of the designed filter. The transmittance of the 0^{th} order is

$$T_0(\mathbf{r}_\mathrm{L}) = e^{i\phi(\mathbf{r}_\mathrm{L})} J_0[h(\mathbf{r}_\mathrm{L})]. \tag{2.30}$$

The energy efficiency of the 0^{th} order is

$$\eta_0 = \frac{\varepsilon_0}{\varepsilon_{in}} = \frac{\int_L |J_0[h(\mathbf{r}_\mathrm{L})]|^2 \, \mathrm{d}^2\mathbf{r}_\mathrm{L}}{\int_L \mathrm{d}^2\mathbf{r}_\mathrm{L}}, \tag{2.31}$$

where ε_0 is the energy of the 0^{th} order and ε_{in} is the input energy of the filter. Similarly, the transmittance of the 1^{st} order is

$$T_1(\mathbf{r}_\mathrm{L}) = e^{i\phi(\mathbf{r}_\mathrm{L})} i J_1[h(\mathbf{r}_\mathrm{L})] e^{inax}. \tag{2.32}$$

The energy efficiency of the 1^{st} order is

$$\eta_1 = \frac{\varepsilon_1}{\varepsilon_{in}} = \frac{\int_L |J_1[h(\mathbf{r}_\mathrm{L})]|^2 \, \mathrm{d}^2\mathbf{r}_\mathrm{L}}{\int_L \mathrm{d}^2\mathbf{r}_\mathrm{L}}, \tag{2.33}$$

where $\varepsilon_1$is the energy of the 1^{st} order. Table 3 summarizes the energy efficiency of the phase-only filter designed for the 0^{th} order. The design of the phase-only filter suggests that the energy efficiency of the filter should be effectively the same as the corresponding complex filter.

Table 2.3: **Energy efficiency of the designed phase-only filter**

Order	Energy efficiency (%)
0	6.3
+/-1	32.1
+/-2	12.7
Total	100

The energy distribution of different Bessel function orders of a phase-only filter is determined by the n' applied in the calculation of $h(\mathbf{r}_\mathrm{L}) = J_{n'}^{-1}[W(\mathbf{r}_\mathrm{L})]$. Here, we also

investigate the cases of phase-only filters designed with different n'. It is noticeable that $h(\mathbf{r}_\mathrm{L}) = J_{n'}^{-1}[W(\mathbf{r}_\mathrm{L})]$ does not exist for some orders of n' for $W(\mathbf{r}_\mathrm{L})$ larger than a certain value, since different Bessel function orders have different maximum values. To solve the problem, one way is to scale the $W(\mathbf{r}_\mathrm{L})$ to the range of the Bessel function order of n', which will affect the energy distribution of different Bessel function orders. Figure 2.18 shows the energy efficiency distributions of phase-only filters designed with $n' = 0, 1, 2$, by taking out the points of $h(\mathbf{r}_\mathrm{L})$ that do not exist to get a rough estimation without scaling down $W(\mathbf{r}_\mathrm{L})$. For the three filters, the superoscillatory field is carried by the 0^{th}, the 1^{st}, and the 2^{nd} Bessel function order, and the energy efficiency is 6.3%, 5.7%, and 5.6% respectively. There is a slight decrease in the energy efficiency when the filter is designed for higher orders.

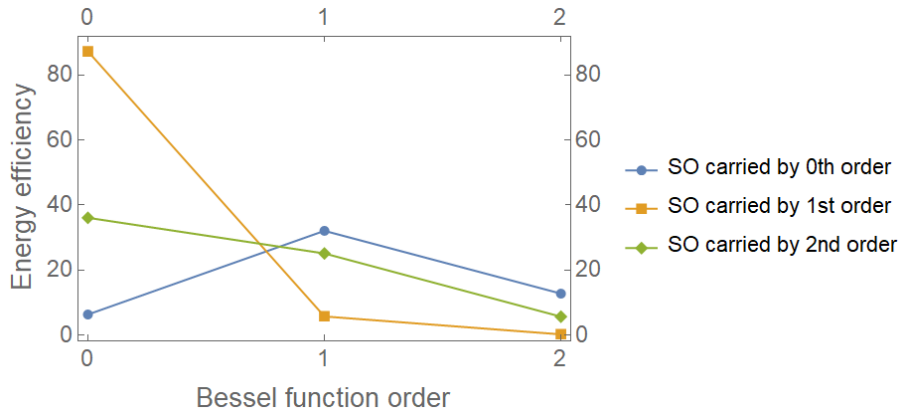

Figure 2.18: Energy efficiency distribution of phase-only filters with different order to carry superoscillatory field, with $M = 151$, $\Delta x = 0.4\,\mathrm{mm}$

.

Based on the energy efficiency results listed in Table 1, Table 2, and Table 3, a phase-only filter will have energy efficiency comparable to the complex filter. The amplitude-only filter always has a significantly lower energy efficiency.

2.7 Discussion and Conclusion

The design method in this study can be applied to a wide range of optical systems, not limited to microscopes. The design method is universal and straightforward. By

utilizing this method, theoretically, an infinitely small spot size can be achieved in the image plane. However, the smaller the spot is, the less intensity remains in the central lobe and more energy goes into the sidelobes. Therefore, there is a balance between the image resolution and the image brightness. Admittedly, the sidelobe with high intensity will affect the imaging process, thus the issue needs to be solved in following studies. Furthermore, modifications can be made by combining the superoscillatory filter with the refractive lens to simplify the imaging system.

In terms of manufacturing, among the three types of filters, the phase-only filter is the easiest to make by etching a varying thickness across a transparent surface. There are many possible ways to make such a filter, however. For example, sinusoidal patterns can be formed by shining fringe patterns from interferometers on photoresist materials. In addition, gradient index materials and electron beam lithography can be applied. An amplitude-only filter is made by creating a varying transmittance across the surface, which is more difficult to realize. Apparently, a complex filter needs both techniques, thus it is most challenging to manufacture.

In terms of energy efficiency, a phase-only filter has a higher energy efficiency compared with an amplitude-only filter. The total energy efficiency of the phase-only filter is 100%. The total energy efficiency of the amplitude-only filter depends on both the arbitrary settings of the filter parameters and the transmittance function of the filter.

Our results show that it is possible to modify the design technique of Smith and Gbur to phase-only or amplitude-only filters with a finite number of pixels, and that these changes can be made without destroying the superoscillations of the transmitted field. Criteria have been given to guide researchers in the design of such filters. It is to be noted that there are other strategies for producing phase-only or amplitude-only filters that might give improved performance; see, for example, Ref. [63]. Our work will hopefully motivate additional research into analytic techniques for designing

superoscillatory filters.

CHAPTER 3: VECTOR SUPEROSCILLATORY FIELD ILLUMINATION

3.1 Introduction

Since superoscillatory waveforms are inevitably surrounded by high intensity sidelobes, the usable super-resolved area of an image is severely limited. A few earlier studies have been done on eliminating the sidelobes. One approach is based on optimization using algorithms, such as genetic algorithm [64]. The designed superoscillatory field can have sidelobes eliminated, but the design of the superoscillatory lenses relies excessively on optimization and faces challenges in mask fabrications. Another study fabricated a pair of meniscus shape apertures, which lead to superoscillatory wave without sidelobes based on the Poisson-Arago phenomenon [65]. The goal of Chapter 3 is to use electromagnetic wave properties to get around the sidelobes. In Chapter 3, section 3.2 describes transverse nature of light. Section 3.3 demonstrates how polarization engineering can be used in some circumstances to suppress superoscillation sidelobes by taking advantage of the transverse wave nature of light. Section 3.4 and section 3.5 illustrate the principle by a model super-resolution imaging system that can image Rayleigh scatterers with separations smaller than the classic Rayleigh criterion. The factors that can affect the quality of the super-resolved image are discussed. In section 3.6, the polarization distribution at the aperture plane is calculated, and a device to form the vector superoscillatory field is proposed.

3.2 Transverse Nature and Polarization of Light

Light is an electromagnetic (EM) wave that consists of oscillations of both the electric field and the magnetic field. In a homogeneous and isotropic medium, the electric field and the magnetic field are perpendicular to each other and propagate in

the direction perpendicular to both fields, thus the EM field is a transverse wave.

According to the Fresnel's wave theory, the electric field can be described by two orthogonal electric field components, E_x and E_y, which satisfy the wave equation and their solutions, propagating in the z direction, are given by

$$E_x(\boldsymbol{r}, t) = E_{0x}\cos(\omega t - kz + \delta_x), \tag{3.1}$$

and

$$E_y(\boldsymbol{r}, t) = E_{0y}\cos(\omega t - kz + \delta_y), \tag{3.2}$$

where k is the wave number, E_{0x} and E_{0y} are the amplitude of the electric field components, and δ_x and δ_y are arbitrary phases. Accordingly, by eliminating the term $\omega t - kz$, the two electric components in both directions form an ellipse in the form of,

$$\frac{E_x(z,t)^2}{E_{0x}^2} + \frac{E_y(z,t)^2}{E_{0y}^2} - \frac{2E_x(z,t)E_y(z,t)}{E_{0x}E_{0y}}\cos(\delta) = \sin^2(\delta). \tag{3.3}$$

In this case, the electric field is called elliptically polarized. The magnetic field is elliptically polarized as well.

When $\delta_x - \delta_y = m\pi$ $(m = 0, \pm\ 1, \pm 2, ...)$, E_x and E_y oscillate in phase, and the polarization ellipse degenerates to a line, for which light is linearly polarized. In this thesis, linear polarization is applied as the polarization state of EM fields. When $\delta_x - \delta_y = (2m+1)\pi/2$ $(m = 0, \pm\ 1, \pm 2, ...)$ and $E_{0x} = E_{0y}$, E_x and E_y oscillate with a phase difference of $\pi/2$, and the polarization ellipse becomes a circle, for which the light field is circularly polarized.

3.2.1 Direction of polarization

Throughout the history of optics, the direction of the magnetic vector is often called the direction of polarization.The plane containing the magnetic vector and the

direction of propagation is called the plane of polarization. However, some places define the two quantities with respect to the electric vector [66]. In this thesis, the later definition is used.

3.2.2 Stokes parameters

Stokes parameters are four quantities that specify the polarization state of an electromagnetic field, which are given in normalized form by

$$s_1 = s_0 \cos(2\chi)\cos(2\psi), \tag{3.4}$$

$$s_2 = s_0 \cos(2\chi)\sin(2\psi) = s_1 \tan(2\psi), \tag{3.5}$$

$$s_3 = s_0 \sin(2\chi), \tag{3.6}$$

$$s_0^2 = s_1^2 + s_2^2 + s_3^2, \tag{3.7}$$

where $\chi = \arctan\frac{b}{a}$ (b and a are the minor axis and the major axis of the polarization ellipse) is the ellipticity and ψ is the orientation of the polarization ellipse (the angle between the direction of the major axis and E_x). In this thesis, Stokes parameters are calculated from the vector electric field components $\boldsymbol{E}_x$ and $\boldsymbol{E}_y$. First, linearly polarized electric fields at 45 and 135 degree, and left-handed and right-handed circularly polarized fields are given by

$$\boldsymbol{E}_{45} = \frac{\sqrt{2}}{2}(\boldsymbol{E}_x + \boldsymbol{E}_y), \tag{3.8}$$

$$\boldsymbol{E}_{135} = \frac{\sqrt{2}}{2}(-\boldsymbol{E}_x + \boldsymbol{E}_y), \tag{3.9}$$

$$\boldsymbol{E}_l = \frac{\sqrt{2}}{2}(\boldsymbol{E}_x + i\boldsymbol{E}_y), \tag{3.10}$$

$$\boldsymbol{E}_r = \frac{\sqrt{2}}{2}(\boldsymbol{E}_x - i\boldsymbol{E}_y). \tag{3.11}$$

Second, the unnormalized Stokes parameters are given by

$$S_0 = |\boldsymbol{E}_x|^2 + |\boldsymbol{E}_y|^2, \tag{3.12}$$

$$S_1 = |\boldsymbol{E}_x|^2 - |\boldsymbol{E}_y|^2, \tag{3.13}$$

$$S_2 = -(|\boldsymbol{E}_{45}|^2 - |\boldsymbol{E}_{135}|^2), \tag{3.14}$$

$$S_3 = -(|\boldsymbol{E}_l|^2 - |\boldsymbol{E}_r|^2). \tag{3.15}$$

Third, the normalized Stokes parameters are given by

$$s_0 = \frac{S_0}{S_0},\ s_1 = \frac{S_1}{S_0}, \tag{3.16}$$

$$s_2 = \frac{S_2}{S_0},\ s_3 = \frac{S_3}{S_0}. \tag{3.17}$$

The orientation angle ψ of polarization can be expressed by Stokes parameters as:

$$\psi = -\frac{1}{2}\arctan(s_1 + i\, s_2). \tag{3.18}$$

3.2.3 Jones vector and matrix

Jones vector is a 2×1 vector describes the electric field components, $\boldsymbol{E}_x$ and $\boldsymbol{E}_y$, and Jones matrix is a 2×2 matrix describes the polarizing components in the optical system. The electric field transmitted by an optical component is given by

$$\begin{bmatrix} \boldsymbol{E}'_x \\ \boldsymbol{E}'_y \end{bmatrix} = \begin{bmatrix} a_1 & a_2 \\ a_3 & a_4 \end{bmatrix} \begin{bmatrix} \boldsymbol{E}_x \\ \boldsymbol{E}_y \end{bmatrix}, \tag{3.19}$$

where a_1 to a_4 are expressions that describe the polarizing element.

3.3 Rayleigh Scattering and Concept of Sidelobe Suppression

3.3.1 Polarization dependence of Rayleigh scattering

Rayleigh scattering is the scattering of a linearly-polarized paraxial electromagnetic wave by a subwavelength-size sphere lying in a transverse plane, where the radius of the sphere is a and $a \ll \lambda$. The intensity distributions of the scattered light at distance l in the far field ($l \gg \lambda$) in the plane perpendicular to the polarization direction and in the plane parallel to the polarization direction satisfy the respective equations [67]:

$$I_1 = I_0 \frac{16\pi^4 a^6 (\frac{n^2-1}{n^2+2})^2}{\lambda^4 l^2}, \tag{3.20}$$

and

$$I_2(\theta) = I_0 \frac{16\pi^4 a^6 (\frac{n^2-1}{n^2+2})^2}{\lambda^4 l^2} \sin^2\theta, \tag{3.21}$$

where I_0 is the intensity of the field incident on the particle and n is the refractive index of the particle. θ is the angle between the polarization direction and the scattering direction. In the plane perpendicular to the polarization direction, the intensity of scattered light is isotropic. In the plane parallel to the polarization direction, the intensity changes as a function of angle θ. Figure 3.1 shows the scattering pattern of a Rayleigh scatterer generated by an incident linearly polarized wave. The intensity of the scattered light vanishes in the polarization direction and reaches the maximum in the direction perpendicular to the polarization direction.

3.3.2 Sidelobe suppression under vector field illumination

The scattering pattern of a Rayleigh scatterer suggests a strategy for sidelobe suppression: by patterning a superoscillatory field such that the central spot and sidelobes are orthogonally polarized, a detector can be placed to select only the central spot scattered light. Such a field is referred to as a vector superoscillatory field (VSF). Figure 3.2 illustrates a superoscillatory field with four zero rings: $r_1 = 0.47\,\mu$m (su-

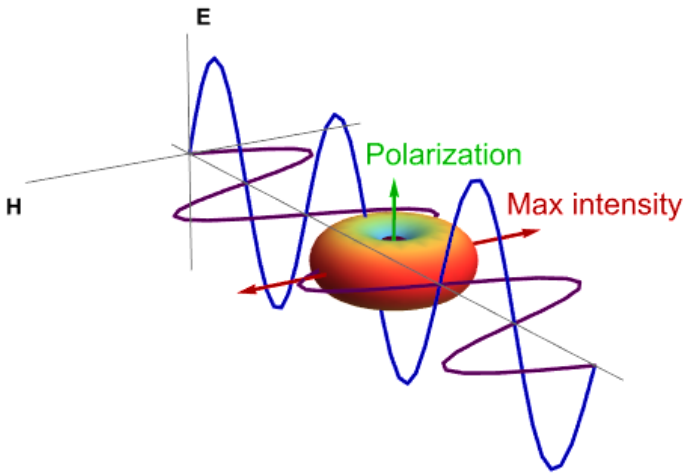

Figure 3.1: Polarization-dependent Rayleigh scattering pattern: scattering pattern of a scatterer by interacting with an electromagnetic wave.

peroscillatory spot radus; by assuming λ=500nm, r_1=0.94λ), $r_2 = 1\,\mu$m, $r_3 = 1.48\,\mu$m, and $r_4 = 2\,\mu$m; orthogonal linear polarization states are imposed for the central spot and the sidelobes to make a VSF. Scatterers located in the two regions produce Rayleigh scattering patterns with perpendicular orientations. The dashed arrows indicate the directions where only the central spot scattered light. Thus, if a detector is placed facing that direction, only the scattered light of the central spot will be detected; the light from the sidelobes is scattered elsewhere.

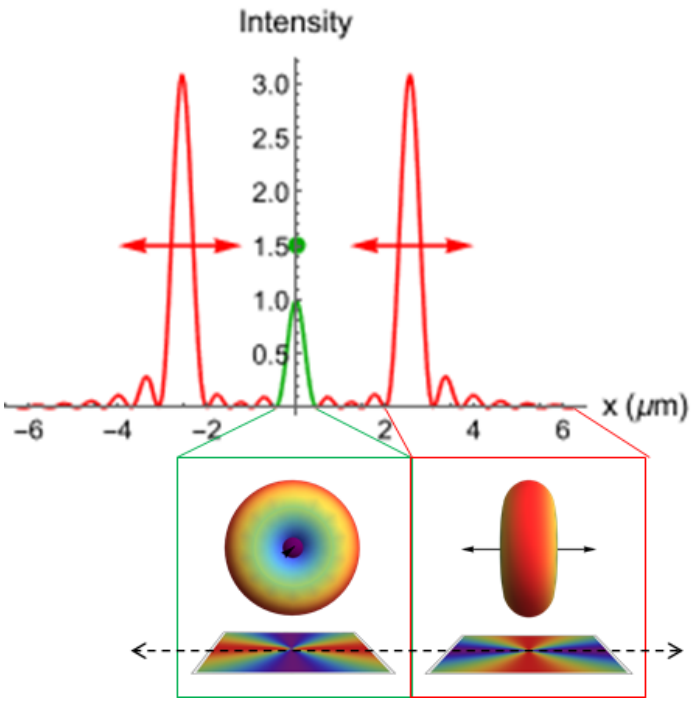

Figure 3.2: Scattering patterns of scatterers under the illumination of the central spot and the sidelobes in a superoscillatory field with orthogonal linear polarization states.

3.4 A Super-resolution System with Vector Superoscillatory Field Illumination

The observation of variations in scattering patterns under different polarization states suggests a possible measurement scheme for creating super-resolution imaging of Rayleigh particles. Figure 3.3 shows the front view and the perspective view of the proposed imaging system. In this imaging system, a VSF is formed by a refractive lens with a superoscillatory filter attached to it. Another lens for tailoring the polarization states may be attached, which is described in the latter part of this chapter. The central lobe is y-polarized and the sidelobes are x-polarized. Rayleigh scatterers are placed on a translation stage. Since the sidelobes will not scatter light toward the x direction for the given polarized superoscillatory field, the time-averaged energy flux along the x direction, $\langle \boldsymbol{S} \rangle_x$, serves as the measurement signal. To receive the signal, a detector facing the x direction is placed at a distance L from the center of the stage. The stage performs a raster scan across the VSF in two-dimensional space to cover all

of the scatterers. Here, the instability of the optical path during the scanning process might limit the accuracy of the system.

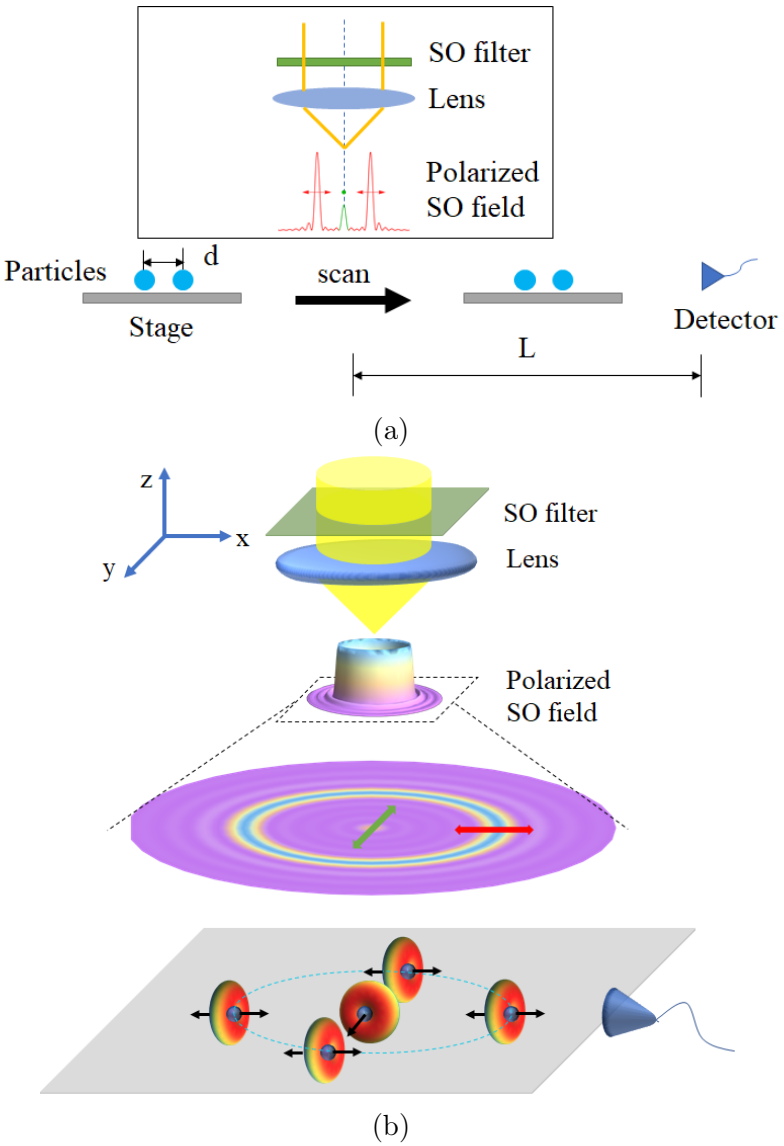

Figure 3.3: A proposed super-resolution imaging system, with (a) the front view and (b) the perspective view.

3.5 Images with Vector Superoscillatory Field Illumination

3.5.1 Foldy-Lax method for calculating multi-scattering

For particles close together (with separations comparable or less than a wavelength) multiple scattering effects become significant and can potentially disrupt the

proposed measurement scheme. Therefore, the total scattered field is evaluated using the venerable Foldy-Lax method [68, 69].

For the first step of the Foldy-Lax method, each individual particle is treated as a dipole in accordance with Rayleigh scattering. Figure 3.4 shows the scattering of an incident wave by two Rayleigh scatterers, which are labeled with index j. Here, both the incident illuminating wave and the scattered wave are vector fields. The illuminating field is scattered off the two particles, producing the secondary spherical wave $\boldsymbol{E}_j^{(s)}(\boldsymbol{r})$, where j represents α_1 or α_2.

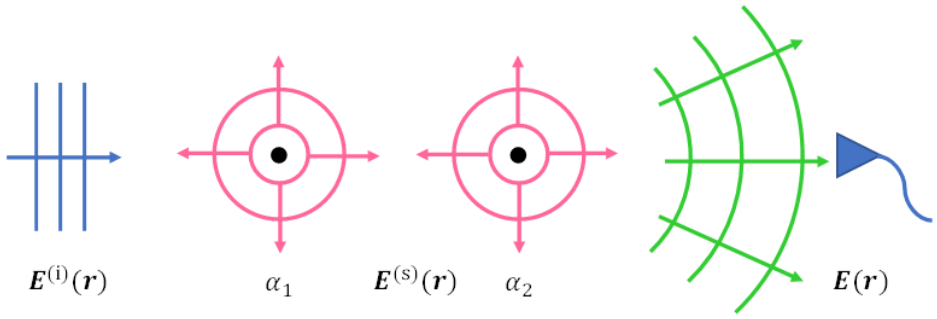

Figure 3.4: Scattering of two Rayleigh particles

For the second step, a total field in regions of the system of particles is the sum of the illuminating field and all scattering fields:

$$\boldsymbol{E}(\boldsymbol{r}) = \boldsymbol{E}^i(\boldsymbol{r}) + \boldsymbol{E}^s(\boldsymbol{r}). \tag{3.22}$$

To be more specific, the total electric field $\boldsymbol{E}(\boldsymbol{r}_i)$ at the location $\boldsymbol{r}_i$ is taken as the sum of the incident field $\boldsymbol{E}^i(\boldsymbol{r}_i)$ and the scattered fields from all the scatterers except the self-energy in the case that a radiating particle is located at position $\boldsymbol{r}_i$, which is expressed as

$$\boldsymbol{E}(\boldsymbol{r}_i) = \boldsymbol{E}^i(\boldsymbol{r}_i) + \Sigma_{i\neq j}\frac{\alpha_j}{\epsilon_0}\boldsymbol{G}(\boldsymbol{r}_i, \boldsymbol{r}_j)\cdot\boldsymbol{E}(\boldsymbol{r}_j), \tag{3.23}$$

where $\boldsymbol{E}(\boldsymbol{r}_j)$ is the total field at a scatterer's location $\boldsymbol{r_j}$ and ϵ_0 is the vacuum permittivity. The quantity $\boldsymbol{G}(\boldsymbol{r}_i, \boldsymbol{r}_j)$ is the Dyadic Green's function representing the electric field at the field point $\boldsymbol{r}_i$ generated by a radiating dipole or a scatterer located at $\boldsymbol{r}_j$, which is of the form,

$$\boldsymbol{G}(\boldsymbol{r}_i, \boldsymbol{r}_j) = [\boldsymbol{I} + \frac{1}{k^2}\nabla\nabla]G(\boldsymbol{r}_i, \boldsymbol{r}_j), \tag{3.24}$$

where $G(\boldsymbol{r}_i, \boldsymbol{r}_j)$ is the scalar Green's function, given by

$$G(\boldsymbol{r}_i, \boldsymbol{r}_j) = \frac{\exp(ik|\boldsymbol{r}_i - \boldsymbol{r}_j|)}{4\pi|\boldsymbol{r}_i - \boldsymbol{r}_j|}, \tag{3.25}$$

and $\boldsymbol{I}$ is the unit dyad. The quantity $\alpha_j = 4\pi\epsilon_0\frac{\epsilon_j - \epsilon_0}{\epsilon_j + 2\epsilon_0}a^2$ is the polarizability of the jth scatterer with ϵ_j as its permittivity. In the simulation, the mesh subdivision is performed on the scattering field. Each scatterer is represented by a single node in the mesh network, as the scatterers are point-like according to the Foldy-Lax method. Eq. (3.23) can then be formulated as a matrix equation and solved for $\boldsymbol{E}(\boldsymbol{r}_i)$. $\boldsymbol{E}(\boldsymbol{r}_i)$ is an array with the electric field at the scatterers as the array elements. In the calculation, the detector is considered as one of the scatterers, with a polarizability of 0. Thus, the electric field at the detector is one of the elements of the calculated $\boldsymbol{E}(\boldsymbol{r}_i)$.

For the third step, the total magnetic field is calculated from the total electric field by Faraday's law,

$$\begin{aligned}\boldsymbol{H}(\boldsymbol{r}_i) =& \frac{1}{i\omega\mu}\nabla \times \boldsymbol{E}(\boldsymbol{r}_i) \\ =& \boldsymbol{H}^i(\boldsymbol{r}_i) + \frac{1}{i\omega\mu}\Sigma_{i\neq j}\frac{\alpha_j}{\epsilon_0}[\nabla \times \boldsymbol{G}(\boldsymbol{r}_i, \boldsymbol{r}_j)] \cdot \boldsymbol{E}(\boldsymbol{r}_j),\end{aligned} \tag{3.26}$$

where $\mathbf{H}^i(\boldsymbol{r}_i)$ is the incident magnetic field at $\boldsymbol{r}_i$.

For the final step, the time averaged Poynting vector of the total field is obtained

by

$$\boldsymbol{S}(\boldsymbol{r}) = \frac{1}{2} Re\{\boldsymbol{E}(\boldsymbol{r}) \times \boldsymbol{H}^*(\boldsymbol{r})\}. \tag{3.27}$$

At large scattering angles, the total Poynting vector will be entirely due to the scattered field. The scattered power in the x direction is calculated as a function of the position of the imaging stage.

3.5.2 Scattering pattern of a single scatterer

To test out the effectiveness of the proposed system in suppressing the sidelobes of the superoscillatory field, the images of Rayleigh scatterers are simulated under a number of illumination conditions. Here, the wavelength of the light source is $\lambda = 500\,\text{nm}$. A refractive lens has a focal length of $f = 50\,\text{mm}$, an object distance of $d_o = 150\,\text{mm}$, an image distance of $d_i = 75\,\text{mm}$, and a diameter of $D = 62.5\,\text{mm}$. The scatterers have a radius of $a = 50\,\text{nm}{=}0.1\lambda$ and a refractive index of $n = 1.5$. Appendix B lists the calculation of the scattered electric and magnetic field with explicit expression of the Dyadic Green function.

Figure 3.5 shows results for a single particle. Figure 3.5 (b) shows that the sidelobe image is almost eliminated when a single scatterer is illuminated by a VSF; Figure 3.5 (c) shows that a superoscillatory field polarized only in the y-direction still manifests large sidelobes.

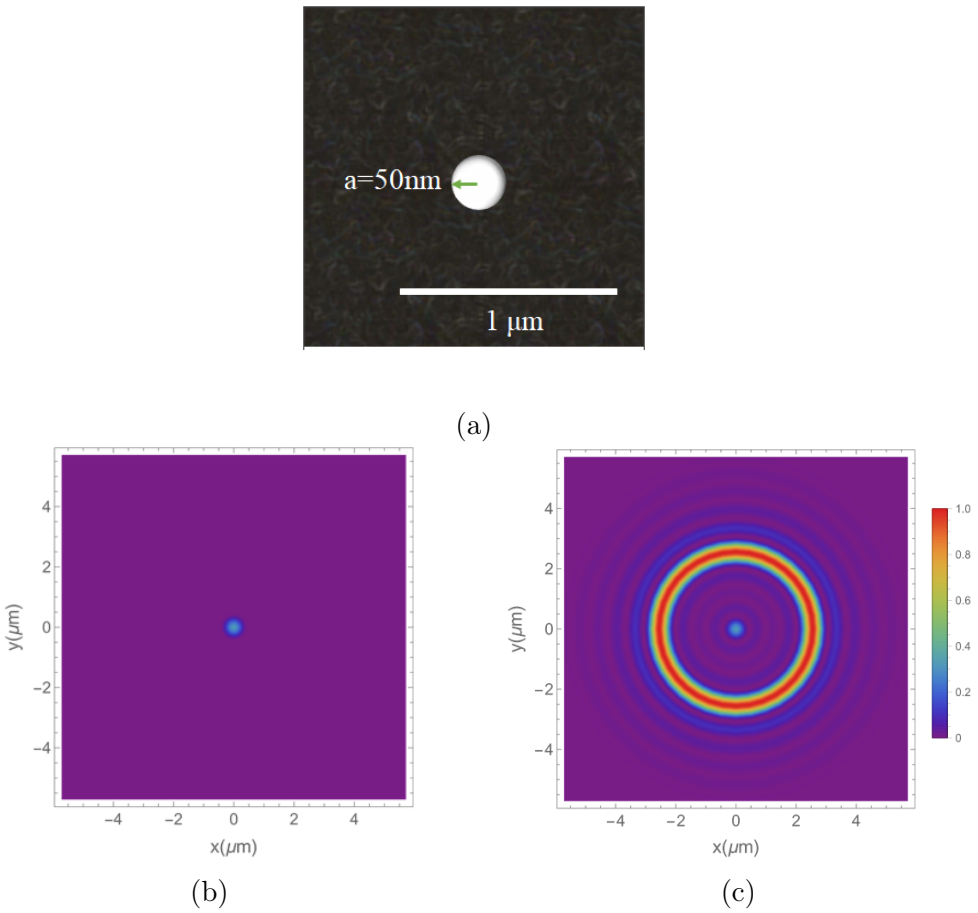

Figure 3.5: Images of Rayleigh scatterers under different illumination conditions: (a) ground truth of a single scatterer ($a = 50\,\text{nm}$=0.1λ and $n = 1.5$), (b) $\langle \boldsymbol{S} \rangle_x$ of the scatterer illuminated by a VSF, and (c) $\langle \boldsymbol{S} \rangle_x$ as illuminated by a superoscillatory field polarized in y direction; with superoscillatory spot radius, $\text{r}_{\text{sp}} = 0.94\lambda$.

3.5.3 Super-resolved images of Rayleigh scatterer patterns

A robust imaging system should be able to image multiple particles and be sensitive to both size and index variations. Therefore, images of various scatterer arrangements are tested.

Figure 3.6 shows that two scatterers are better resolved when illuminated by a VSF than when illuminated by a diffraction-limited spot. The separation between the two scatterers is $d_0 = 610\,\text{nm}$=1.22λ. The VSF is tailored to have a central lobe radius of $r_s = 470\,\text{nm}$=0.94λ, while the radius of the diffraction-limited spot

is $r_d = 732\,\text{nm}$=1.46λ. The two particles are resolved by the VSF illumination but not the diffraction-limited spot.

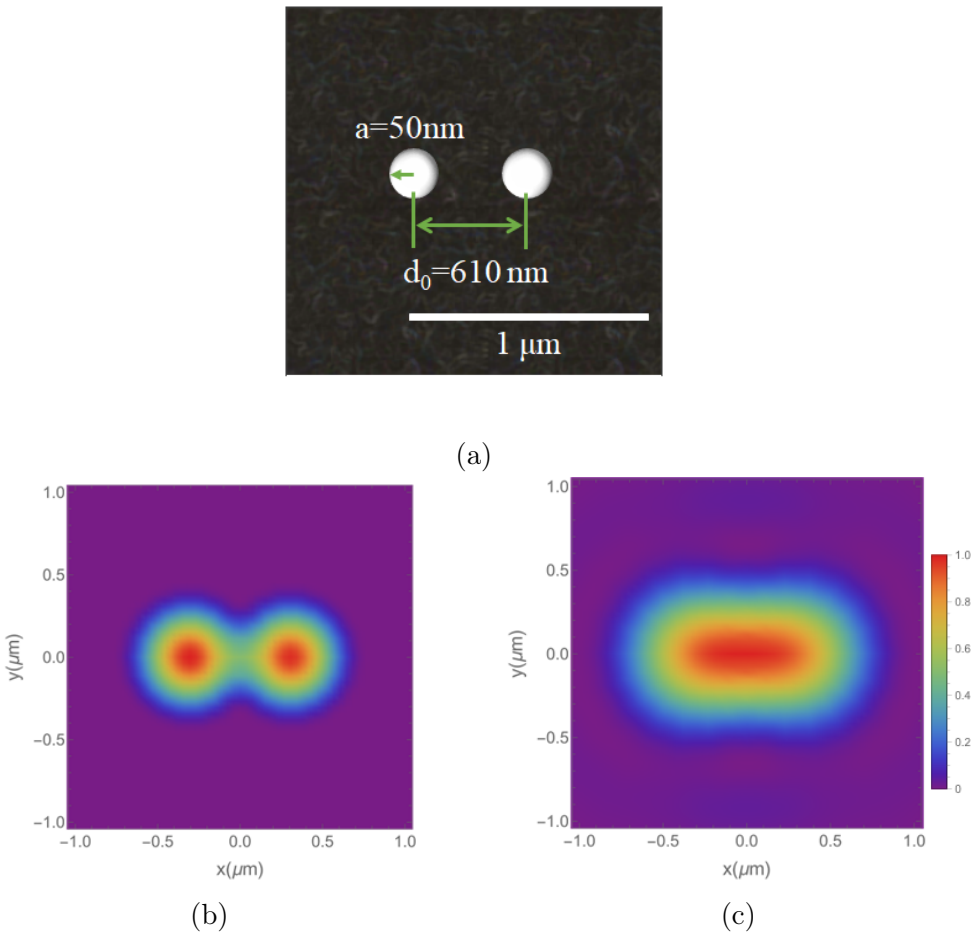

Figure 3.6: Images of Rayleigh scatterers under different illumination conditions: (a) ground truth of two scatterers separated by $d_0 = 610\,\text{nm}$, (b) $\langle \boldsymbol{S} \rangle_x$ of the two scatterers illuminated by a VSF with $r_s = 470\,\text{nm}$=0.94λ, and (c) $\langle \boldsymbol{S} \rangle_x$ when illuminated by the diffraction-limited spot with $r_d = 732\,\text{nm}$=1.46λ.

Figure 3.7 shows the simulated response for a five-scatterer system with a "Λ" shape, with $a = 50\,\text{nm}$, $n = 1.5$, and $d_0 = 610\,\text{nm}$=1.22λ. In Figure3.7 (b), the system is imaged with a VSF, and in Figure3.7 (c), the image produced by a diffraction-limited spot is shown for comparison. It is evident that the particles are better resolved by the VSF illumination.

Figure 3.8 compares the images of a nanoparticle system under different illumi-

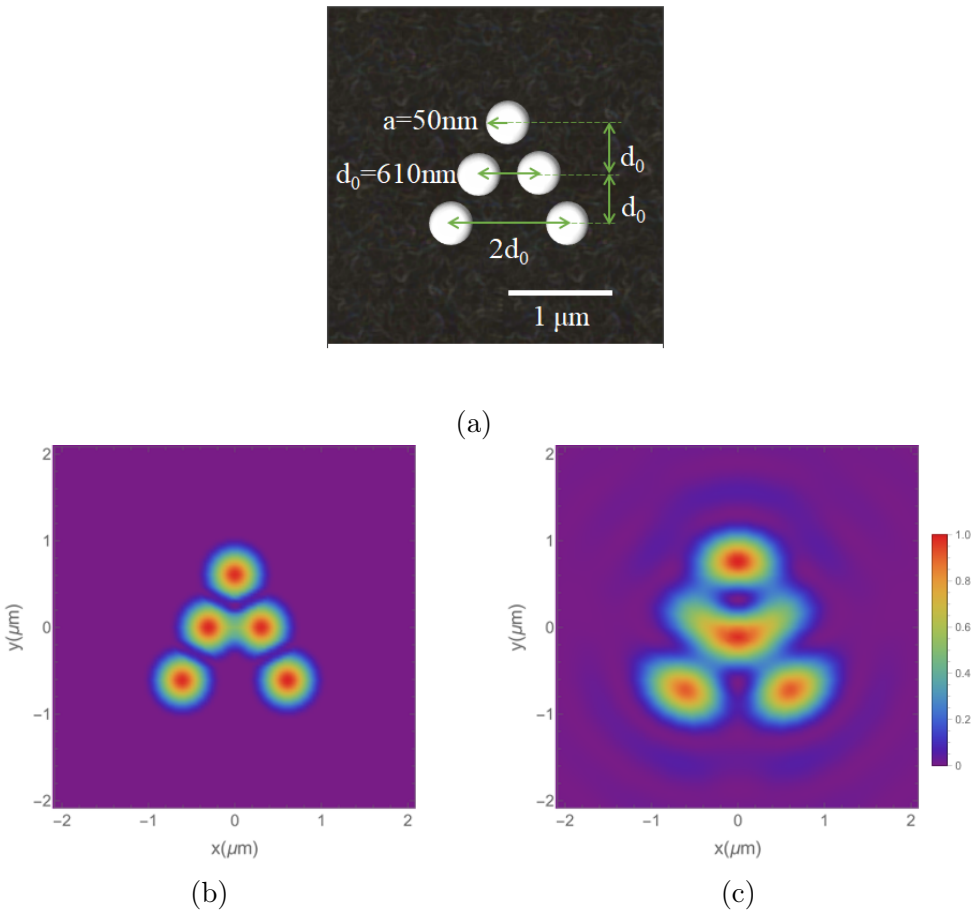

Figure 3.7: Images of Rayleigh scatterers under different illumination: (a) ground truth of five scatterers with a "Λ" shape ($a = 50\,\text{nm}$=0.1λ, $n = 1.5$, and $d_0 = 610\,\text{nm}$=1.22λ) (b) $\langle \boldsymbol{S} \rangle_x$ of the scatterers illuminated by a VSF, and (c) $\langle \boldsymbol{S} \rangle_x$ of the scatterers illuminated by a diffraction-limited spot.

nation conditions: Figure 3.8(a) shows the ground truth of the system, with n=1.5, Figure 3.8 (b) shows the image illuminated by a VSF, and Figure 3.8 (c) shows the image illuminated by a diffraction-limited spot. The image under the VSF shows more clear boundaries of the nanoparticles.

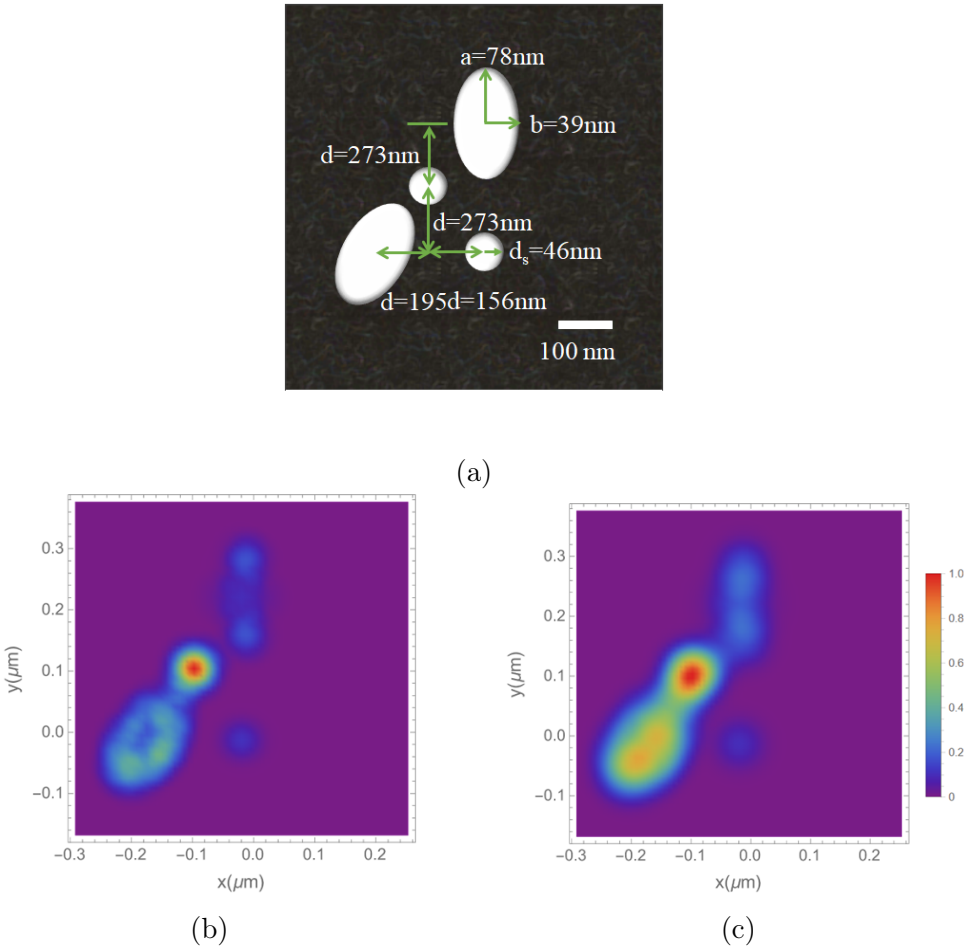

Figure 3.8: Images of Rayleigh scatterers under different illumination: (a) ground truth of nanoparticles with different shapes,with n=1.5, (b) $\langle \boldsymbol{S} \rangle_x$ of the scatterers illuminated by a VSF, and (c) $\langle \boldsymbol{S} \rangle_x$ as illuminated by a diffraction-limited spot.

3.5.4 Factors affecting super-resolved image quality

There are several factors might affect the quality of the super-resolved images. Figure 3.9 (a) shows, the five scatterers, with each numbered, are taken to have an index ratio of $n_1 : n_2 : n_3 : n_4 : n_5 = 1 : 2 : 3 : 4 : 1$; acceptable resolution and index discrimination is demonstrated. In Figure 3.9 (b), the scatterer size has been increased to $a = 200\,\text{nm}$=0.4λ, and significant distortions of the scattered field can be seen; this shows that multiple scattering effects become significant beyond a certain scattering strength.

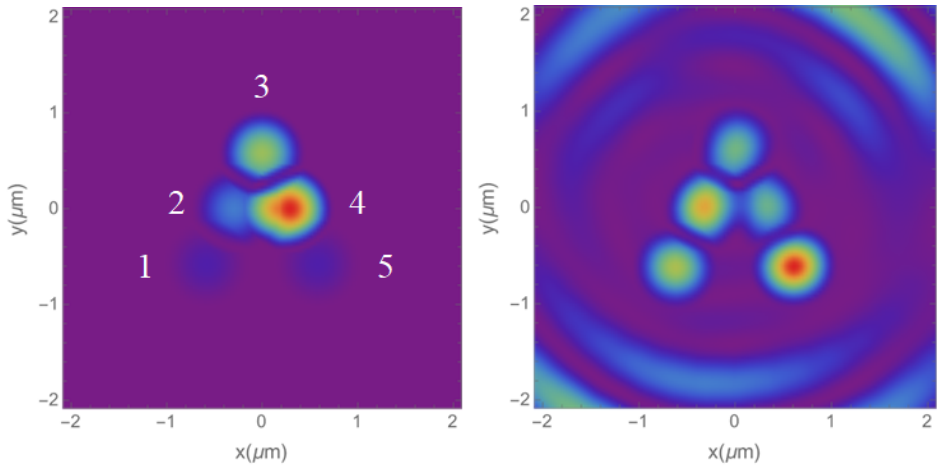

(a) (b)

Figure 3.9: Images of Rayleigh scatterers under different illumination: (a) $\langle \boldsymbol{S} \rangle_x$ as illuminated by the VSF for five scatterers with a refractive index ratio of $n_1 : n_2 : n_3 : n_4 : n_5 = 1 : 2 : 3 : 4 : 1$ and (b) $\langle \boldsymbol{S} \rangle_x$ as illuminated by the VSF for five scatterers with a size of $a = 200\,\text{nm} = 0.4\lambda$.

Scatterers aligned along the polarization direction could potentially have their images distorted by multiple scattering effects. Figure 3.10 shows the image of a five-scatterer system with a cross shape illuminated by the VSF. The scatterers' size and refractive index are the same as those of the Λ system. The scatterers that are vertically aligned along field polarization direction are linked by multiple scattering artifacts. The effect is relatively small, however, and the objects remain well-resolved. Overall, the minimum resolution of the system is subject to the detector's sensitivity. As the central spot becomes narrower, its amplitude decreases as well. System noise could be included in the simulations in future studies.

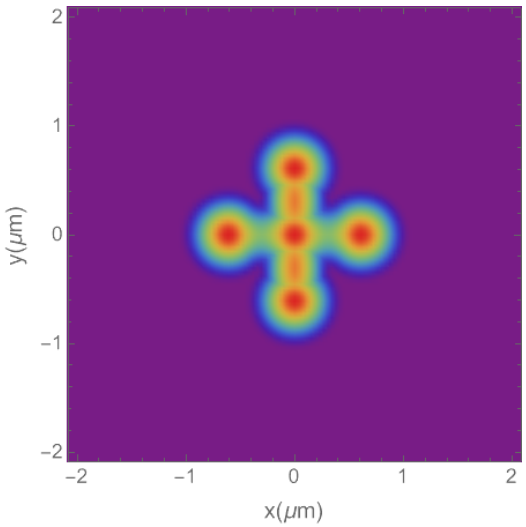

Figure 3.10: Multi-scattering due to scatterers pattern: $\langle \boldsymbol{S} \rangle_x$ of five scatterers with a cross shape illuminated by a VSF; scatterers' size and refractive index are the same as those of the Λ system.

It is natural to ask if the sidelobe suppression is due to the polarization engineering or some other effect. As the selection of scattering signals from the y-polarized central lobe or the x-polarized sidelobes is achieved by placing the detector facing x direction, the image is also simulated by placing the detector with another orientation. In Figure 3.11, the detector for detecting the five-scatterers system (with a "Λ" shape) faces the y direction, and it can be seen that the image is overwhelmed by the scattered light from the sidelobes.

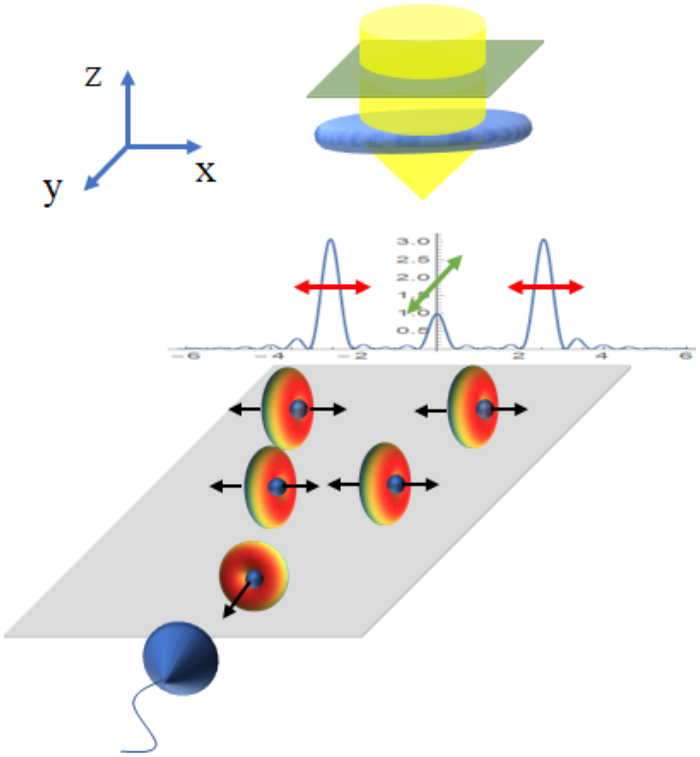

(a)

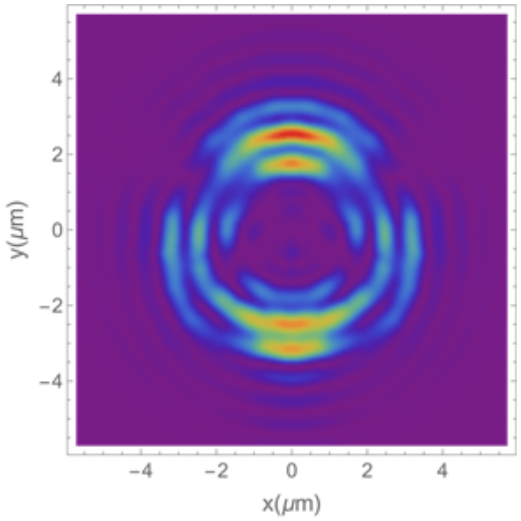

(b)

Figure 3.11: Imaging system and an obtained image with a detector facing y direction: (a) experimental setup and (b) $\langle \boldsymbol{S} \rangle_x$ of five scatterers illuminated by a VSF.

3.6 Creation of Vector Superoscillatory Field

In this section, to construct the desired vector superoscillatory field, the vector field in the aperture plane is calculated from the desired vector superoscillatory field in the

image plane. The polarization distribution in the aperture plane is then illustrated; a polarization element is proposed for generating such a polarization distribution.

3.6.1 Vector superoscillatory field in image plane

The calculation of a scalar superoscillatory field has been demonstrated in Chapter 2. The vector superoscillatory field in the image plane is created by filtering the scalar superoscillatory field by two window functions: one window function transmits the central lobe of $U_{\mathrm{I}}(\boldsymbol{r}_{\mathrm{I}})$ as $\boldsymbol{E}'_y(\boldsymbol{r}_{\mathrm{I}})$ and the other window function transmits sidelobes of $U_{\mathrm{I}}(r_{\mathrm{I}})$ as $\boldsymbol{E}'_x(\boldsymbol{r}_{\mathrm{I}})$. The window functions are:

$$t_{E_x}(\boldsymbol{r}_{\mathrm{I}}) = \begin{cases} 0 & r_{\mathrm{I}} \leq 0.47\,\mu\mathrm{m} \\ 1 & r_{\mathrm{I}} > 0.47\,\mu\mathrm{m} \end{cases} \tag{3.28}$$

and

$$t_{E_y}(\boldsymbol{r}_{\mathrm{I}}) = \begin{cases} 1 & r_{\mathrm{I}} \leq 0.47\,\mu\mathrm{m} \\ 0 & r_{\mathrm{I}} > 0.47\,\mu\mathrm{m} \end{cases} \tag{3.29}$$

Then, $\boldsymbol{E}'_x(\boldsymbol{r}_{\mathrm{I}})$ and $\boldsymbol{E}'_y(\boldsymbol{r}_{\mathrm{I}})$ are:

$$\boldsymbol{E}'_x(\boldsymbol{r}_{\mathrm{I}}) = U_{\mathrm{I}}(\boldsymbol{r}_{\mathrm{I}}) t_{E_x}(\boldsymbol{r}_{\mathrm{I}}), \tag{3.30}$$

and

$$\boldsymbol{E}'_y(\boldsymbol{r}_{\mathrm{I}}) = U_{\mathrm{I}}(r_{\mathrm{I}}) t_{E_y}(\boldsymbol{r}_{\mathrm{I}}), \tag{3.31}$$

where $U_{\mathrm{I}}(r_{\mathrm{I}})$ is the scalar superoscillatory field. Figure 3.12 shows the amplitude and the phase of $\boldsymbol{E}'_x(\boldsymbol{r}_{\mathrm{I}})$ and $\boldsymbol{E}'_y(\boldsymbol{r}_{\mathrm{I}})$.

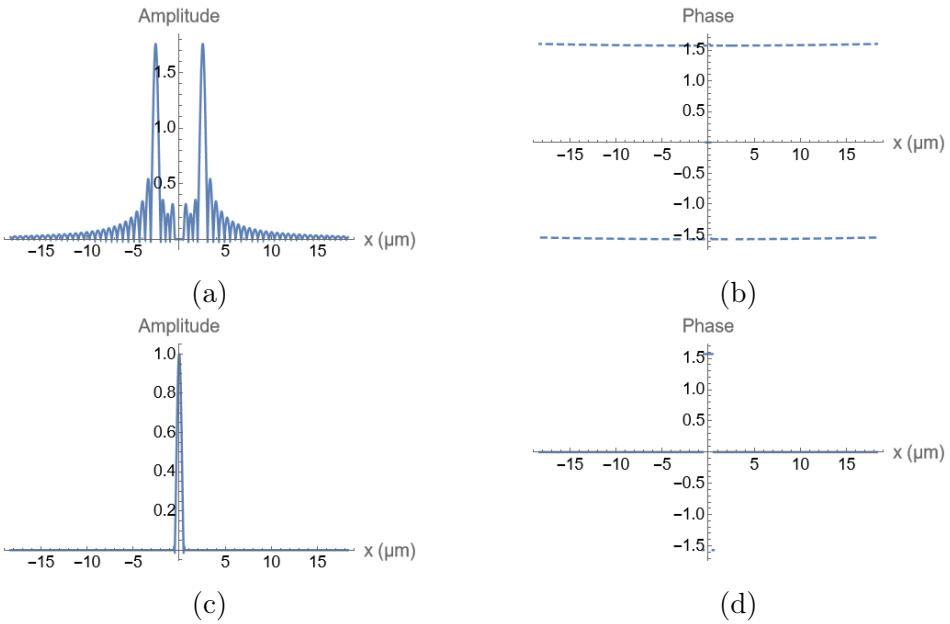

Figure 3.12: Vector superoscillatory field in the image plane: (a) amplitude of $\boldsymbol{E}'_x(\boldsymbol{r}_{\mathrm{I}})$, (b) phase of $\boldsymbol{E}'_x(\boldsymbol{r}_{\mathrm{I}})$, (c) amplitude of $\boldsymbol{E}'_y(\boldsymbol{r}_{\mathrm{I}})$, and (d) phase of $\boldsymbol{E}'_y(\boldsymbol{r}_{\mathrm{I}})$.

3.6.2 Vector field in aperture plane

The vector field, $\boldsymbol{E}_x(\boldsymbol{r}_{\mathrm{L}})$ and $\boldsymbol{E}_y(\boldsymbol{r}_{\mathrm{L}})$, which produces this vector superoscillatory field can be determined by inverting the Fourier relationship. In the calculation, the vector field is obtained by using Fourier Bessel transform over the interpolation functions of $\boldsymbol{E}'_x(\boldsymbol{r}_{\mathrm{L}})$ and $\boldsymbol{E}'_y(\boldsymbol{r}_{\mathrm{L}})$ in the image plane:

$$\boldsymbol{E}_x(\boldsymbol{r}_{\mathrm{L}i}) = \left(\frac{iU_{\mathrm{o}}e^{ikd_{\mathrm{I}}}}{\lambda d_{\mathrm{I}}}e^{\frac{ik}{2d_{\mathrm{I}}}|\boldsymbol{r}_{\mathrm{I}i}|^2}\right)^{-1}\int_{r_{\mathrm{I}}}\boldsymbol{E}'_x(\boldsymbol{r}_{\mathrm{I}})J_0\left(\frac{-2\pi k r_{\mathrm{L}i}r_{\mathrm{I}}}{d_{\mathrm{I}}}\right)dr_{\mathrm{I}}, \tag{3.32}$$

and

$$\boldsymbol{E}_y(\boldsymbol{r}_{\mathrm{L}i}) = \left(\frac{iU_{\mathrm{o}}e^{ikd_{\mathrm{I}}}}{\lambda d_{\mathrm{I}}}e^{\frac{ik}{2d_{\mathrm{I}}}|\boldsymbol{r}_{\mathrm{I}i}|^2}\right)^{-1}\int_{r_{\mathrm{I}}}\boldsymbol{E}'_y(\boldsymbol{r}_{\mathrm{I}})J_0\left(\frac{-2\pi k r_{\mathrm{L}i}r_{\mathrm{I}}}{d_{\mathrm{I}}}\right)dr_{\mathrm{I}}. \tag{3.33}$$

Figure 3.13 shows the amplitude and the phase of $\boldsymbol{E}_x(\boldsymbol{r}_{\mathrm{L}})$ and $\boldsymbol{E}_y(\boldsymbol{r}_{\mathrm{L}})$ in the aperture plane. The amplitude of $\boldsymbol{E}_y(\boldsymbol{r}_{\mathrm{L}})$ is significantly smaller than that of $\boldsymbol{E}_x(\boldsymbol{r}_{\mathrm{L}})$. When the maximum amplitude of $\boldsymbol{E}_x(\boldsymbol{r}_{\mathrm{L}})$ is normalized to 1, that of $\boldsymbol{E}_y(\boldsymbol{r}_{\mathrm{L}})$ is around

0.02. The phase of $\boldsymbol{E}_x(\boldsymbol{r}_\mathrm{L})$ contains two annuli of phase shift of value π. The phase of $\boldsymbol{E}_y(\boldsymbol{r}_\mathrm{L})$ is near 0, with a shallow gradual change, across the aperture. Overall, $\boldsymbol{E}_x(\boldsymbol{r}_\mathrm{L})$ dominates the vector field in the aperture plane, however, there is a minimal amount of $\boldsymbol{E}_y(\boldsymbol{r}_\mathrm{L})$.

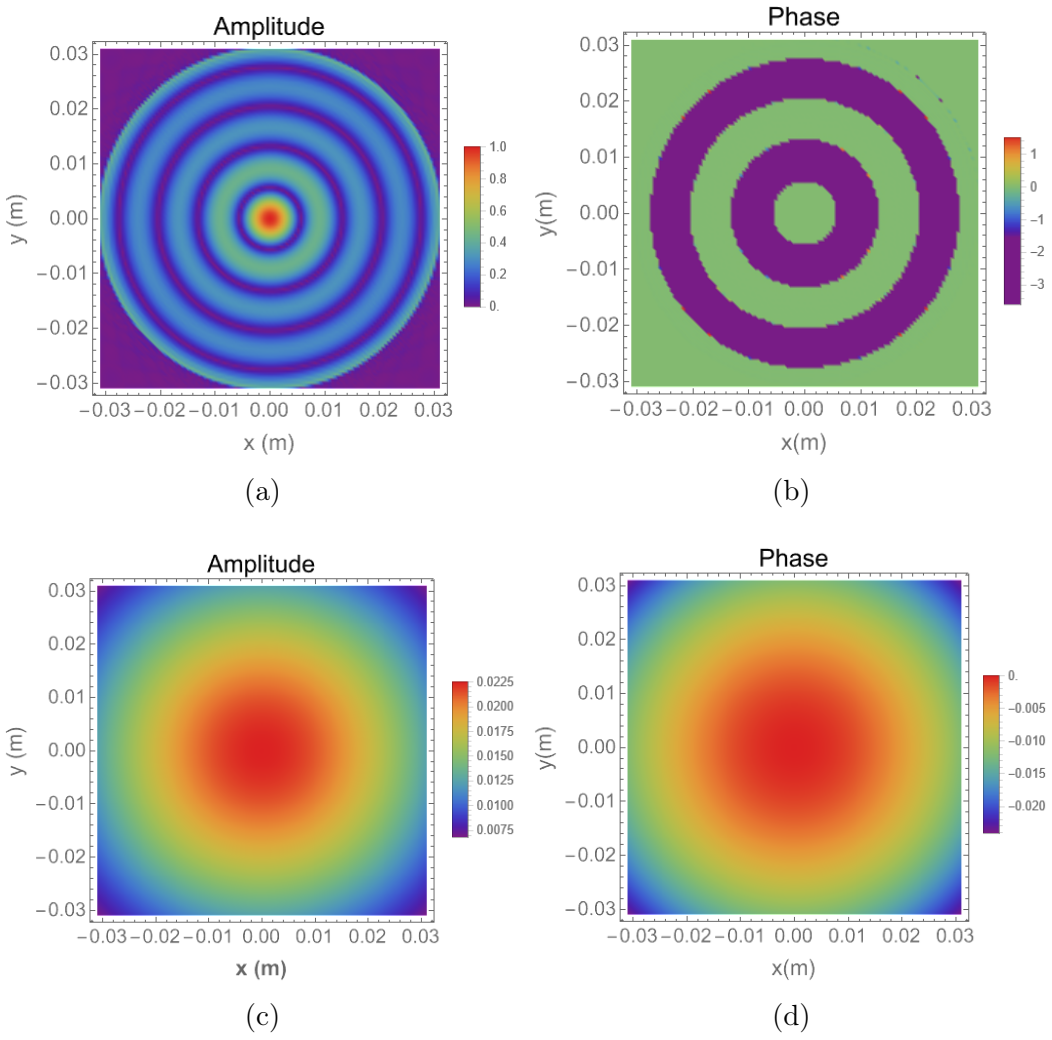

Figure 3.13: Vector field in the aperture plane: (a) amplitude of $\boldsymbol{E}_x(\boldsymbol{r}_\mathrm{L})$, (b) phase of $\boldsymbol{E}_x(\boldsymbol{r}_\mathrm{L})$, (c) amplitude of $\boldsymbol{E}_y(\boldsymbol{r}_\mathrm{L})$, and (d) phase of $\boldsymbol{E}_y(\boldsymbol{r}_\mathrm{L})$.

3.6.3 Calculation of polarization distribution in aperture

To achieve the VSF in the image plane, a polarization-sensitive superoscillatory filter is introduced to the aperture plane. First, Stokes parameters are calculated from the vector electric field, $\boldsymbol{E}_x(\boldsymbol{r}_\mathrm{L})$ and $\boldsymbol{E}_y(\boldsymbol{r}_\mathrm{L})$, in the aperture plane. Second,

a polarization state distribution is calculated across the aperture. The ellipticity of polarization ellipses is given by:

$$\chi = \frac{1}{2} \arcsin \frac{s_3}{s_1}, \tag{3.34}$$

and the orientation angle of polarization ellipses is given by:

$$\psi = -\frac{1}{2} \arg s_1 + i s_2. \tag{3.35}$$

In Figure 3.14, the ellipticity plot shows that the polarization states are linear. Figure 3.15 (a) and (b) plot the orientation angle distribution in the range of $[-\pi/2, \pi/2]$ and $[0, 2\pi]$, respectively. The orientation angle distribution consists of annuli with a value near 0, which represent horizontal polarization. The sharp transition regions between the annuli consist of non-horizontal polarization components.

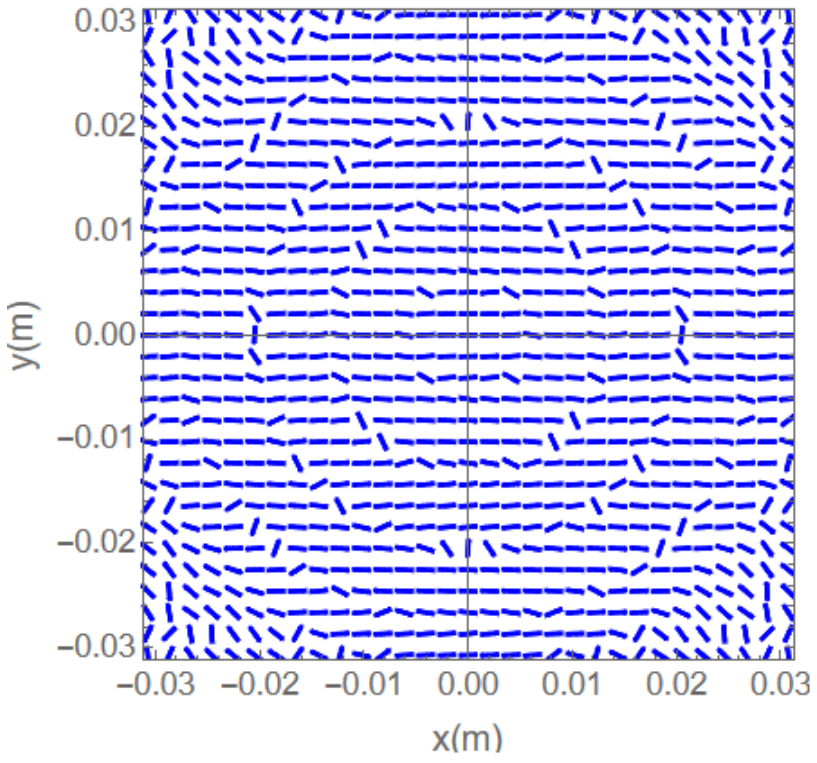

Figure 3.14: Polarization states in the aperture plane.

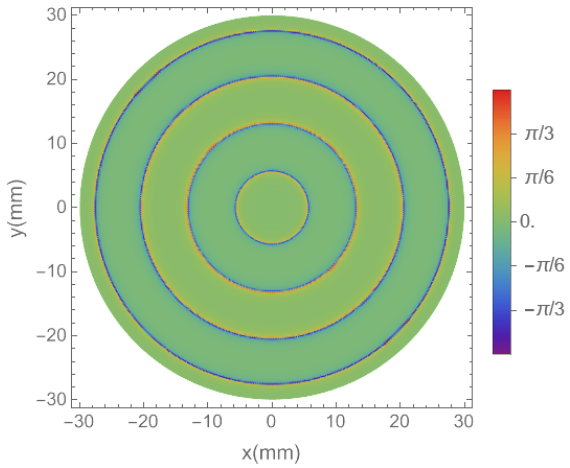

(a)

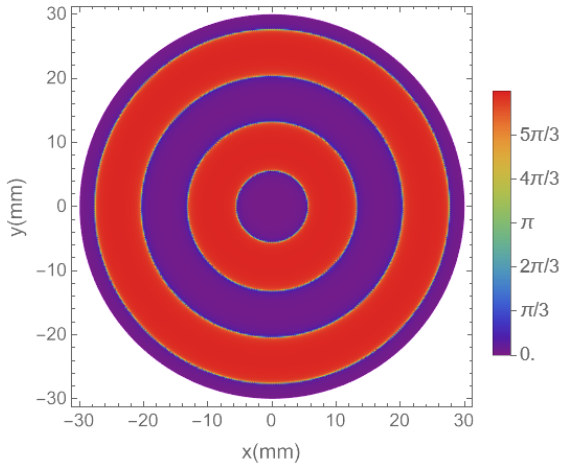

(b)

Figure 3.15: Orientation angle in the aperture plane in the range of (a) [-π/2,π/2] and (b) [0,2π].

3.6.4 Device for generating vector superoscillatory field

A good variety of methods for creating such a polarization-sensitive filter in the aperture plane have already been standardized, such as spatial light modulators, custom diffractive optical elements, and geometric phase-based q-plates [70].

In this study, a liquid crystal device is proposed as following steps. For the first step, Jones vector in the aperture plane is expressed as:

$$\begin{bmatrix} \boldsymbol{E}_x \\ \boldsymbol{E}_y \end{bmatrix} = \begin{bmatrix} E_x e^{-i\phi_x} \\ E_y e^{-i\phi_y} \end{bmatrix} = e^{-i\phi_y} \begin{bmatrix} E_x e^{-i\delta} \\ E_y \end{bmatrix}, \tag{3.36}$$

where $\delta = \phi_x - \phi_y$ is the phase difference of $\boldsymbol{E}_x$ and $\boldsymbol{E}_y$. In this study, $\delta \approx 0||\pi$. The amplitude of the resultant field of $\boldsymbol{E}_x$ and $\boldsymbol{E}_y$ is given by

$$U_L = \sqrt{E_x^2 + E_y^2}. \tag{3.37}$$

By setting the input polarization state as horizontal polarization in x direction, and the amplitude as U_L, the vector field before entering is given by

$$\begin{bmatrix} \boldsymbol{E}_{ox} \\ \boldsymbol{E}_{oy} \end{bmatrix} = \begin{bmatrix} U_L \\ 0 \end{bmatrix}, \tag{3.38}$$

where U_L is generated by a scalar superoscillatory lens calculated in Chapter 2. As shown in Figure 3.13, the electric field in x direction has a π phase shift in two annuli, which is different from the case of scalar field U_L. This difference can be compensated by add another 90 degree rotation angle in the annulus regions in the liquid crystal device, which will be described below.

For the second step, liquid crystal cells are applied as polarization rotators to twist the incident field from horizontal polarization to the target polarization states across the aperture plane. The output polarization is aligned with the scratch direction of the output surface of each liquid crystal cell. The angle of twist is given by

$$\theta = \alpha d, \tag{3.39}$$

where α is a coefficient of the liquid crystal material, d is the thickness of the liquid

crystal cell. The phase retardation coefficient of the liquid crystal cell is given by

$$\beta = (n_e - n_o)k, \tag{3.40}$$

where n_e and n_o are the extraordinary and the ordinary refractive indices, respectively, and k is the wavenumber. Usually, $\beta >> \alpha$. It has been shown that when the input field is polarized in x direction, the field will keep linear polarization but obtain an angle of rotation of θ after passing through a liquid crystal cell, as shown in figure below. The blue cell array provides the rotation of polarization states. The green cell array is to compensate the differences of the phase shift due to the thickness variations among different liquid crystal cells.

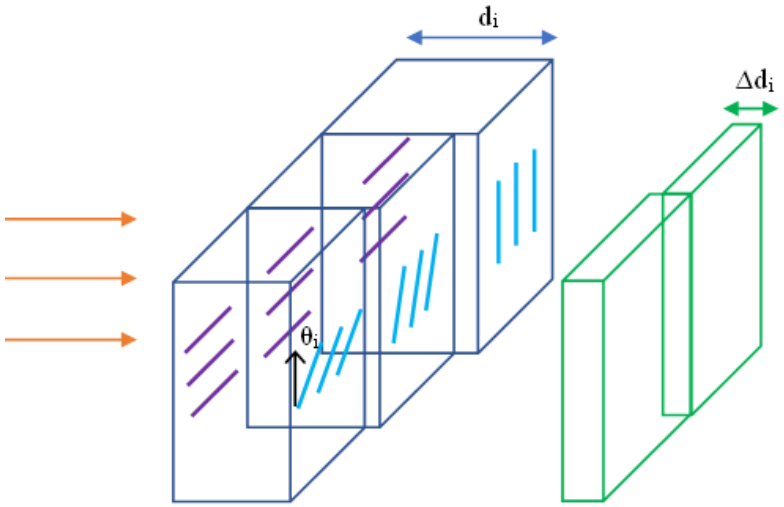

Figure 3.16: Rotation of polarization states by liquid crystal cells.

Appendix C lists the calculation of the vector field after being transmitted by liquid crystal cells.

3.7 Discussion and Conclusion

In this chapter, the transverse wave nature of light and the polarization-dependent scattering of Rayleigh scatterers are utilized to produce sidelobe-free super-resolved images. A liquid crystal device is proposed for creating the vector-superoscillatory

field illumination. Other researchers have started investigating the use of vector fields to improve superoscillatory imaging. Recently, Pant, Meena and Singh [71] filtered the transverse electric field from a tightly focused beam, suppressing sidelobes and leaving a longitudinal superoscillatory spot. These results highlight that direct consideration of the vector properties of light can provide significant benefits to superoscillatory imaging.

CHAPTER 4: CIRCULARLY COHERENT VORTEX BEAMS

4.1 Introduction

Circularly coherent sources, which are perfectly coherent on any ring that is concentric to the beam center, can preserve the spiral phase structures of optical vortices on propagation, making them potentially useful for free-space applications such as communications and remote sensing. In Chapter 4, section 4.2 describes basic quantities applied in partial coherence theory, coherent optical vortices, and singularities in partially coherent fields. Section 4.3 theoretically studies circularly coherent vortex beams by imposing circular coherence on Laguerre-Gaussian (LG) beams. In section 4.4, the second-order coherence properties and coherence singularities of these circularly coherent vortex beams are investigated in free-space propagation up to 3 km. Section 4.5 discusses the noteworthy self-focusing feature of such beams that arises due to the circular coherence. Section 4.6 shows an experimental setup for measuring circularly coherent vortex beams.

4.2 Partial Coherence and Optical Vortices

4.2.1 Second-order coherence properties

The cross-spectral density (CSD) is defined as the two-point correlation function of an ensemble of space-frequency realizations for any pair of points in the field given by

$$W(\boldsymbol{r}_1, \boldsymbol{r}_2; \omega) = \langle U^*(\boldsymbol{r}_1; \omega) U(\boldsymbol{r}_2; \omega) \rangle, \tag{4.1}$$

where $U(\boldsymbol{r}_i; \omega)$, with $i = 1, 2$ represents a member of a statistical ensemble of monochromatic realizations of the field and the angular brackets denote an average over the

ensemble [54].

When the two points $\boldsymbol{r}_1$ and $\boldsymbol{r}_2$ coincide, the CSD reduces to the spectral density, which is the component of the irradiance at frequency ω, i.e.

$$S(\boldsymbol{r};\omega) = W(\boldsymbol{r},\boldsymbol{r};\omega) = \langle |U(\boldsymbol{r};\omega)|^2 \rangle. \tag{4.2}$$

The spectral degree of coherence, which characterizes the strength of correlations and visibility of interference fringes produced by the field at points $\boldsymbol{r}_1$ and $\boldsymbol{r}_2$, is defined as [72]

$$\mu(\boldsymbol{r}_1,\boldsymbol{r}_2;\omega) = \frac{W(\boldsymbol{r}_1,\boldsymbol{r}_2;\omega)}{\sqrt{S(\boldsymbol{r}_1;\omega), S(\boldsymbol{r}_2;\omega)}}. \tag{4.3}$$

The spectral degree of coherence is constrained to the bounds $0 \leq |\mu| \leq 1$, with 0 representing incoherence and 1 representing complete coherence.

For quasi-monochromatic fields of center frequency ω, the observable properties of the field are well-approximated by the CSD at this single frequency. In this chapter, the optical fields are considered as quasi-monochromatic and therefore the dependence in ω is dropped for brevity going forward.

From Eq. (4.1), it follows that the CSD must be Hermitian with respect to $\boldsymbol{r}_1$ and $\boldsymbol{r}_2$ and furthermore must satisfy the non-negative definiteness condition,

$$\iint \psi^*(\boldsymbol{r}_1) W(\boldsymbol{r}_1,\boldsymbol{r}_2) \psi(\boldsymbol{r}_2)\, d^2r_1\, d^2r_2 \geq 0, \tag{4.4}$$

where $\psi(\boldsymbol{r}_i)$ is an arbitrary function that is square-integrable. In general, it is difficult to demonstrate that any particular function of $\boldsymbol{r}_1$ and $\boldsymbol{r}_2$ is non-negative definite. In 2007, however, Gori and Santarsiero showed [73] that any valid CSD can be written in the mathematical form,

$$W(\boldsymbol{r}_1,\mathbf{r}_2) = \int H^*(\boldsymbol{r}_1,\boldsymbol{v}) P_N(\boldsymbol{v}) H(\boldsymbol{r}_2,\boldsymbol{v}) d^N v. \tag{4.5}$$

This expression represents the CSD as an average over an ensemble of fields $H(\boldsymbol{r}_i, \boldsymbol{v})$, where $\boldsymbol{v}$ is in general an N-dimensional dummy vector that characterizes a particular state of the field and $P_N(\boldsymbol{v})$ is a non-negative probability density that represents the probability that the field is in state $\boldsymbol{v}$.

One of the insightful ideas arising from Eq. (4.5) is that new coherence phenomena can be generated by making unusual choices for the field ensemble and probability density. For example, it is possible to add a partially coherent twist to a general CSD for both circularly symmetric and non-symmetric beams [74], and it is possible to make fields that are coherent in the radial direction and partially coherent in the azimuthal direction [75]. Here, the interest is in circularly coherent beams, which possess a spectral degree of coherence that only depends on the difference between the squared radial coordinates of two points; here the shape of the degree of coherence may be written as [76]

$$\mu(r_1, r_2) = \operatorname{sinc}\left(\frac{r_2^2 - r_1^2}{\delta_\mu^2}\right), \tag{4.6}$$

where δ_μ may be interpreted as the correlation length of the field and $\operatorname{sinc} = \sin x/x$. Any pair of points located within a ring concentric with the center beam axis are perfectly coherent.

4.2.2 Coherent optical vortex

The goal is to impose this circular coherence upon a vortex beam. The most familiar class of vortex beams are the LG beams, which are characterized by a radial order n and an azimuthal order m. We consider vortex beams with $n = 0$, which possess a field $\psi_m(\boldsymbol{r})$ in the source plane,

$$\psi_m(\boldsymbol{r}) = \left(\frac{\sqrt{2}r}{\sigma_s}\right)^{|m|} e^{-r^2/\sigma_s^2} e^{im\phi}, \tag{4.7}$$

where σ_s is the waist size, m is the azimuthal (vortex) order, ϕ is the azimuthal angle, and r is the modulus of the position vector $\boldsymbol{r}$. The phase $\exp(im\phi)$ represents the vortex phase twist of the beam. Figure 4.1 shows transverse profiles of LG beams with a beam waist of σ_s =0.02 m, azimuthal orders of $m = 1$ and $m = 3$.

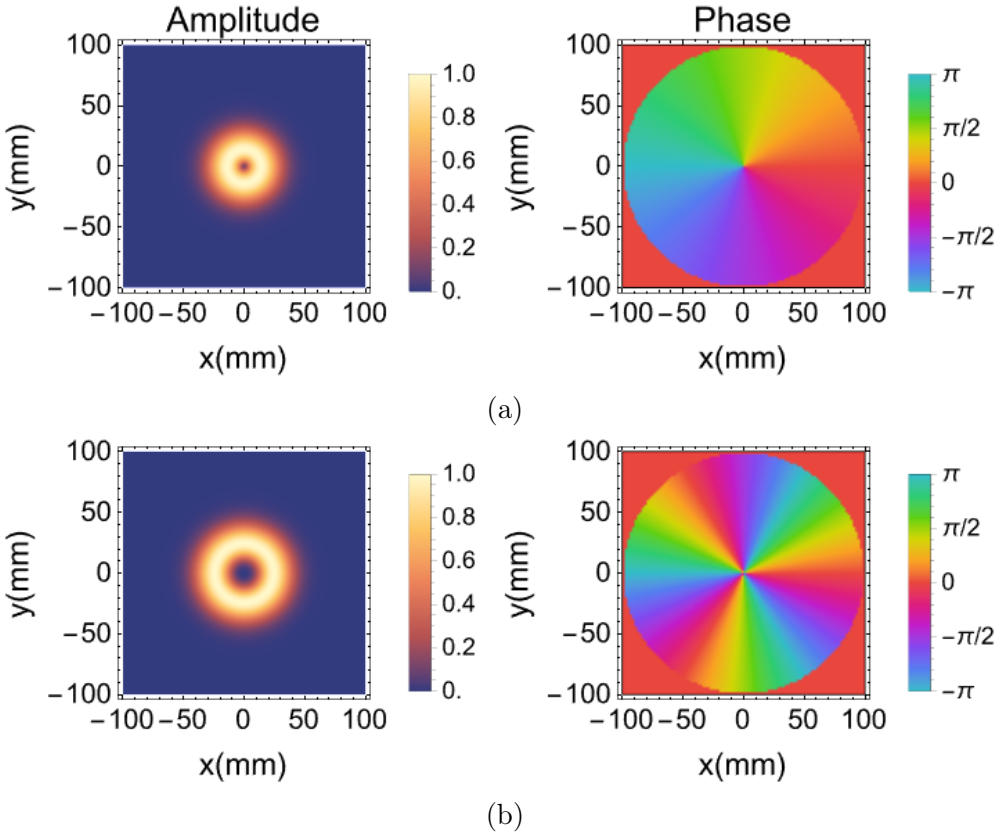

Figure 4.1: Amplitude and phase profiles of LG beams with an azimuthal order of (a) $m = 1$ and (b) $m = 3$, with $\sigma_s = 0.02$ m.

4.2.3 Optical vortices in partially coherent fields

It has been assumed that there are intrinsic conflicts between optical vortices and partial coherence. In partially coherent fields, optical vortices usually evolve into singularities of a correlation function with one fixed observation point, named correlation vortices. Then, under some observing points, the vortex structure distorted and are called non-deterministic vortices. In addition, positions of correlation vortices depend on observation points and vortices center can have non-zero intensity which makes

it hard to detect them. Correlation vortices in circularly coherent vortex beams are demonstrated in section 4.3 and section 4.4.

4.3 Circularly Coherent Vortex Beam at Source Plane

4.3.1 Creation of circularly coherent vortex beam

One way to create a circularly coherent beam is to take the ensemble of fields $H(\mathbf{r_i}, \mathbf{v})$ to be of the form,

$$H(\mathbf{r}, v) = \psi(\mathbf{r}) e^{ivr^2/\delta_\mu^2}, \tag{4.8}$$

where $\psi(\mathbf{r})$ is interpreted as the deterministic field of the ensemble, which is taken to be a LG beam. Here, the probability density function $P_N(v)$ is taken to be

$$P_N(v) = \sqcap(v)\,, \tag{4.9}$$

where $\sqcap(v)$ is a rectangular function that is equal to unity for $|v| \leq 1$ and zero otherwise, and v is taken to be a one-dimensional variable. These are the functions employed by Santarsiero et al. [76], and the choice of $H(\mathbf{r}, v)$ indicates that the ensemble consists of an identical set of beams with random focal lengths (or radii of curvatures), as shown in Figure 4.2.

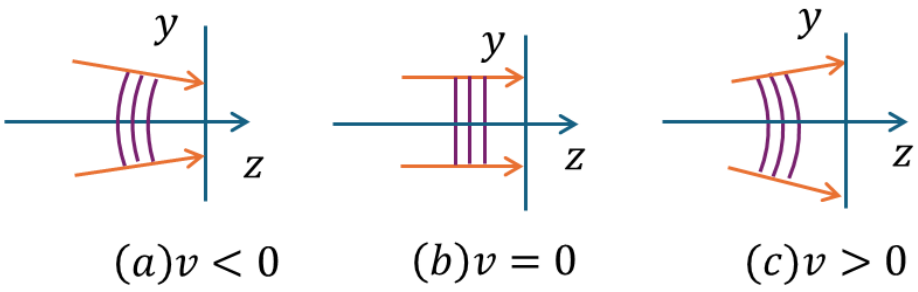

Figure 4.2: Component fields of $H(\mathbf{r}, v)$ with different radii of curvatures: (a) v<0, (b) v=0, and (c) v>0.

By substituting these forms of $H(\mathbf{r}, v)$ and $P_N(v)$ into Eq. (4.5), the CSD in the

source plane of a circularly coherent field is

$$\begin{aligned} W_0(\mathbf{r}_1, \mathbf{r}_2) &= \int \sqcap(v)\, \psi^*(\mathbf{r}_1) e^{-ivr_1^2/\delta_\mu^2} \psi(\mathbf{r}_2) e^{ivr_2^2/\delta_\mu^2} dv \\ &= \psi^*(\mathbf{r}_1)\psi(\mathbf{r}_2)\mathrm{sinc}\left(\frac{r_2^2 - r_1^2}{\delta_\mu^2}\right). \end{aligned} \tag{4.10}$$

In this form, it can be seen that the spectral degree of coherence is determined by the Fourier transform of $P_{\mathrm{N}}(v)$ with respect to v.

If $\psi(\boldsymbol{r}) = \psi_m(\boldsymbol{r})$, the CSD of the resulting circularly coherent LG beam is of the form,

$$\begin{aligned} W_0(\mathbf{r}_1, \mathbf{r}_2) = &\left(\frac{\sqrt{2}r_1}{\sigma_s}\right)^m e^{-r_1^2/2\sigma_s^2} e^{-im\phi_1} \\ &\times \left(\frac{\sqrt{2}r_2}{\sigma_s}\right)^m e^{-r_2^2/2\sigma_s^2} e^{im\phi_2} \mathrm{sinc}\left(\frac{r_2^2 - r_1^2}{\delta_u^2}\right). \end{aligned} \tag{4.11}$$

According to Eq. (4.11), the CSD is characterized by the coherent vortex beam structure and the radial spectral degree of coherence.

4.3.2 Spectral degree of coherence

Figure 4.3a shows the absolute spectral degree of coherence of circularly coherent source with a diagonal symmetric stripe-shaped pattern, expressed in Eq. (4.6). It can be derived that along the diagonal ($r_1 = r_2$) the source is perfectly coherent ($\mu = 1$); this illustrates that the field at points on any ring concentric to the beam axis is perfectly coherent, as shown in Figure 4.3b. In the off-diagonal region, the pattern starts narrowing as r_1 and r_2 increase. Thus, if a pair of concentric rings is free to move, as one of the two rings moves away from the beam center, the radial separation needed between two rings to obtain a relatively high degree of coherence will become smaller.

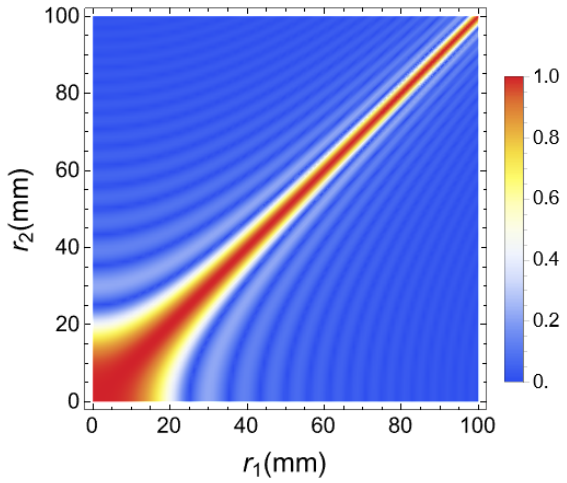

(a)

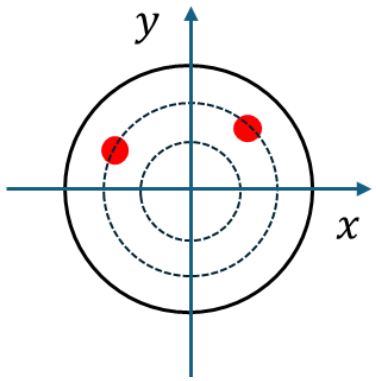

(b)

Figure 4.3: Absolute spectral degree of coherence,$\mu(r_1, r_2)$, of (a) a circularly coherent source, with $\delta_\mu = 0.044\,\mathrm{m}$,(b) with perfect coherence along any ring concentric to the beam axis.

4.3.3 Cross-spectral density

The CSD of circularly coherent vortex beams exhibits a complex correlation structure, including a number of phase singularities. One type of coherence singularity, now known as a correlation vortex, is a vortex of the CSD with one observation point fixed. These are often directly related to the underlying phase singularity of the members of the ensemble, and typically they are singularities of the two-point correlation function and not zeros of intensity like a coherent optical vortex. Another type of coherence singularity, called a ring dislocation, is related to the structure of the spectral degree of coherence; ring dislocations manifest as circles of amplitude

zero of a CSD under a fixed oberving point, and in some cases, as lines of amplitude zero in the amplitude of a CSD.

Figure 4.4 shows the cross-spectral density of circularly coherent LG beams at the source plane, with $\sigma_s = 0.02\,\mathrm{m}$ and $\delta_\mu = 0.044\,\mathrm{m}$. It can be seen that there is a zero of the cross-spectral density for either $r_1 = 0$ or $r_2 = 0$ for $m > 0$, which represents a correlation vortex on the beam axis whose position is independent of the choice of fixed observation point. It can be seen that ring dislocations appear as lines of amplitude zero for higher-order vortex beams. Figure 4.4 also shows that the peak of the CSD shifts away from the origin and the pattern becomes narrower as the azimuthal order increases.

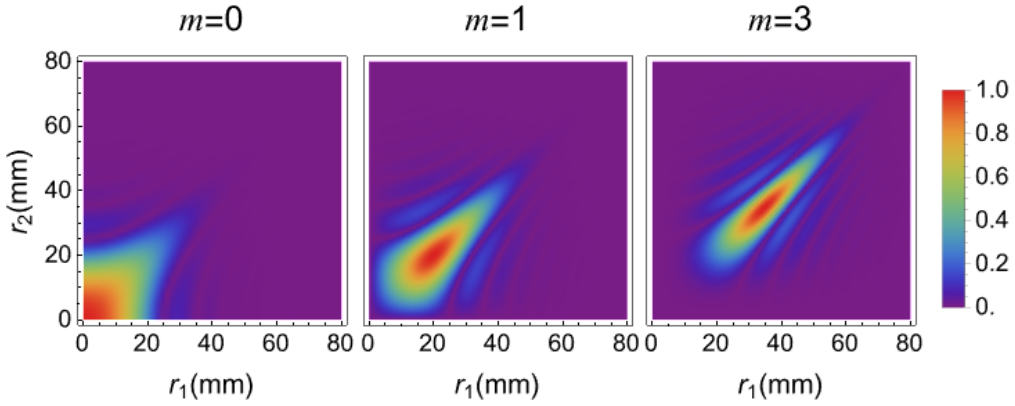

Figure 4.4: CSDs of circularly coherent LG beams at the source plane: CSD as function of r_1 and r_2, with an azimuthal order of $m = 0$, $m = 1$, and $m = 3$, with $\sigma_s = 0.02\,\mathrm{m}$ and $\delta_\mu = 0.044\,\mathrm{m}$.

4.3.4 Amplitude and phase under a fixed observing point

To clearly view the correlation vortices of the beam, we can project the four variable source plane cross-spectral density $W(\mathbf{r}_1, \mathbf{r}_2)$ into a two variable space by fixing one of the two observing points. Fig. 4.5a and 4.5b show amplitude and phase distributions for different azimuthal orders with a fixed observing point r_1 at the source plane, with observing points $r_1 = 0.18\,\mathrm{mm}$, $0.27\,\mathrm{mm}$, and $0.44\,\mathrm{mm}$, respectively. Here, the fixed observation point is shifted outward as the azimuthal order of the LG vortex beams

increases to meet the expansion of the zero intensity region near the beam core and the high intensity ring in the LG vortex beams. Since both the spectral density and the spectral degree of coherence are circularly symmetric, the CSD is also circularly symmetric even with a fixed observation point. In Fig. 4.5a, points and rings with an amplitude of zero represent correlation vortices and ring dislocations, respectively. In Fig. 4.5b, spiral phase structures at beam centers and phase jumps of π manifest correlation vortices and ring dislocations, respectively.

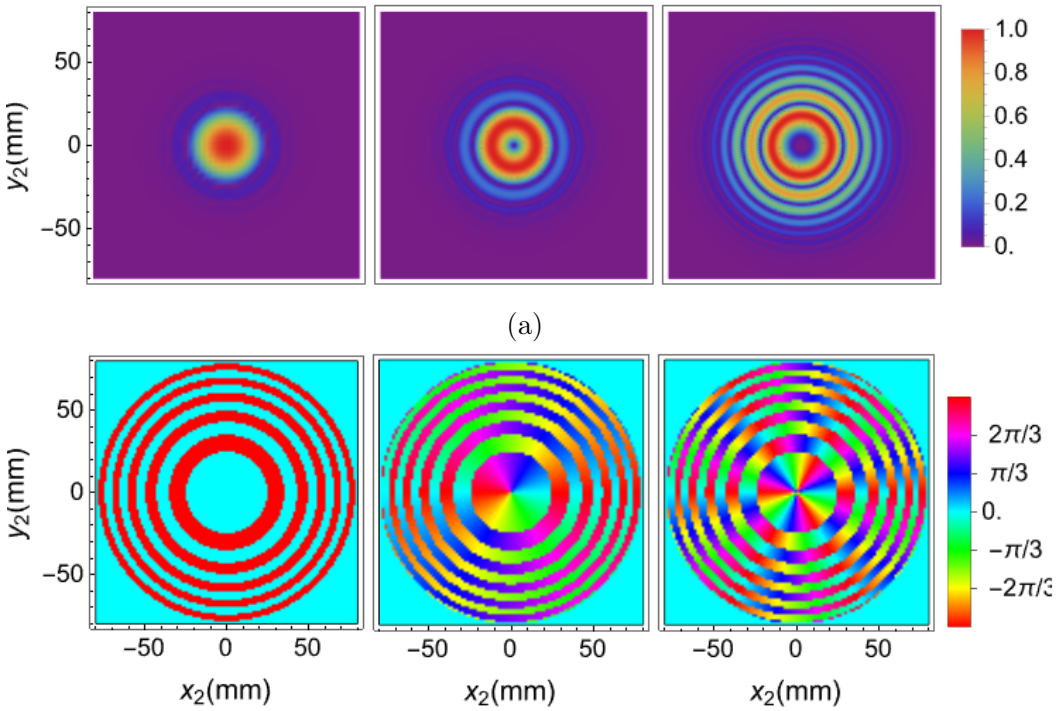

Figure 4.5: Circularly coherent LG beams at the source plane: (a) amplitude , and (c) phase of CSDs under a fixed observing point, r_1, with an azimuthal order of $m=0$, $m=1$, and $m=3$, with $\sigma_s=0.02\,\mathrm{m}$ and $\delta_\mu=0.044\,\mathrm{m}$. Observing points are $r_1=0.18\,\mathrm{mm}$, $0.27\,\mathrm{mm}$, and $0.44\,\mathrm{mm}$, respectively.

4.4 Paraxial Propgation of Circularly Coherent Vortex Beam

4.4.1 Cross-spectral density

According to the Huygens-Fresnel principle [77], the propagation of the cross-spectral density can be determined in the paraxial regime by the expression,

$$W(\mathbf{r}_1, \mathbf{r}_2; z) = \frac{1}{(\lambda z)^2} \iint W_0(\mathbf{r}'_1, \mathbf{r}'_2) e^{-\frac{ik}{2z}(\mathbf{r}_1 - \mathbf{r}'_1)^2} e^{\frac{ik}{2z}(\mathbf{r}_2 - \mathbf{r}'_2)^2} d^2\mathbf{r}'_1 d^2\mathbf{r}'_2, \tag{4.12}$$

where $\mathbf{r}'_i$ is the position vector at the source plane, $\mathbf{r}_i$ is the position vector in the far field, z is the propagation distance, and k is the wavenumber. By substituting Eq. (4.11) into Eq. (4.12) and separating r'_1 and r'_2, this may be written as

$$\begin{aligned} W(\mathbf{r}_1, \mathbf{r}_2; z) = &\frac{1}{(\lambda z)^2} \int \sqcap(v) dv \\ &\int \left(\frac{\sqrt{2} r'_1}{\sigma_s} \right)^m e^{-r'^2_1/2\sigma_s^2} e^{-im\phi'_1} e^{-ivr'^2_1/\delta_\mu^2} e^{-\frac{ik}{2z}(\mathbf{r}_1 - \mathbf{r}'_1)^2} d^2\mathbf{r}'_1 \\ &\int \left(\frac{\sqrt{2} r'_2}{\sigma_s} \right)^m e^{-r'^2_2/2\sigma_s^2} e^{im\phi'_2} e^{ivr'^2_2/\delta_\mu^2} e^{\frac{ik}{2z}(\mathbf{r}_2 - \mathbf{r}'_2)^2} d^2\mathbf{r}'_2. \end{aligned} \tag{4.13}$$

After some straightforward manipulations, the far-field CSD is given by

$$\begin{aligned} W(\mathbf{r}_1, \mathbf{r}_2; z) = &\frac{4\pi^2}{(\lambda z)^2} \left(\frac{k^2 r_1 r_2}{z^2} \right)^{|m|} e^{\frac{ik}{2z}(r_2^2 - r_1^2)} e^{im(\phi_2 - \phi_1)} \\ &\int \sqcap(v) \frac{1}{(2|\alpha|)^{2(|m|+1)}} e^{-\frac{(kr_1/z)^2}{4\alpha^*}} e^{-\frac{(kr_2/z)^2}{4\alpha}} dv, \end{aligned} \tag{4.14}$$

where $\alpha = \frac{1}{2\sigma_s^2} - \frac{iv}{\delta_\mu^2} - \frac{ik}{2z}$. Appendix D shows details of the derivation, and Appendix E lists a method to implement the calculation numerically.

Figure 4.6 illustrates the evolution of the cross-spectral density on propagation, showing its behavior at the source plane, 1 km, 2 km, and 3 km, for three different values of m . It can be seen that, in all cases, the CSD shifts toward the origin at $z \approx 1$ km (shown in the zoomed-in subplot); this is a manifestation of the self-

focusing effect of the beams. At z >1 km, CSDs start spreading as the free-space diffraction becomes dominant. The correlation vortex of each beam stays at the origin on propagation, which demonstrates that these correlation vortices are stable on propagation. The ring dislocations, which appear as lines of amplitude zero in the higher-order beams, diminish near the focal region (shown in the zoomed-in subplot) and reappear for z >1 km.

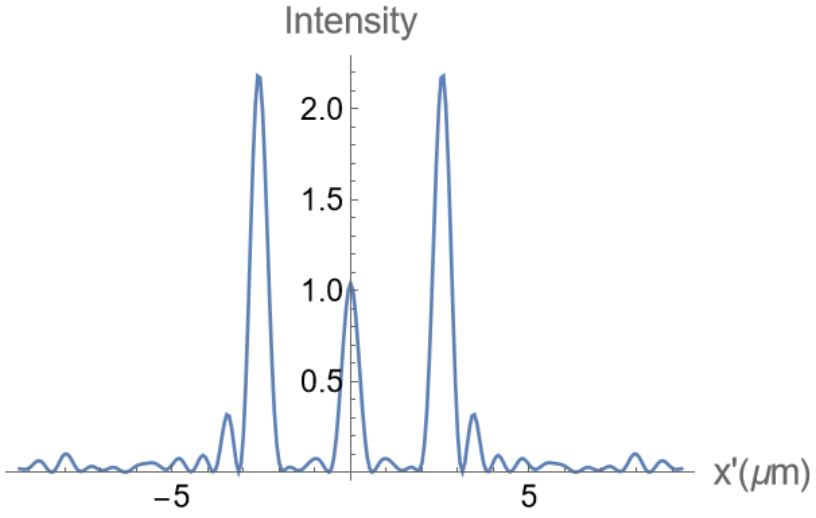

(a)

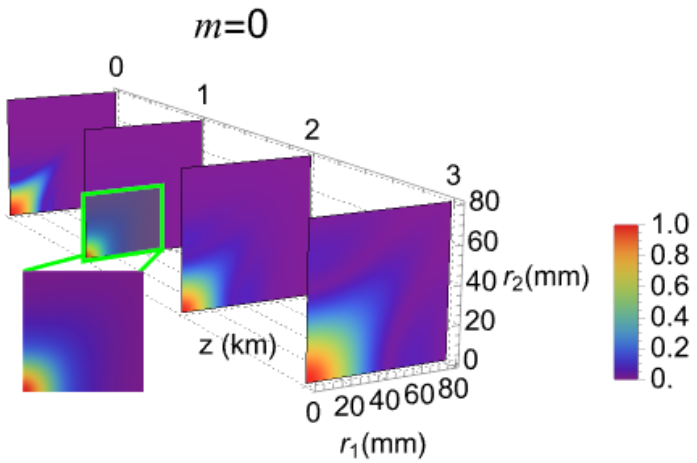

(b)

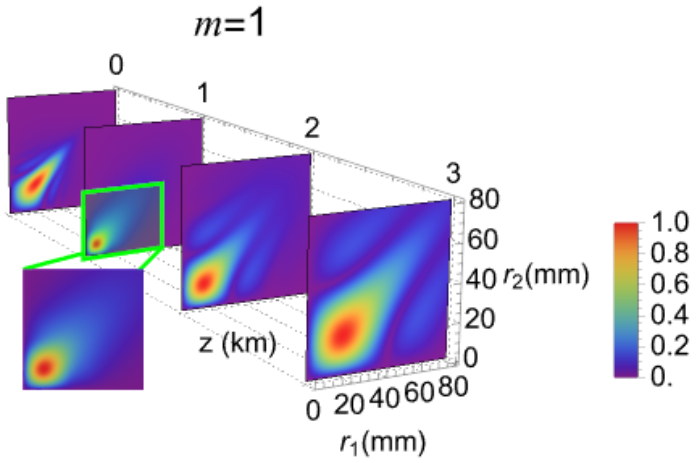

(c)

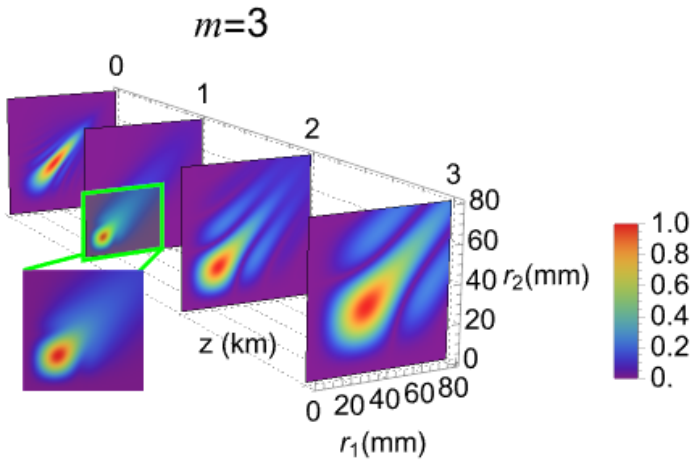

Figure 4.6: Cross-spectral densities of circularly coherent LG beams on propagation with an azimuthal order of m=0, m=1, and m=3, with $\sigma_s = 0.02\,\mathrm{m}$, $\delta_\mu = 0.044\,\mathrm{m}$, and $\lambda = 632.8\,\mathrm{nm}$ at the source plane, 1 km, 2 km, and 3 km, respectively.

4.4.2 Spectral degree of coherence

Figure 4.7 plots the evolution of the spectral degree of coherence on propagation for the same azimuthal orders. It can be derived that the spectral degree of coherence remains unity along the diagonal ($\mu = 1$). The ring dislocations, which are represented by lines of amplitude zero, can be seen clearly in the spectral degree of coherence, demonstrating that they are a result of the correlation structure of the beam. It is to be noted that the beams typically exhibit a higher coherence for small values of r_1 and r_2, representing a "plateau" of coherence. This indicates that circularly coherent beams are highly coherent near the beam core. This plateau contracts at $z \approx 1\,\text{km}$, coinciding with the overall focusing of the beam (as shown in the zoomed-in subplots), and expands for $z > 1\,\text{km}$, indicating a larger coherent area at the beam center.

(a)

(b)

(c)

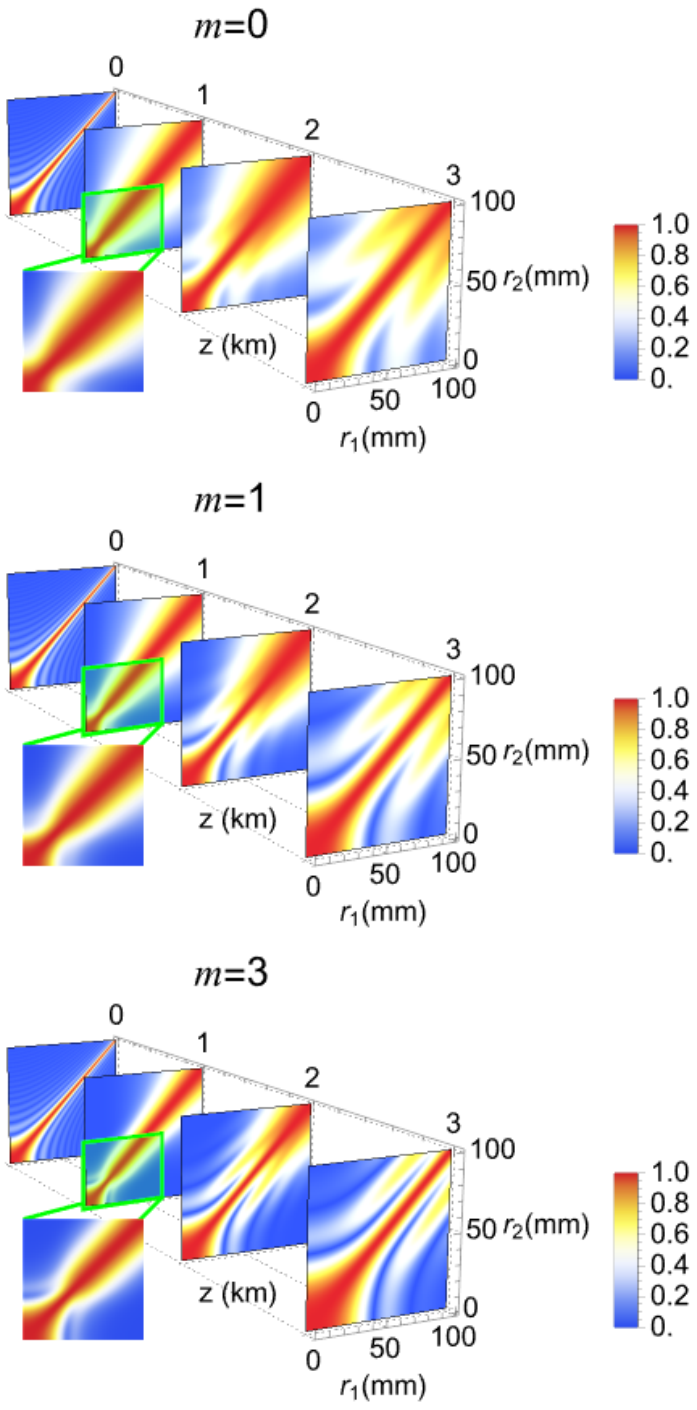

Figure 4.7: Spectral degree of coherence of circularly coherent LG beams on propagation with an azimuthal order of m=0, m=1, and m=3, with $\sigma_s = 0.02\,\mathrm{m}$, $\delta_\mu = 0.044\,\mathrm{m}$, and $\lambda = 632.8\,\mathrm{nm}$ at the source plane, 1 km, 2 km, and 3 km, respectively.

4.4.3 Amplitude and phase under a fixed observing point

In Figs. 4.8 and 4.9, the amplitude and phase profiles of the beams on propagation are shown, by fixing r_1 and then plotting the CSD in Cartesian coordinates of r_2 (x_2 and the y_2 directions). The fixed observing points are r_1=0.18 mm, 0.27 mm, and 0.44 mm for the three azimuthal modes. The circularly coherent beams maintain both the zero amplitude and spiral phase structure on the beam axis, a property that makes them intriguing candidates for applications such as free-space optical communication. For long propagation distances, the phase pattern develops its own twist due to the quadratic Fresnel operator, which is expected for any vortex beam on propagation.

(a)

(b)

(c)

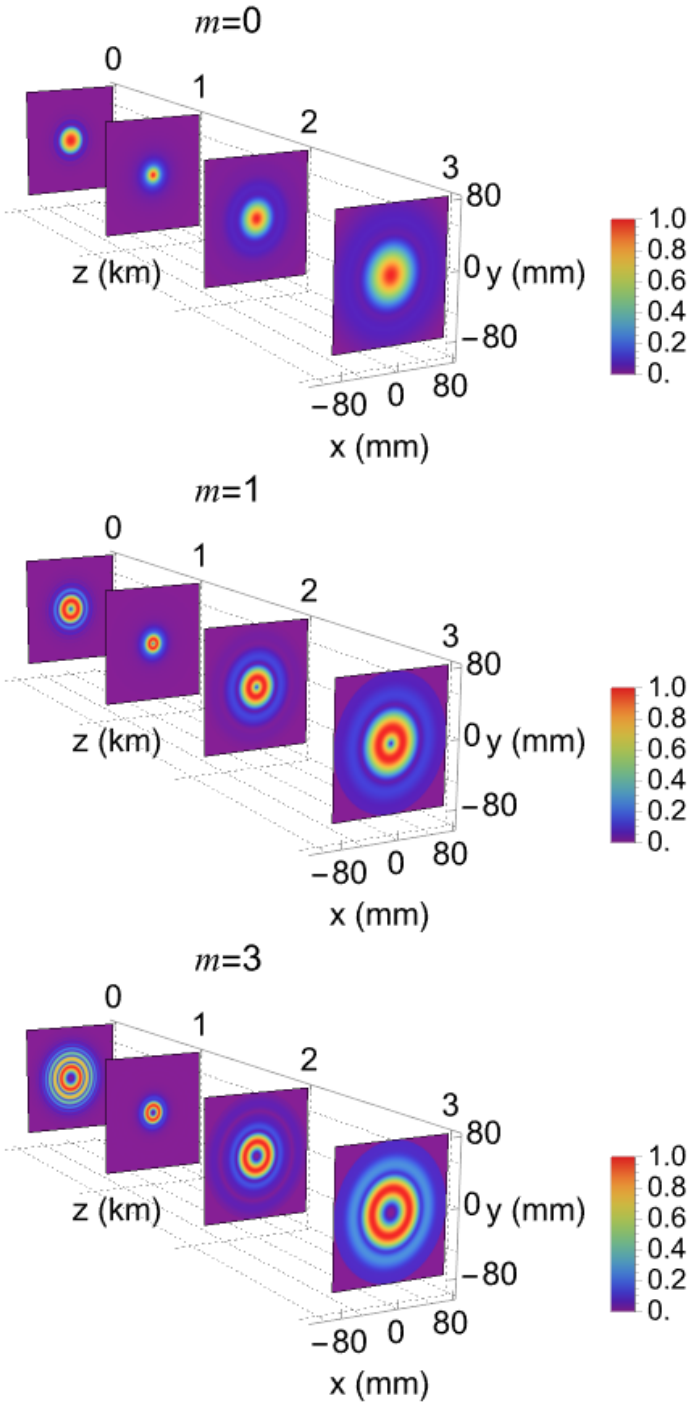

Figure 4.8: Amplitude of CSDs of circularly coherent LG beams on propagation with an azimuthal order of m=0, m=1, and m=3 under a fixed observing point, r_1, with $\sigma_s = 0.02\,\mathrm{m}$, $\delta_\mu = 0.044\,\mathrm{m}$, and $\lambda = 632.8\,\mathrm{nm}$ at the source plane, 1 km, 2 km, and 3 km, respectively. Observing points are $r_1 = 0.18\,\mathrm{mm}$, $0.27\,\mathrm{mm}$, and $0.44\,\mathrm{mm}$, respectively.

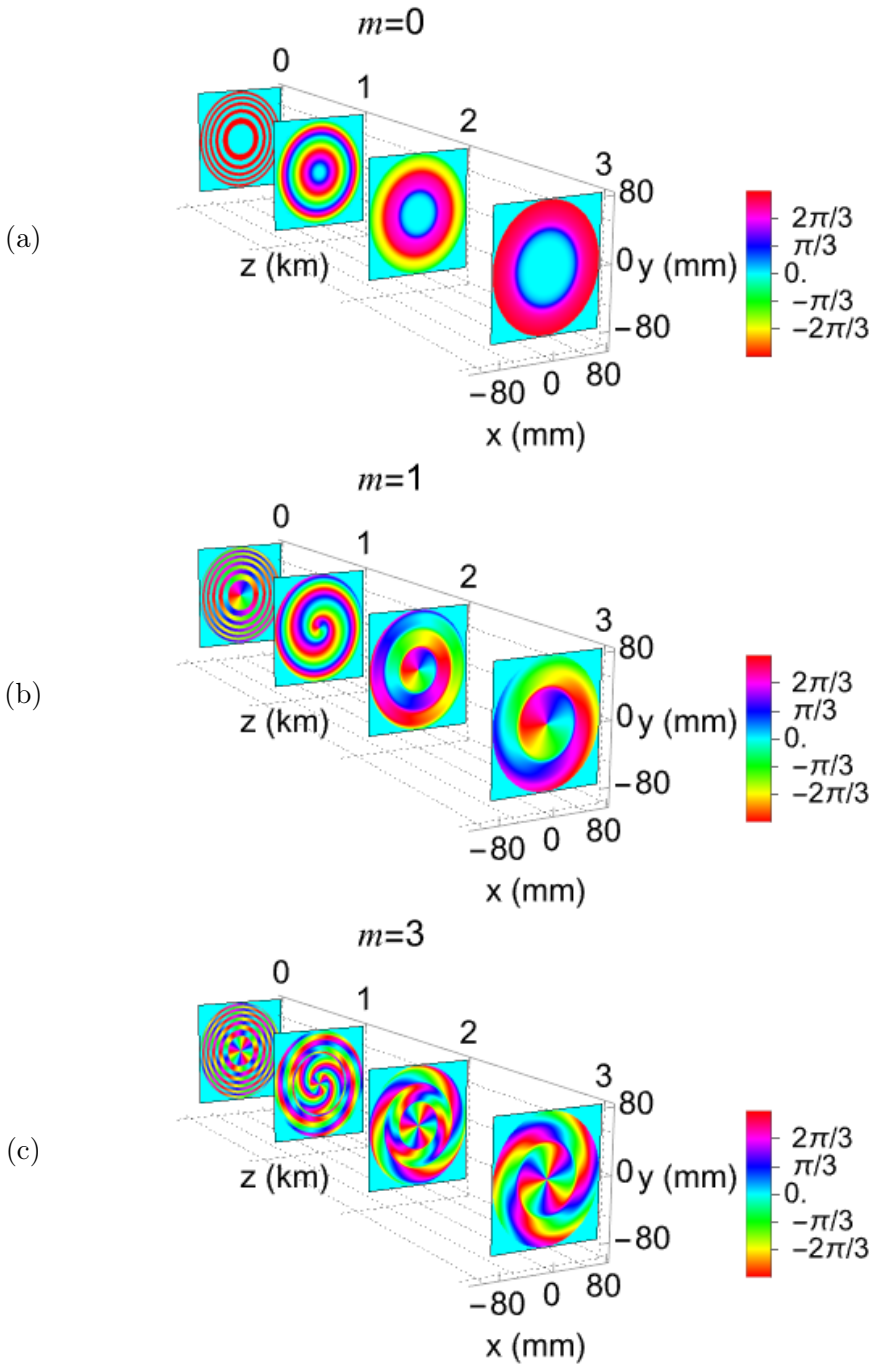

Figure 4.9: Phase of CSDs of circularly coherent LG beams on propagation with an azimuthal order of m=0, m=1, and m=3 under a fixed observing point, r_1, with $\sigma_s = 0.02$ m, $\delta_\mu = 0.044$ m, and $\lambda = 632.8$ nm at the source plane, 1 km, 2 km, and 3 km, respectively. Observing points are $r_1 = 0.18$ mm, 0.27 mm, and 0.44 mm, respectively.

4.5 Self-focusing Effect of Circular Coherence

4.5.1 Self-focusing of circularly coherent vortex beams

As already noted, the self-focusing effect of circularly coherent vortex beams arises from the quadratic phase term, $\exp(-ivr_i^2/\delta_\mu^2)$, in Eq. (4.13), which is the equivalent to a paraxial lens transmittance $\exp(-ikr^2/2f)$. By equating the two expressions, it can be derived that $\delta_\mu = \sqrt{2vf/k}$, therefore a smaller δ_μ will lead to a smaller focal length, f, or stronger focusing power of the circularly coherent vortex beams.

Figure 4.10 compares the propagation profiles of coherent vortex beams and the circularly coherent vortex beam. The circular coherent beams clearly show a focusing region. The focal length is determined by the coherence length, δ_μ. Appendix F includes the numerical method for calculating the beam profiles on propagation.

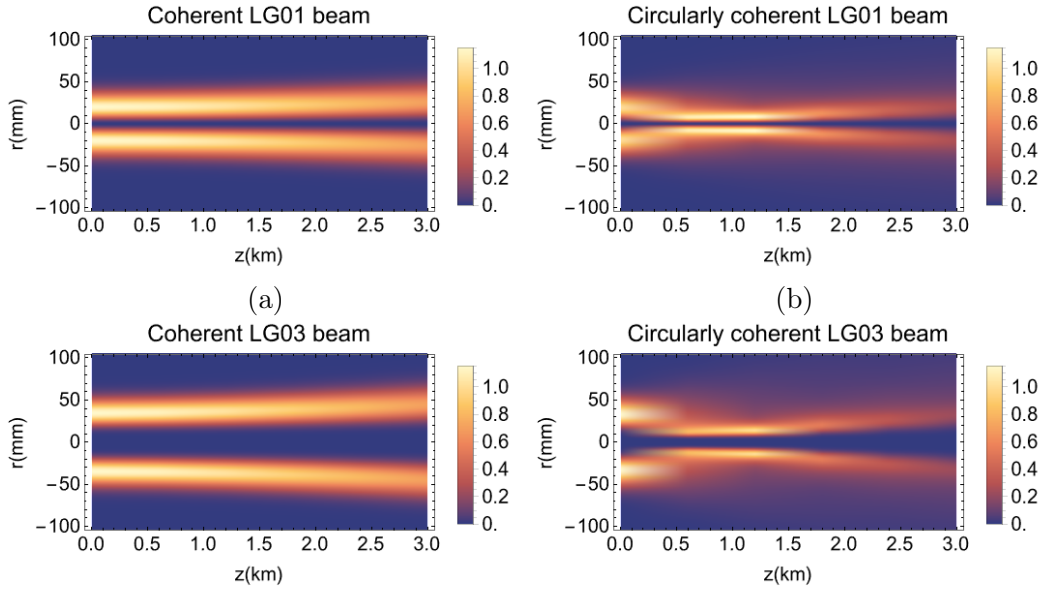

Figure 4.10: Propagation profiles of (a) coherent LG01, (b) circularly coherent LG01, and (c) coherent LG03, and (d) circularly coherent LG03, with $\sigma_s = 0.02\,\mathrm{m}$ and $\delta_\mu = 0.044\,\mathrm{m}$.

4.5.2 Self-focusing of superimposed LG±04 beams

To better illustrate the self-focusing effect of the circular coherence, a comparison of propagation profiles between the intensity of a coherent beam (constructed by the superposition of two LG beams with an azimuthal order of $m = \pm 4$, with a Rayleigh distance of 3972 m) and the spectral density of the superimposed beams with circular coherence is shown in Fig. 4.11. Circularly coherent superimposed beams show a focal region in the range of $z \in [0.5, 1.5]$ km. The focal length is determined by both the beam width, σ_s, and the parameter, δ_μ, of the spectral degree of coherence: the smaller δ_u, the stronger focusing power of the circularly coherent superimposed beams.

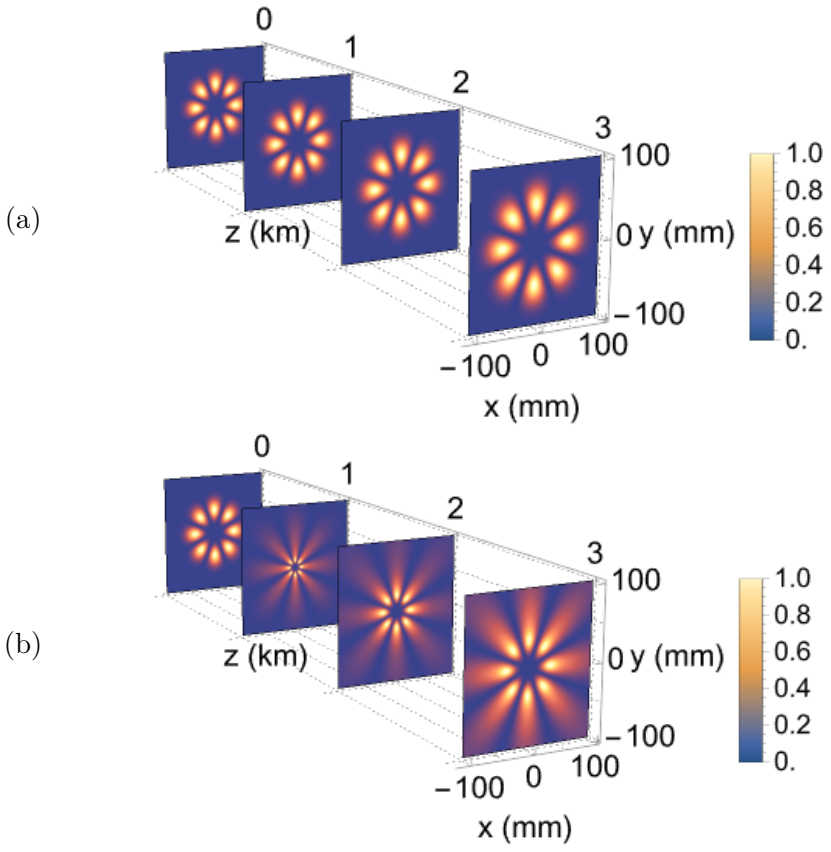

Figure 4.11: Comparison of (a) intensity of a coherent beam and (b) spectral density of the beam with circular coherence, constructed by the superposition of LG beams with an azimuthal order of $m = 4$ and $m =$ -4, with $\sigma_s = 0.02$ m, $\delta_\mu = 0.044$ m, and $\lambda = 632.8$ nm, propagating from the source plane upto 3 km.

4.5.3 Comparison of focal regions by a lens and a circular coherence beam

It is natural to ask if the self-focusing property of circular coherence can be utilized for creating a focal spot for imaging application. Therefore, the propagation profile of a coherent beam focused by a lens is compared to that of a self-focusing circular coherence beam. For the coherent system, the lens has a focal length of 5m and a lens transmittance of $t(r) = \cos^8(\pi r/D)$, where D is the aperture size. For the self-focusing circular coherence beam, its component coherent field has the same expression of the lens transmittance, $U(r) = \cos^8(\pi r/D)$, and its spectral degree of coherence has a coherence length, $\delta_\mu = 0.0017$m. Figure 4.12a shows the focusing profile of the coherent beam and Figure 4.12b shows the focusing profile of the self-focusing circular coherence beam. The intensity distribution in the focal region of the self-focusing circularly coherent beam appears smoother (indicating a lower contrast) than that of the coherent beam, which is common for partially coherent imaging.

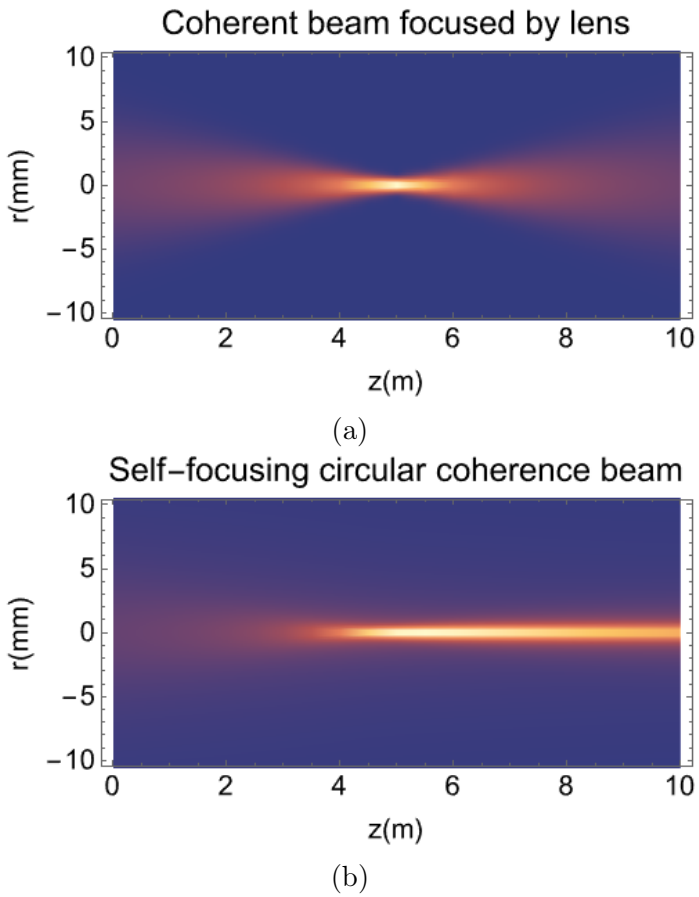

Figure 4.12: Comparison of focal regions of (a) a coherent beam focused by a lens and (b) a self-focusing circular coherence beam, with $\delta_\mu = 0.0017\,\text{m}$, and $\lambda = 632.8\,\text{nm}$.

4.5.4 Focal spot of superimposed circularly coherent LG±04 beams

As circularly coherent beams are perfectly coherent in the azimuthal direction of any ring that is concentric to the beam axis, the contrast of a circularly coherent focal spot in azimuthal direction near the beam axis is assumed be comparable to that of a coherent focal spot. To verify this assumption, the propagation profiles of a superposition of LG±04 beams (with a beam pattern consisting of petal-shaped beamlets in azimuthal direction) focused by a lens ($f = 1$ km) is compared to that of a self-focusing circularly coherent counterpart beam (δ_μ=0.0025m), as shown in Figure 4.13. The coherent beam is focused by a lens with a uniform transmittance, and its focal spot maintains its original beam pattern (by assuming the focal region is

free of aberrations). The focal spot of the circularly coherent beam shows a smoother distribution in the radial direction. However, the contrast is comparable to that of the coherent beam in the azimuthal direction near the beam central axis. The component beamlets are clear without reduced contrast in between. This result shows that the circularly coherent beam might be applied for lens-less imaging in cases where the image contrast in azimuthal direction is important.

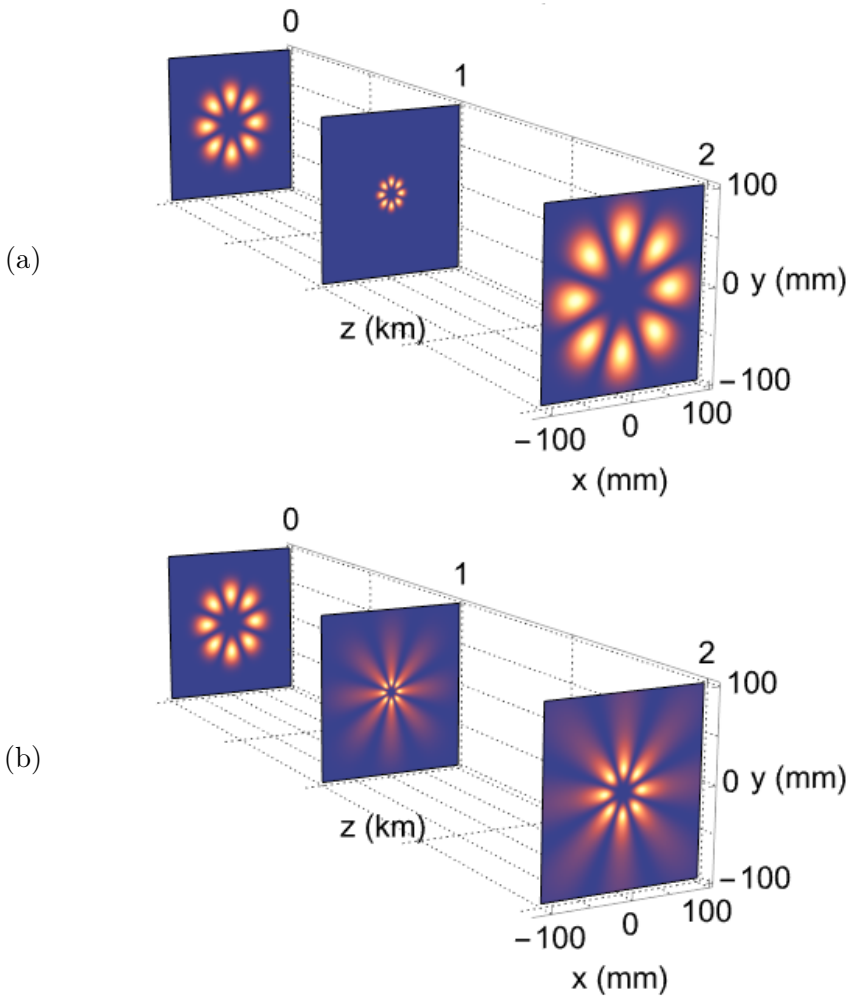

Figure 4.13: Comparison of focal regions of (a) the superposition of coherent LG±04 beam focused by a lens and (b) self-focusing circularly coherent counterpart beam, with $\delta_\mu = 0.0025\,\mathrm{m}$, and $\lambda = 632.8\,\mathrm{nm}$.

4.6 Experiment for Measuring Circularly Coherent Vortex Beams

In the introduction of circular coherence by Santarsiero and Gori, a circularly coherent field was generated by a longitudinal line source collimated an objective lens [76], which was proposed to be formed by a lens-mirror-beam splitter system[78]. Here, an alternative configuration for generating circularly coherent vortex beams is shown as below.

Here, the proposed source consists of a laser and two objective lenses, one which moves back and forth along the optical path within a certain range, a, and one which is fixed. The oscillation motion of the front objective lens shifts the position of the focal point (an approximate point source) between the two objective lenses so that optical fields have different radius of curvatures after transmitted by the rear objective lens. The optical field at the back focal plane of the rear objective lens is expressed by

$$U(\mathbf{r}, z) = \frac{-i}{\lambda f} e^{ik(z+f)} e^{\frac{ik}{2f}(1-\frac{z}{f})\mathbf{r}^2}, \tag{4.15}$$

where z is the position offset of the moving objective lens, f is the focal length of the rear objective lens, and the intensity of the focal point is normalized (by assuming the focal point's intensity is uniform as the objective lens moves). Subsequently, the CSD is calculated by integrating over the two-point correlation of the optical field over the traveling distance of the moving lens, which is given by

$$\begin{aligned} W(\mathbf{r}_1, \mathbf{r}_2) =& \frac{1}{a(\lambda f)^2} \int_{-a/2}^{a/2} e^{\frac{ikz}{2f^2}(r_2^2 - r_1^2)} dz \\ =& \frac{1}{a(\lambda f)^2} \mathrm{sinc}\left[\frac{ka\,(r_2^2 - r_1^2)}{4\pi f^2}\right]. \end{aligned} \tag{4.16}$$

Accordingly, the spectral degree of coherence, $\mu = \mathrm{sinc}\left[\frac{ka\left(r_2^2 - r_1^2\right)}{4\pi f^2}\right]$. In the experiment, the moving objective lens can be carried by a stage, driven by a piezoelectric motor with an oscillation frequency ω. Alternatively, a SLM can be a practical appa-

ratus for creating the circular coherence. An experiment setup proposed to generate and measure circularly coherent vortex beams is shown in Fig. 4.14. The circularly coherent field is created by a laser source, a moving objective lens, and a fixed objective lens then reflected by a spatial light modulator (SLM) containing a binary fork hologram to provide the spiral phase structure and the intensity profile of a vortex beam. Subsequently, the circularly coherent beam goes through a pinhole mask to project an interference fringe through an objective lens on the CCD camera. Pinhole positions are adjustable so that the degree of coherence of any pair of concentric rings are measurable.

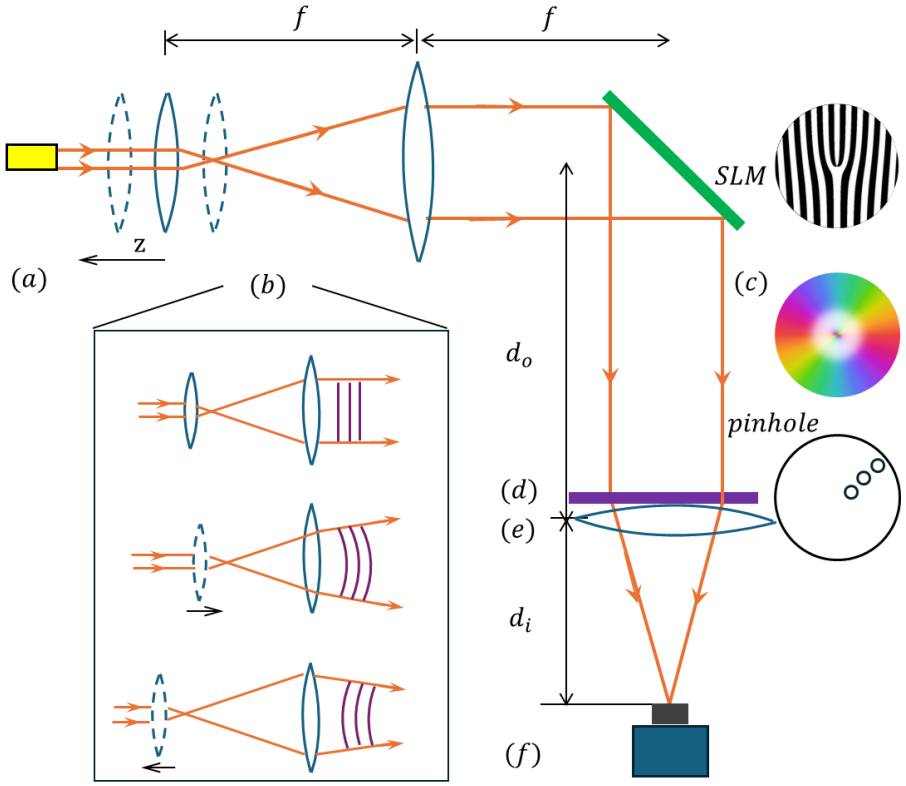

Figure 4.14: Experiment setup for measuring circularly coherent vortex beams. A circularly coherent field is created by (a) a laser and (b) a moving lens and a fixed lens and reflected by (c) a SLM to impose the circular coherence upon a vortex beam. The circularly coherent vortex beam goes through (d) a Young's pinhole mask with adjustable pinholes to measure the spectral degree of coherence of any concentric rings. The interference fringe is projected by (e) an objective onto (f) a CCD.

4.7 Discussion and Conclusion

This chapter demonstrates the paraxial propagation and coherence properties of circularly coherent vortex beams, which are perfectly coherent for points located on any concentric ring in the beam transverse plane. These beams are a generalization of the original circularly coherent beams introduced by Santarsiero et al. [76]. The simulation results show that the circular coherence is preserved on propagation, and correlation singularities, in the form of correlation vortices and ring dislocations, manifest for higher-order singularities.

These circularly coherent vortex beams show the self-focusing property of their original non-vortex counterparts. The focal region formed by a coherent beam focused by a lens and that formed by a self-focusing beam are compared: the circularly coherent focal spot can have a contrast in azimuthal direction near the beam axis comparable to that of a coherent beam, which illustrates a potential application in imaging.

It is to be noted that these beams have already shown promise for propagation through atmospheric turbulence, as a recent theoretical study demonstrated [79]. Furthermore, other researchers have looked at a broader class of self-focusing partially coherent beams of which circular coherence is a special case [80]; those beams have also been found to be resistant to turbulence effects in a recent study [81]. Most of the beams considered in that self-focusing class, however, do not have perfect circular coherence; the study described in this chapter is a complement to their work that concentrates on the circular coherent case.

In future work, we hope to investigate the position stability of circularly coherent vortex beams under a series of turbulence conditions. A study has demonstrated the performance of these beams under turbulence conditions in terms of orbital angular momentum (OAM) spectrum [79]. We want to further look at the amplitude and the phase of CSDs under a fixed observing point, the spectral degree of coherence,

and the amplitude of CSDs on propagation under turbulence conditions. We are also interested in encoding a superoscillatory pattern onto these beams and evaluate their performance, including but not limited to the effect of self-focusing of circular coherence on superoscillatory fields. The results might indicate the potential of applying circularly coherent superoscillatory fields with vortex structures for super-resolution imaging.

CHAPTER 5: SUMMARY AND FUTURE WORK

5.1 Summary

This dissertation work developed the concept of controlling superoscillation-based imaging with polarization and coherence. Superoscillation is a physical phenomenon that shows local oscillations of a band-limited signal that fluctuate more rapidly than the fastest Fourier component of the signal. Because the light spot from a superoscillatory wave can be narrower than the Rayleigh spot of traditional lens systems, superoscillatory imaging has been developed to achieve super-resolution. As shown in the review of superoscillatory imaging methods in Chapter 1, although superoscillatory imaging has demonstrated the ability to surpass the classic resolution limit, problems associated with this technique need to be solved.

One of the problems that directly challenges the application of superoscillatory imaging is the difficulty in designing and manufacturing a device to generate superoscillatory waves. In Chapter 2, mathematical formulas were applied to simplify filter profiles based on a previous method. The new designed filters not only generated superoscillatory field, but also had only one filtering profile, either a phase profile or an amplitude profile, which provided a potential to reduce the difficulty in manufacturing. Simulation results illustrated the superoscillatory spots generated by the designed filter. Energy efficiency of a phase-only type of filter was the same as that of a complex filter.

Through literature reviews, it is immediately obvious that a significant problem of superoscillatory imaging is large sidelobes coexisting with the superoscillatory central lobe. Although optimization algorithms might be able to solve this problem, there is a lack of explanation of how these methods work from a physics perspective. In

Chapter 3, by considering the transverse electromagnetic wave nature of light, a vector superoscillatory field was conceptualized to avoid sidelobes in the imaging process; only light signals from the central lobe (with a unique polarization state from that of sidelobes) are scattered toward a detector. A proposed imaging system incorporated a light source to provide a vector superoscillatory field illumination in the image plane. Simulated images of Rayleigh scatters under vector superoscillatory field illumination showed a better visual resolution than those illuminated by the classic Rayleigh spot. The final section of the chapter proposed a liquid crystal device to generate a vector superoscillatory field.

Modern studies of impacts of partial coherence on imaging, and the most recent study of behaviors of superoscillation on propagation, led to the study of circularly coherent vortex beams in free-space propagation in Chapter 4. It shows how circular coherence, with points on concentric rings that are perfectly coherent, can be considered for studying superoscillatory imaging. To achieve this goal, circularly coherent vortex beams were created (with spiral phase structures located at beam centers), which then demonstrates the second-order coherence properties of the beams, both at the source plane and on free-space propagation. It is shown that the beams maintain a circular coherence, although their expression of degree of coherence changes on propagation. It is also shown that the spiral phase structure remains intact. Furthermore, an experiment setup shows how a circular coherence source can be created, imposed on vortex beams, and measured for its degree of coherence. The maintained circular coherence on propagation together with the self-focusing effect show the potential of circularly coherent vortex beams for superoscillatory imaging.

5.2 List of Contributions

1. Theoretical derivation of two-dimensional image field by numerical window Fourier transform.

2. Design of phase-only and amplitude-only superoscillatory filter profiles.

3. Design of an imaging system incorporated with a vector superoscillatory field illumination.

4. Extension of Foldy-Lax method for calculating the intensity of scattered field.

5. Development of a two-dimensional numerical Hankel transform algorithm for optical beam propagation from Fresnel zone to Fraunhofer zone.

5.3 List of Related Publications

1. Qi, Rui, and Gregory J. Gbur. "Simplified superoscillatory lenses for super-resolution imaging." JOSA A 39.12 (2022): C116-C125.

2. Qi, Rui, and Greg Gbur. "Super-resolution imaging system developed from vector superoscillatory field illumination." Optics Letters 48.16 (2023): 4284-4287.

3. Shiri, Arash, Rui Qi, and Greg Gbur. "Circularly coherent vortex beams optimized for propagation through turbulence." JOSA A 41.6 (2024): B127-B134.

4. Rui Qi, Shiri, Arash, and Greg Gbur. "Circularly Coherent Vortex Beams with Coherence Singularities in Free-space Propagation." Submit to JOSA.

5.4 Future Work

Several directions of future work are listed as follows.

Circularly coherent superoscillatory image field

As circularly coherent vortex beams have demonstrated self-focusing effect on propagation, superoscillatory field with circular coherence might achieve a narrower superoscillatory spot than that of a coherent field. A circularly coherent superoscillatory field be obtained in the following ways:

1. Have the scalar field at the aperture plane (in Chapter 2) multiply an additional phase factor (representing a lens transmittance) as the source plane field.

2. Have the source plane field multiply the degree of coherence of circular coherence.

3. Propagate the field to an image plane in free space.

Circularly coherent beams under turbulence

Investigation is to be conduction for the stability of circularly coherent vortex beams under a broad range of turbulence conditions, with an eye towards optimizing them for free-space optical communications.

Binary superoscillatory filter

Unlike the step-like phase-only filter developed in Chapter 2, binary lenses, with an amplitude transmittance of either 0 or 1, can be an alternative to the step-like phase-only filter. In future work, mathematical formula for generating a binary profile is to be investigated.

REFERENCES

[1] L. Rayleigh, "Xxxi. investigations in optics, with special reference to the spectroscope.," *The London, Edinburgh, and Dublin Philosophical Magazine and Journal of Science*, vol. 8, no. 49, pp. 261–274, 1879.

[2] E. Abbe, "Xv.the relation of aperture and power in the microscope (continued).," *Journal of the royal microscopical society*, vol. 3, no. 6, pp. 790–812, 1883.

[3] M. Minsky, "Memoir on inventing the confocal scanning microscope," *Scanning*, vol. 10, no. 4, pp. 128–138, 1988.

[4] S. W. Hell, "Improvement of lateral resolution in far-field fluorescence light microscopy by using two-photon excitation with offset beams," *Optics communications*, vol. 106, no. 1-3, pp. 19–24, 1994.

[5] S. W. Hell and J. Wichmann, "Breaking the diffraction resolution limit by stimulated emission: stimulated-emission-depletion fluorescence microscopy," *Optics letters*, vol. 19, no. 11, pp. 780–782, 1994.

[6] M. J. Rust, M. Bates, and X. Zhuang, "Sub-diffraction-limit imaging by stochastic optical reconstruction microscopy (storm)," *Nature methods*, vol. 3, no. 10, pp. 793–796, 2006.

[7] D. W. Pohl and D. Courjon, *Near field optics*, vol. 242. Springer Science & Business Media, 2012.

[8] J. B. Pendry, "Negative refraction makes a perfect lens," *Physical review letters*, vol. 85, no. 18, p. 3966, 2000.

[9] K. S. Youngworth and T. G. Brown, "Focusing of high numerical aperture cylindrical-vector beams," *Optics Express*, vol. 7, no. 2, pp. 77–87, 2000.

[10] C.-C. Sun and C.-K. Liu, "Ultrasmall focusing spot with a long depth of focus based on polarization and phase modulation," *Optics letters*, vol. 28, no. 2, pp. 99–101, 2003.

[11] K. Kitamura, K. Sakai, and S. Noda, "Sub-wavelength focal spot with long depth of focus generated by radially polarized, narrow-width annular beam," *Optics express*, vol. 18, no. 5, pp. 4518–4525, 2010.

[12] Y. Kozawa, D. Matsunaga, and S. Sato, "Superresolution imaging via superoscillation focusing of a radially polarized beam," *Optica*, vol. 5, no. 2, pp. 86–92, 2018.

[13] B. Pant, H. K. Meena, and B. K. Singh, "Creation of pure longitudinal superoscillatory spot," *Optics Letters*, vol. 48, no. 5, pp. 1240–1243, 2023.

[14] L. Helseth, "Optical vortices in focal regions," *Optics Communications*, vol. 229, no. 1-6, pp. 85–91, 2004.

[15] S. Pereira and A. Van de Nes, "Superresolution by means of polarisation, phase and amplitude pupil masks," *Optics communications*, vol. 234, no. 1-6, pp. 119–124, 2004.

[16] T. Pu, J.-Y. Ou, N. Papasimakis, and N. I. Zheludev, "Label-free deeply subwavelength optical microscopy," *Applied Physics Letters*, vol. 116, no. 13, 2020.

[17] Y. Zhang, X. Song, J. Xie, J. Hu, J. Chen, X. Li, H. Zhang, Q. Zhou, L. Yuan, C. Kong, *et al.*, "Large depth-of-field ultra-compact microscope by progressive optimization and deep learning," *Nature Communications*, vol. 14, no. 1, p. 4118, 2023.

[18] F. Wei, D. Lu, H. Shen, W. Wan, J. L. Ponsetto, E. Huang, and Z. Liu, "Wide field super-resolution surface imaging through plasmonic structured illumination microscopy," *Nano letters*, vol. 14, no. 8, pp. 4634–4639, 2014.

[19] B. S. Luk'yanchuk, R. Paniagua-Domínguez, I. Minin, O. Minin, and Z. Wang, "Refractive index less than two: photonic nanojets yesterday, today and tomorrow

invited

," *Opt. Mater. Express*, vol. 7, pp. 1820–1847, Jun 2017.

[20] A. Darafsheh, G. F. Walsh, L. Dal Negro, and V. N. Astratov, "Optical superresolution by high-index liquid-immersed microspheres," *Applied Physics Letters*, vol. 101, no. 14, 2012.

[21] A. V. Maslov and V. N. Astratov, "Imaging of sub-wavelength structures radiating coherently near microspheres," *Applied Physics Letters*, vol. 108, no. 5, 2016.

[22] A. Maslov, B. Jin, and V. Astratov, "Wave optics of imaging with contact ball lenses," *Scientific Reports*, vol. 13, no. 1, p. 6688, 2023.

[23] V. Astratov *et al.*, *Label-free super-resolution microscopy*. Springer, 2019.

[24] V. N. Astratov, Y. B. Sahel, Y. C. Eldar, L. Huang, A. Ozcan, N. Zheludev, J. Zhao, Z. Burns, Z. Liu, E. Narimanov, *et al.*, "Roadmap on label-free superresolution imaging," *Laser & Photonics Reviews*, vol. 17, no. 12, p. 2200029, 2023.

[25] R. E. Thompson, D. R. Larson, and W. W. Webb, "Precise nanometer localization analysis for individual fluorescent probes," *Biophysical journal*, vol. 82, no. 5, pp. 2775–2783, 2002.

[26] R. J. Ober, S. Ram, and E. S. Ward, "Localization accuracy in single-molecule microscopy," *Biophysical journal*, vol. 86, no. 2, pp. 1185–1200, 2004.

[27] D. Sheppard, B. Hunt, and M. W. Marcellin, "Super-resolution of imagery acquired through turbulent atmosphere," in *Conference Record of The Thirtieth Asilomar Conference on Signals, Systems and Computers*, vol. 1, pp. 81–85, IEEE, 1996.

[28] M. Tsang, R. Nair, and X.-M. Lu, "Quantum theory of superresolution for two incoherent optical point sources," *Physical Review X*, vol. 6, no. 3, p. 031033, 2016.

[29] Z. Zalevsky, D. Mendlovic, and A. W. Lohmann, "Understanding superresolution in wigner space," *JOSA A*, vol. 17, no. 12, pp. 2422–2430, 2000.

[30] S. A. Schelkunoff, "A mathematical theory of linear arrays," *The Bell System Technical Journal*, vol. 22, no. 1, pp. 80–107, 1943.

[31] P. Woodward and J. Lawson, "The theoretical precision with which an arbitrary radiation-pattern may be obtained from a source of finite size," *Journal of the Institution of Electrical Engineers-Part III: Radio and Communication Engineering*, vol. 95, no. 37, pp. 363–370, 1948.

[32] G. T. Di Francia, "Super-gain antennas and optical resolving power," *Il Nuovo Cimento (1943-1954)*, vol. 9, pp. 426–438, 1952.

[33] Y. Aharonov, J. Anandan, S. Popescu, and L. Vaidman, "Superpositions of time evolutions of a quantum system and a quantum time-translation machine," *Physical review letters*, vol. 64, no. 25, p. 2965, 1990.

[34] M. Berry, "Faster than fourier," *Quantum Coherence and Reality*, pp. 55–65, 1994.

[35] J. S. Anandan and J. L. Safko, "Quantum coherence and reality: In celebration of the 60th birthday of yakir aharonov," in *QUANTUM COHERENCE AND REALITY: In Celebration of the 60th Birthday of Yakir Aharonov*, pp. 1–386, World Scientific, 1994.

[36] M. V. Berry, "Evanescent and real waves in quantum billiards and gaussian beams," *Journal of Physics A: Mathematical and General*, vol. 27, no. 11, p. L391, 1994.

[37] W. Qiao, "A simple model of aharonov-berry's superoscillations," *Journal of Physics A: Mathematical and General*, vol. 29, no. 9, p. 2257, 1996.

[38] I. Chremmos and G. Fikioris, "Superoscillations with arbitrary polynomial shape," *Journal of Physics A: Mathematical and Theoretical*, vol. 48, no. 26, p. 265204, 2015.

[39] D. Slepian and H. O. Pollak, "Prolate spheroidal wave functions, fourier analysis and uncertainty i," *Bell System Technical Journal*, vol. 40, no. 1, pp. 43–63, 1961.

[40] P. J. S. Ferreira and A. Kempf, "Superoscillations: faster than the nyquist rate," *IEEE transactions on signal processing*, vol. 54, no. 10, pp. 3732–3740, 2006.

[41] G. Gbur, "Using superoscillations for superresolved imaging and subwavelength focusing," *Nanophotonics*, vol. 8, no. 2, pp. 205–225, 2019.

[42] M. Berry and S. Popescu, "Evolution of quantum superoscillations and optical superresolution without evanescent waves," *Journal of Physics A: Mathematical and General*, vol. 39, no. 22, p. 6965, 2006.

[43] N. I. Zheludev and G. Yuan, "Optical superoscillation technologies beyond the diffraction limit," *Nature Reviews Physics*, vol. 4, no. 1, pp. 16–32, 2022.

[44] P. H. van Cittert, "Die wahrscheinliche schwingungsverteilung in einer von einer lichtquelle direkt oder mittels einer linse beleuchteten ebene," *Physica*, vol. 1, no. 1-6, pp. 201–210, 1934.

[45] F. Zernike, "The concept of degree of coherence and its application to optical problems," *Physica*, vol. 5, no. 8, pp. 785–795, 1938.

[46] H. H. Hopkins, "The concept of partial coherence in optics," *Proceedings of the Royal Society of London. Series A. Mathematical and Physical Sciences*, vol. 208, no. 1093, pp. 263–277, 1951.

[47] H. H. Hopkins, "On the diffraction theory of optical images," *Proceedings of the Royal Society of London. Series A. Mathematical and Physical Sciences*, vol. 217, no. 1130, pp. 408–432, 1953.

[48] H. Hopkins, "Applications of coherence theory in microscopy and interferometry," *JOSA*, vol. 47, no. 6, pp. 508–526, 1957.

[49] E. Wolf, "A macroscopic theory of interference and diffraction of light from finite sources, i. fields with a narrow spectral range," *Proceedings of the Royal Society of London. Series A. Mathematical and Physical Sciences*, vol. 225, no. 1160, pp. 96–111, 1954.

[50] E. Wolf, "A macroscopic theory of interference and diffraction of light from finite sources ii. fields with a spectral range of arbitrary width," *Proceedings of the Royal Society of London. Series A. Mathematical and Physical Sciences*, vol. 230, no. 1181, pp. 246–265, 1955.

[51] E. Wolf, "New theory of partial coherence in the space-frequency domain. part ii: Steady-state fields and higher-order correlations," *JOSA A*, vol. 3, no. 1, pp. 76–85, 1986.

[52] T. D. Visser, G. Gbur, and E. Wolf, "Effect of the state of coherence on the three-dimensional spectral intensity distribution near focus," *Optics communications*, vol. 213, no. 1-3, pp. 13–19, 2002.

[53] G. Gbur and T. D. Visser, "Can spatial coherence effects produce a local minimum of intensity at focus?," *Optics letters*, vol. 28, no. 18, pp. 1627–1629, 2003.

[54] E. Wolf, "New theory of partial coherence in the space–frequency domain. part i: spectra and cross spectra of steady-state sources," *JOSA*, vol. 72, no. 3, pp. 343–351, 1982.

[55] J. Mays and G. Gbur, "Partially coherent superoscillations in the talbot effect," *Journal of Physics A: Mathematical and Theoretical*, vol. 55, no. 50, p. 504002, 2022.

[56] M. K. Smith and G. Gbur, "Construction of arbitrary vortex and superoscillatory fields.," *Optics Letters*, vol. 41, no. 21, pp. 4979–4982, 2016.

[57] M. K. Smith and G. Gbur, "Mathematical method for designing superresolution lenses using superoscillations.," *Optics Letters*, vol. 45, no. 7, pp. 1854–1857, 2020.

[58] G. Chen, Z.-Q. Wen, and C.-W. Qiu, "Superoscillation: from physics to optical applications.," *Light: Science & Applications*, vol. 8, pp. 1–23, June 2019.

[59] K. S. Rogers and E. T. Rogers, "Realising superoscillations: A review of mathematical tools and their application.," *Journal of Physics: Photonics*, vol. 2, p. 042004, August 2020.

[60] V. I. Adzhalov, M. A. Golub, S. V. Karpeev, I. N. Sisakian, and V. A. Soifer, "Multichannel computer-optics components matched to mode groups.," *Soviet Journal of Quantum Electronics*, vol. 20, pp. 136–139, Febrary 1990.

[61] W.-H. Lee, "Binary computer-generated holograms.," *Applied Optics*, vol. 18, pp. 3661–3669, November 1979.

[62] J. P. Kirk and A. L. Jones, "Phase-only complex-valued spatial filter.," *Journal of the Optical Society of America*, vol. 61, no. 8, pp. 1023–1028, 1971.

[63] T. W. Clark, R. F. Offer, S. Franke-Arnold, A. S. Arnold, and N. Radwell, "Comparison of beam generation techniques using a phase only spatial light modulator," *Opt. Express*, vol. 24, pp. 6249–6264, Mar 2016.

[64] G. H. Yuan, E. T. Rogers, and N. I. Zheludev, "Achromatic super-oscillatory lenses with sub-wavelength focusing," *Light: Science & Applications*, vol. 6, no. 9, pp. e17036–e17036, 2017.

[65] Y. Hu, S. Wang, J. Jia, S. Fu, H. Yin, Z. Li, and Z. Chen, "Optical superoscillatory waves without side lobes along a symmetric cut," *Advanced Photonics*, vol. 3, no. 4, pp. 045002–045002, 2021.

[66] M. Born and E. Wolf, *Principles of optics: electromagnetic theory of propagation, interference and diffraction of light*. Elsevier, 2013.

[67] C. F. Bohren and D. R. Huffman, "Particles small compared with the wavelength," in *Absorption and Scattering of Light by Small Particles*, John Wiley & Sons, 2008.

[68] L. L. Foldy, "The multiple scattering of waves. i. general theory of isotropic scattering by randomly distributed scatterers," *Physical Review*, vol. 67, p. 107, February 1945.

[69] M. Lax, "Multiple scattering of waves. ii. the effective field in dense systems," *Physical Review*, vol. 85, p. 621, February 1952.

[70] A. Rubano, F. Cardano, B. Piccirillo, and L. Marrucci, "Q-plate technology: a progress review," *Journal of the Optical Society of America B*, vol. 36, pp. D70–D87, February 2019.

[71] B. Pant, H. K. Meena, and B. K. Singh, "Creation of pure longitudinal superoscillatory spot," *Optics Letters*, vol. 48, pp. 1240–1243, February 2023.

[72] E. Wolf, *Introduction to the Theory of Coherence and Polarization of Light*. Cambridge university press, 2007.

[73] F. Gori and M. Santarsiero, "Devising genuine spatial correlation functions," *Optics letters*, vol. 32, no. 24, pp. 3531–3533, 2007.

[74] F. Gori and M. Santarsiero, "Devising genuine twisted cross-spectral densities," *Optics Letters*, vol. 43, no. 3, pp. 595–598, 2018.

[75] G. Piquero, M. Santarsiero, R. Martínez-Herrero, J. De Sande, M. Alonzo, and F. Gori, "Partially coherent sources with radial coherence," *Optics Letters*, vol. 43, no. 10, pp. 2376–2379, 2018.

[76] M. Santarsiero, R. Martínez-Herrero, D. Maluenda, J. De Sande, G. Piquero, and F. Gori, "Partially coherent sources with circular coherence," *Optics Letters*, vol. 42, no. 8, pp. 1512–1515, 2017.

[77] L. Mandel and E. Wolf, *Optical Coherence and Quantum Optics*. Cambridge university press, 1995.

[78] M. Santarsiero, R. Martínez-Herrero, D. Maluenda, J. De Sande, G. Piquero, and F. Gori, "Synthesis of circularly coherent sources," *Optics Letters*, vol. 42, no. 20, pp. 4115–4118, 2017.

[79] A. Shiri, R. Qi, and G. Gbur, "Circularly coherent vortex beams optimized for propagation through turbulence," *JOSA A*, vol. 41, no. 6, pp. B127–B134, 2024.

[80] Z. Mei, O. Korotkova, D. Zhao, and Y. Mao, "Self-focusing vortex beams," *Optics letters*, vol. 46, no. 10, pp. 2384–2387, 2021.

[81] M. Luo, M. Koivurova, M. Ornigotti, and C. Ding, "Turbulence-resistant self-focusing vortex beams," *New Journal of Physics*, vol. 24, p. 093036, sep 2022.

[82] B. E. Saleh and M. C. Teich, *Fundamentals of photonics*. john Wiley & sons, 2019.

[83] L. Yu, M. Huang, M. Chen, W. Chen, W. Huang, and Z. Zhu, "Quasi-discrete hankel transform," *Optics letters*, vol. 23, no. 6, pp. 409–411, 1998.

APPENDIX A: DERIVATION OF TWO-DIMENSIONAL INTENSITY DISTRIBUTION AT THE IMAGE PLANE

The intensity of the image point, (k,l), at the image plane, $I_{k,l}$, is obtained by substituting the transmittance of the phase-only filter in spatial frequency domain into Eq.(13), which is expressed as

$$\begin{aligned} I_{k,l} =& |A_{k,l}|^2 \\ =& |L^2 \Delta x' \Delta y' \int_0^p \int_0^p \exp\{i[\phi(f_x, f_y) + h(f_x, f_y) \cos\left(\frac{2\pi b f_x}{\Delta f_x}\right)]\} \\ & \exp\{-2\pi i(k f_x \Delta x' + l f_y \Delta y')\} \mathrm{d}f_x \mathrm{d}f_y|^2. \end{aligned} \tag{A.1}$$

Assume $p = \Delta f_x M = \Delta f_y N$, we express the integral over p as a summation of integrals over Δf_x and Δf_y. Thus,

$$\begin{aligned} A_{k,l} =& L^2 \Delta x' \Delta y' \sum_{n=0}^{N-1} \sum_{m=0}^{M-1} \int_{(n-\frac{1}{2})\Delta f_y}^{(n+\frac{1}{2})\Delta f_y} \int_{(m-\frac{1}{2})\Delta f_x}^{(m+\frac{1}{2})\Delta f_x} \\ & \exp\{i[\phi_{m,n}(f_x, f_y) + h_{m,n}(f_x, f_y) \cos\left(\frac{2\pi b f_x}{\Delta f_x}\right)]\} \\ & \exp\{-2\pi i(k f_x \Delta x' + l f_y \Delta y')\} \mathrm{d}f_x \mathrm{d}f_y. \end{aligned} \tag{A.2}$$

We assume that $\phi_{m,n}(f_x, f_y)$ and $h_{m,n}(f_x, f_y)$ are constants within the rang of a single pixel, $\{[(m-\frac{1}{2})\Delta f_x, (m+\frac{1}{2})\Delta f_x], [(n-\frac{1}{2})\Delta f_y, (n+\frac{1}{2})\Delta f_y]\}$, and then factor out $\exp(i\phi_{m,n})$. $A_{k,l}$ is simplified as

$$
\begin{aligned}
A_{k,l} =& L^2\Delta x'\Delta y' \sum_{n=0}^{N-1}\sum_{m=0}^{M-1} \exp(i\phi_{m,n}) \int_{(n-\frac{1}{2})\Delta f_y}^{(n+\frac{1}{2})\Delta f_y} \int_{(m-\frac{1}{2})\Delta f_x}^{(m+\frac{1}{2})\Delta f_x} \\
& \exp\{ih_{m,n}\cos\left(\frac{2\pi b f_x}{\Delta f_x}\right)\}\exp\{-2\pi i(kf_x\Delta x' + lf_y\Delta y')\}\mathrm{d}f_x\mathrm{d}f_y \\
=& L^2\Delta x'\Delta y' \sum_{n=0}^{N-1}\sum_{m=0}^{M-1} \exp(i\phi_{m,n}) \\
& \int_{(n-\frac{1}{2})\Delta f_y}^{(n+\frac{1}{2})\Delta f_y} \int_{(m-\frac{1}{2})\Delta f_x}^{(m+\frac{1}{2})\Delta f_x} \exp\{ih_{m,n}\cos\left(\frac{2\pi b f_x}{\Delta f_x}\right)\}\mathrm{d}f_x\mathrm{d}f_y \\
& \int_{(n-\frac{1}{2})\Delta f_y}^{(n+\frac{1}{2})\Delta f_y} \int_{(m-\frac{1}{2})\Delta f_x}^{(m+\frac{1}{2})\Delta f_x} \exp\{-2\pi i(kf_x\Delta x' + lf_y\Delta y')\}\mathrm{d}f_x\mathrm{d}f_y.
\end{aligned} \tag{A.3}
$$

Since $\cos\left(\frac{2\pi b f_x}{\Delta f_x}\right)$ is periodic, the integral

$$
\begin{aligned}
& \int_{(n-\frac{1}{2})\Delta f_y}^{(n+\frac{1}{2})\Delta f_y} \int_{(m-\frac{1}{2})\Delta f_x}^{(m+\frac{1}{2})\Delta f_x} \exp\{ih_{m,n}\cos\left(\frac{2\pi b f_x}{\Delta f_x}\right)\}\mathrm{d}f_x\mathrm{d}f_y \\
=& \int_{-\frac{1}{2}\Delta f_y}^{\frac{1}{2}\Delta f_y} \int_{-\frac{1}{2}\Delta f_x}^{\frac{1}{2}\Delta f_x} \exp\{ih_{m,n}\cos\left(\frac{2\pi b f_x}{\Delta f_x}\right)\}\mathrm{d}f_x\mathrm{d}f_y.
\end{aligned} \tag{A.4}
$$

Here, the integral

$$
\begin{aligned}
&\int_{(n-\frac{1}{2})\Delta f_y}^{(n+\frac{1}{2})\Delta f_y}\int_{(m-\frac{1}{2})\Delta f_x}^{(m+\frac{1}{2})\Delta f_x}\exp\{-2\pi i(kf_x\Delta x'+lf_y\Delta y')\}\mathrm{d}f_x\mathrm{d}f_y\\
=&(-\frac{1}{2\pi ik\Delta x'})\exp(-2\pi ikf_x\Delta x')\Big|_{(m-\frac{1}{2})\Delta f_x}^{(m+\frac{1}{2})\Delta f_x}\\
&(-\frac{1}{2\pi il\Delta y'})\exp(-2\pi ilf_y\Delta y')\Big|_{(n-\frac{1}{2})\Delta f_y}^{(n+\frac{1}{2})\Delta f_y}\\
=&(-\frac{1}{2\pi ik\Delta x'})\exp(-2\pi ikm\Delta f_x\Delta x')\\
&[\exp(-2\pi ik\tfrac{1}{2}\Delta f_x\Delta x')-\exp(2\pi ik\tfrac{1}{2}\Delta f_x\Delta x')]\\
&(-\frac{1}{2\pi il\Delta y'})\exp(-2\pi iln\Delta f_y\Delta y')\\
&[\exp(-2\pi il\tfrac{1}{2}\Delta f_y\Delta y')-\exp(2\pi il\tfrac{1}{2}\Delta f_y\Delta y')]\\
=&\exp(-2\pi ikm\Delta f_x\Delta x'-2\pi iln\Delta f_y\Delta y')\\
&\int_{-\frac{1}{2}\Delta f_x}^{\frac{1}{2}\Delta f_x}\int_{-\frac{1}{2}\Delta f_y}^{\frac{1}{2}\Delta f_y}\exp(-2\pi ik\Delta x'f_x-2\pi il\Delta y'f_y)\mathrm{d}f_x\mathrm{d}f_y.
\end{aligned}
\tag{A.5}
$$

Substitute Eq.(31) and Eq.(32) into Eq.(30), we have

$$
\begin{aligned}
A_{k,l}=&L^2\Delta x'\Delta y'\sum_{n=0}^{N-1}\sum_{m=0}^{M-1}\exp\{i\phi_{m,n}-2\pi i(km\Delta f_x\Delta x'+ln\Delta f_y\Delta y')\}\\
&\int_{-\frac{1}{2}\Delta f_y}^{\frac{1}{2}\Delta f_y}\int_{-\frac{1}{2}\Delta f_x}^{\frac{1}{2}\Delta f_x}\exp\{i[h_{m,n}\cos\left(\frac{2\pi bf_x}{\Delta f_x}\right)\\
&-2\pi(k\Delta x'f_x+l\Delta y'f_y)]\}\mathrm{d}f_x\mathrm{d}f_y.
\end{aligned}
\tag{A.6}
$$

Define $u=2\pi f_x/\Delta f_x$ and $v=2\pi f_y/\Delta f_y$, then $\mathrm{d}f_x=\frac{\Delta f_x}{2\pi}\mathrm{d}u$ and $\mathrm{d}f_y=\frac{\Delta f_y}{2\pi}\mathrm{d}v$. As a result,

$$
\begin{aligned}
A_{k,l}=&L^2\Delta x'\Delta y'\sum_{n=0}^{N-1}\sum_{m=0}^{M-1}\exp\{i\phi_{m,n}-2\pi i(km\Delta f_x\Delta x'+ln\Delta f_y\Delta y')\}\\
&\frac{\Delta f_x\Delta f_y}{4\pi^2}\int_{-\pi}^{\pi}\int_{-\pi}^{\pi}\exp\{i[h_{m,n}\cos(bu)-k\Delta x'\Delta f_xu-l\Delta y'\Delta f_yv]\mathrm{d}u\mathrm{d}v.
\end{aligned}
\tag{A.7}
$$

Besides, with the relations of $M = \frac{1}{\Delta x' \Delta f_x}$ and $N = \frac{1}{\Delta y' \Delta f_y}$, $A_{k,l}$ is further simplified as

$$\begin{aligned} A_{k,l} =& \frac{L^2}{MN} \sum_{n=0}^{N-1} \sum_{m=0}^{M-1} \exp\{i\phi_{m,n} - 2\pi i(\frac{km}{M} + \frac{ln}{N})\} \\ & \frac{1}{4\pi^2} \int_{-\pi}^{\pi} \int_{-\pi}^{\pi} \exp\{i[h_{m,n} \cos(bu) - \frac{k}{M}u - \frac{l}{N}v]\} \mathrm{d}u\mathrm{d}v. \end{aligned} \tag{A.8}$$

Define $S_{m,n}(k,l)$ as the scattering function, which is a function of position of the image point. $S_{m,n}(k,l)$ is expressed by

$$S_{m,n}(k,l) = \frac{1}{4\pi^2} \int_{-\pi}^{\pi} \int_{-\pi}^{\pi} \exp\{i[h_{m,n} \cos(bu) - \frac{k}{M}u - \frac{l}{N}v]\} \mathrm{d}u\mathrm{d}v. \tag{A.9}$$

Substitute Eq. (36) into Eq. (35), we have

$$A_{k,l} = \frac{L^2}{MN} \sum_{n=0}^{N-1} \sum_{m=0}^{M-1} \exp\{i[\phi_{m,n} - 2\pi(\frac{mk}{M} + \frac{nl}{N})]\} S_{m,n}(k,l), \tag{A.10}$$

which gives the two-dimensional field distribution at the image plane.

Finally, the intensity distribution at the image plane, $I_{k,l}$, is calculated by $I_{k,l} = |A_{k,l}|^2$.

APPENDIX B: SCATTERING CALCULATION WITH FOLDY-LAX METHOD FOR THREE PARTICLES

The scattered field is assumed to be a spherical wave, which relates to the illuminating field by a Green's function. Since both the illuminating field and the scattering field are vector field, we need to apply the Dyadic Green's function. The Dyadic Green's function is expressed by

$$\begin{aligned}\mathbf{G}(\mathbf{r},\mathbf{r}') =&(\mathbf{I}+\frac{1}{k^2}\nabla\nabla)\frac{\exp ik|\mathbf{r}-\mathbf{r}'|}{|\mathbf{r}-\mathbf{r}'|}\\ =&(\mathbf{I}+\frac{1}{k}\nabla\nabla)\frac{\exp ik\mathbf{r}_{12}}{\mathbf{r}_{12}},\end{aligned} \tag{B.1}$$

where $\mathbf{r}$ is the position of interest, $\mathbf{r}'$ is the position of a scatter, $\nabla\nabla$ is an operator of a double partial derivative. Basically, this function characterizes the field scattered by particles. If the incident field is $\mathbf{E}^{(i)}(\mathbf{r})$, the field scattered by the particle is given by

$$\mathbf{E}^{(s)}(\mathbf{r}) = \alpha\mathbf{G}(\mathbf{r},\mathbf{r}')\mathbf{E}^{(i)}(\mathbf{r}'), \tag{B.2}$$

where α is the scattering potential of the scatterer. By calculating the $\nabla\nabla$ operator in $\mathbf{G}(\mathbf{r},\mathbf{r}')$, we get a $\mathbf{G}$ matrix with 9 components.

$$\mathbf{G}(\mathbf{r},\mathbf{r}') = \begin{bmatrix}\mathbf{G}_{xx}(\mathbf{r},\mathbf{r}') & \mathbf{G}_{yx}(\mathbf{r},\mathbf{r}') & \mathbf{G}_{zx}(\mathbf{r},\mathbf{r}')\\ \mathbf{G}_{xy}(\mathbf{r},\mathbf{r}') & \mathbf{G}_{yy}(\mathbf{r},\mathbf{r}') & \mathbf{G}_{zy}(\mathbf{r},\mathbf{r}')\\ \mathbf{G}_{xz}(\mathbf{r},\mathbf{r}') & \mathbf{G}_{yz}(\mathbf{r},\mathbf{r}') & \mathbf{G}_{zz}(\mathbf{r},\mathbf{r}')\end{bmatrix}. \tag{B.3}$$

By applying the relation in Eq. (B.2), we have the scattered field of a single scatter.

$$\mathbf{E}^{(s)}(\mathbf{r}) = \alpha\begin{bmatrix}\mathbf{G}_{xx}(\mathbf{r},\mathbf{r}') & \mathbf{G}_{yx}(\mathbf{r},\mathbf{r}') & \mathbf{G}_{zx}(\mathbf{r},\mathbf{r}')\\ \mathbf{G}_{xy}(\mathbf{r},\mathbf{r}') & \mathbf{G}_{yy}(\mathbf{r},\mathbf{r}') & \mathbf{G}_{zy}(\mathbf{r},\mathbf{r}')\\ \mathbf{G}_{xz}(\mathbf{r},\mathbf{r}') & \mathbf{G}_{yz}(\mathbf{r},\mathbf{r}') & \mathbf{G}_{zz}(\mathbf{r},\mathbf{r}')\end{bmatrix}\begin{bmatrix}\mathbf{E}_x^{(i)}\\ \mathbf{E}_y^{(i)}\\ \mathbf{E}_z^{(i)}\end{bmatrix}, \tag{B.4}$$

For a field covering multiple scatterers, the total field is the sum of illuminating field and the total scattered field of all the particles. To simplify the calculation, we consider the detector as a scatterer, $j = 3$, with its scattering potential as 0. Then, we neglect all the points without a scatterer. Here, we have a total of three points involved in the calculation. In addition, we need to exclude the self-energy of each scatterer. Finally, the expression for the total electric field at a position interest is given by

$$\mathbf{E}(\mathbf{r}_i) = \mathbf{E}^i(\mathbf{r}_i) + \Sigma_{i\neq j}\alpha_j \mathbf{G}(\mathbf{r}_i, \mathbf{r}_j)\mathbf{E}(\mathbf{r}_j). \tag{B.5}$$

Then, we use matrix calculation to obtain the total field at the three positions (two particles and a detector) simultaneously.

$$\begin{bmatrix} \mathbf{E}(\mathbf{r}_1) \\ \mathbf{E}(\mathbf{r}_2) \\ \mathbf{E}(\mathbf{r}_3) \end{bmatrix} = \begin{bmatrix} \mathbf{E}^{(i)}(\mathbf{r}_1) \\ \mathbf{E}^{(i)}(\mathbf{r}_2) \\ \mathbf{E}^{(i)}(\mathbf{r}_3) \end{bmatrix} + \begin{bmatrix} \alpha_1 & \alpha_2 & \alpha_3 \\ \alpha_1 & \alpha_2 & \alpha_3 \\ \alpha_1 & \alpha_2 & \alpha_3 \end{bmatrix} \begin{bmatrix} \mathbf{G}(\mathbf{r}_1, \mathbf{r}'_1) & \mathbf{G}(\mathbf{r}_1, \mathbf{r}'_2) & \mathbf{G}(\mathbf{r}_1, \mathbf{r}'_3) \\ \mathbf{G}(\mathbf{r}_2, \mathbf{r}'_1) & \mathbf{G}(\mathbf{r}_2, \mathbf{r}'_2) & \mathbf{G}(\mathbf{r}_2, \mathbf{r}'_3) \\ \mathbf{G}(\mathbf{r}_3, \mathbf{r}'_1) & \mathbf{G}(\mathbf{r}_3, \mathbf{r}'_2) & \mathbf{G}(\mathbf{r}_3, \mathbf{r}'_3) \end{bmatrix} \begin{bmatrix} \mathbf{E}(\mathbf{r}_1) \\ \mathbf{E}(\mathbf{r}_2) \\ \mathbf{E}(\mathbf{r}_3) \end{bmatrix}, \tag{B.6}$$

Then, we have

$$(\mathbf{I} - \begin{bmatrix} \alpha_1 & \alpha_2 & \alpha_3 \\ \alpha_1 & \alpha_2 & \alpha_3 \\ \alpha_1 & \alpha_2 & \alpha_3 \end{bmatrix} \begin{bmatrix} \mathbf{G}(\mathbf{r}_1, \mathbf{r}'_1) & \mathbf{G}(\mathbf{r}_1, \mathbf{r}'_2) & \mathbf{G}(\mathbf{r}_1, \mathbf{r}'_3) \\ \mathbf{G}(\mathbf{r}_2, \mathbf{r}'_1) & \mathbf{G}(\mathbf{r}_2, \mathbf{r}'_2) & \mathbf{G}(\mathbf{r}_2, \mathbf{r}'_3) \\ \mathbf{G}(\mathbf{r}_3, \mathbf{r}'_1) & \mathbf{G}(\mathbf{r}_3, \mathbf{r}'_2) & \mathbf{G}(\mathbf{r}_3, \mathbf{r}'_3) \end{bmatrix}) \begin{bmatrix} \mathbf{E}(\mathbf{r}_1) \\ \mathbf{E}(\mathbf{r}_2) \\ \mathbf{E}(\mathbf{r}_3) \end{bmatrix} = \begin{bmatrix} \mathbf{E}^{(i)}(\mathbf{r}_1) \\ \mathbf{E}^{(i)}(\mathbf{r}_2) \\ \mathbf{E}^{(i)}(\mathbf{r}_3) \end{bmatrix} \tag{B.7}$$

Then, the electric field at positions of interest is

$$\begin{bmatrix} \mathbf{E}(\mathbf{r}_1) \\ \mathbf{E}(\mathbf{r}_2) \\ \mathbf{E}(\mathbf{r}_3) \end{bmatrix} = (\mathbf{I} - \begin{bmatrix} \alpha_1 & \alpha_2 & \alpha_3 \\ \alpha_1 & \alpha_2 & \alpha_3 \\ \alpha_1 & \alpha_2 & \alpha_3 \end{bmatrix} \begin{bmatrix} \mathbf{G}(\mathbf{r}_1, \mathbf{r}'_1) & \mathbf{G}(\mathbf{r}_1, \mathbf{r}'_2) & \mathbf{G}(\mathbf{r}_1, \mathbf{r}'_3) \\ \mathbf{G}(\mathbf{r}_2, \mathbf{r}'_1) & \mathbf{G}(\mathbf{r}_2, \mathbf{r}'_2) & \mathbf{G}(\mathbf{r}_2, \mathbf{r}'_3) \\ \mathbf{G}(\mathbf{r}_3, \mathbf{r}'_1) & \mathbf{G}(\mathbf{r}_3, \mathbf{r}'_2) & \mathbf{G}(\mathbf{r}_3, \mathbf{r}'_3) \end{bmatrix})^{-1} \begin{bmatrix} \mathbf{E}^{(i)}(\mathbf{r}_1) \\ \mathbf{E}^{(i)}(\mathbf{r}_2) \\ \mathbf{E}^{(i)}(\mathbf{r}_3) \end{bmatrix} \tag{B.8}$$

Next, we expand the incident field and the total field with its x, y, and z components as

$$\begin{bmatrix} \mathbf{E}(\mathbf{r}_1) \\ \mathbf{E}(\mathbf{r}_2) \\ \mathbf{E}(\mathbf{r}_3) \end{bmatrix} = \begin{bmatrix} \mathbf{E}_x(\mathbf{r}_1) \\ \mathbf{E}_x(\mathbf{r}_2) \\ \mathbf{E}_x(\mathbf{r}_3) \\ \mathbf{E}_y(\mathbf{r}_1) \\ \mathbf{E}_y(\mathbf{r}_2) \\ \mathbf{E}_y(\mathbf{r}_3) \\ \mathbf{E}_z(\mathbf{r}_1) \\ \mathbf{E}_z(\mathbf{r}_2) \\ \mathbf{E}_z(\mathbf{r}_3) \end{bmatrix}, \tag{B.9}$$

and

$$\begin{bmatrix} \mathbf{E}^{(i)}(\mathbf{r}_1) \\ \mathbf{E}^{(i)}(\mathbf{r}_2) \\ \mathbf{E}^{(i)}(\mathbf{r}_3) \end{bmatrix} = \begin{bmatrix} \mathbf{E}_x^{(i)}(\mathbf{r}_1) \\ \mathbf{E}_x^{(i)}(\mathbf{r}_2) \\ \mathbf{E}_x^{(i)}(\mathbf{r}_3) \\ \mathbf{E}_y^{(i)}(\mathbf{r}_1) \\ \mathbf{E}_y^{(i)}(\mathbf{r}_2) \\ \mathbf{E}_y^{(i)}(\mathbf{r}_3) \\ \mathbf{E}_z^{(i)}(\mathbf{r}_1) \\ \mathbf{E}_z^{(i)}(\mathbf{r}_2) \\ \mathbf{E}_z^{(i)}(\mathbf{r}_3) \end{bmatrix}, \tag{B.10}$$

And, we construct the $\mathbf{G}$ matrix as shown in figure below

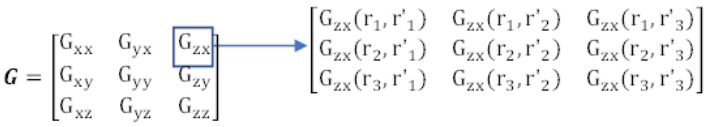

Figure B.1: Construction of a G matrix

Then, we can write Eq. (B.10) in a simplified form as

$$\mathbf{E}_q(\mathbf{r}_i) = (1 - \Sigma_{p=1}^{3}\Sigma_{j=1}^{3}\mathbf{G}_{p,q}(\mathbf{r}_i, \mathbf{r}_j))^{-1}\mathbf{E}_p^{(i)}(\mathbf{r}_j), \tag{B.11}$$

where p and q are the index of coordinates of x, y, and z, for electric field at positions of interest and scatterers, respectively. $\mathbf{r}_i$ and $\mathbf{r}_j$ are position vectors of positions of interest and scatterers, respectively.

Here, we show an example for deriving $\mathbf{G}$ matrix component $\mathbf{G}_{xx}$.

$$\begin{aligned}\mathbf{G}_{xx}(\mathbf{r}, \mathbf{r}') =&(\mathbf{I} + \frac{1}{k^2}\nabla_x\nabla_x)\frac{\exp ik|\mathbf{r} - \mathbf{r}'|}{|\mathbf{r} - \mathbf{r}'|} \\ =&(\mathbf{I} + \frac{1}{k}\nabla_x\nabla_x)\frac{\exp ik\mathbf{r}_{12}}{\mathbf{r}_{12}},\end{aligned} \tag{B.12}$$

where $\mathbf{r}_{12} = |\mathbf{r}_1 - \mathbf{r'}_2|$. Then,

$$\begin{aligned}\mathbf{G}_{xx}(\mathbf{r}_{12}) =&\frac{\exp(ik\mathbf{r}_{12})}{\mathbf{r}_{12}} + \frac{1}{k^2}\nabla_x\frac{\partial}{\partial x}\frac{\exp(ik\mathbf{r}_{12})}{\mathbf{r}_{12}} \\ =&\frac{\exp(ik\mathbf{r}_{12})}{\mathbf{r}_{12}} + \frac{1}{k^2}\nabla_x(\frac{1}{\mathbf{r}_{12}}\frac{\partial \exp(ik\mathbf{r}_{12})}{dx} + \exp ik\mathbf{r}_{12}\frac{\partial \mathbf{r}_{12}^{-1}}{dx}).\end{aligned} \tag{B.13}$$

Here,

$$\frac{\partial \exp(ik\mathbf{r}_{12})}{dx} = \frac{ik\mathbf{x}_{12}\exp(ik\mathbf{r}_{12})}{\mathbf{r}_{12}}, \tag{B.14}$$

and

$$\frac{\partial \mathbf{r}_{12}^{-1}}{dx} = -\frac{x_{12}}{r_{12}^3}. \tag{B.15}$$

Then,

$$\begin{aligned}\mathbf{G}_{xx}(\mathbf{r},\mathbf{r}') =&\frac{\exp(ik\mathbf{r}_{12})}{\mathbf{r}_{12}} + \frac{1}{k^2}\nabla_x(\frac{ik\mathbf{x}_{12}\exp(ik\mathbf{r}_{12})}{\mathbf{r}_{12}^2} - \frac{\mathbf{x}_{12}\exp(ik\mathbf{r}_{12})}{\mathbf{r}_1^3})\\ =&\frac{\exp(ik\mathbf{r}_{12})}{\mathbf{r}_{12}} + \frac{1}{k^2}(\frac{\partial}{dx}\frac{ik\mathbf{x}_{12}\exp(ik\mathbf{r}_{12})}{\mathbf{r}_{12}^2} - \frac{\partial}{dx}\frac{\mathbf{x}_{12}\exp(ik\mathbf{r}_{12})}{\mathbf{r}_1^3})\\ =&\frac{\exp(ik\mathbf{r}_{12})}{\mathbf{r}_{12}} + \frac{1}{k^2}(\frac{ik\exp(ik\mathbf{r}_{12})}{\mathbf{r}_{12}^2} + \frac{ik\mathbf{x}_{12}}{\mathbf{r}_{12}}\frac{\partial\exp(ik\mathbf{r}_{12})}{dx}\\ &+ ik\mathbf{x}_{12}\exp(ik\mathbf{x}_{12})\frac{\partial\mathbf{r}_{12}^{-2}}{dx} - \frac{\exp(ik\mathbf{r}_{12})}{\mathbf{r}_{12}^3} - \frac{\mathbf{x}_{12}}{\mathbf{r}_{12}^3}\frac{\partial\exp(ik\mathbf{r}_{12})}{dx}\\ &- \mathbf{x}_{12}\exp(ik\mathbf{r}_{12})\frac{\partial\mathbf{r}_{12}^{-3}}{dx}).\end{aligned} \tag{B.16}$$

Here,

$$\frac{\partial\mathbf{r}_{12}^{-2}}{dx} = 2\frac{\mathbf{x}_{12}}{\mathbf{r}_{12}^4}, \tag{B.17}$$

and

$$\frac{\partial\mathbf{r}_{12}^{-3}}{dx} = -3\frac{\mathbf{x}_{12}}{\mathbf{r}_{12}^5}. \tag{B.18}$$

Finally, we have

$$\begin{aligned}\mathbf{G}_{xx}(\mathbf{r},\mathbf{r}') =&\frac{\exp(ik\mathbf{r}_{12})}{\mathbf{r}_{12}} + \frac{1}{k^2}(\frac{ik\exp(ik\mathbf{r}_{12})}{\mathbf{r}_{12}^2} - \frac{k^2\mathbf{x}_{12}^2\exp(ik\mathbf{r}_{12})}{\mathbf{r}_{12}^3} - \frac{\exp(ik\mathbf{r}_{12})}{\mathbf{r}_{12}^3}\\ &- \frac{3ik\mathbf{x}_{12}^2\exp(ik\mathbf{r}_{12})}{\mathbf{r}_{12}^4} + \frac{3\mathbf{x}_{12}^2\exp(ik\mathbf{x}_{12})}{\mathbf{r}_{12}^5}).\end{aligned} \tag{B.19}$$

Then, we can derive the other 8 components with the same method, as listed below.

$$\begin{aligned}\mathbf{G}_{yy}(\mathbf{r},\mathbf{r}') =&\frac{\exp(ik\mathbf{r}_{12})}{\mathbf{r}_{12}} + \frac{1}{k^2}(\frac{ik\exp(ik\mathbf{r}_{12})}{\mathbf{r}_{12}^2} - \frac{k^2\mathbf{y}_{12}^2\exp(ik\mathbf{r}_{12})}{\mathbf{r}_{12}^3} - \frac{\exp(ik\mathbf{r}_{12})}{\mathbf{r}_{12}^3}\\ &- \frac{3ik\mathbf{y}_{12}^2\exp(ik\mathbf{r}_{12})}{\mathbf{r}_{12}^4} + \frac{3\mathbf{y}_{12}^2\exp(ik\mathbf{y}_{12})}{\mathbf{r}_{12}^5}).\end{aligned} \tag{B.20}$$

$$\begin{aligned}\mathbf{G}_{zz}(\mathbf{r},\mathbf{r}') =&\frac{\exp(ik\mathbf{r}_{12})}{\mathbf{r}_{12}}+\frac{1}{k^2}(\frac{ik\exp(ik\mathbf{r}_{12})}{\mathbf{r}_{12}^2}-\frac{k^2\mathbf{z}_{12}^2\exp(ik\mathbf{r}_{12})}{\mathbf{r}_{12}^3}-\frac{\exp(ik\mathbf{r}_{12})}{\mathbf{r}_{12}^3}\\&-\frac{3ik\mathbf{z}_{12}^2\exp(ik\mathbf{r}_{12})}{\mathbf{r}_{12}^4}+\frac{3\mathbf{z}_{12}^2\exp(ik\mathbf{z}_{12})}{\mathbf{r}_{12}^5}).\end{aligned} \tag{B.21}$$

$$\begin{aligned}\mathbf{G}_{xy}(\mathbf{r},\mathbf{r}') =&\mathbf{G}_{yx}(\mathbf{r},\mathbf{r}')\\=&\frac{\exp(ik\mathbf{r}_{12})}{\mathbf{r}_{12}}+\frac{1}{k^2}(\frac{3\exp(ik\mathbf{r}_{12})\mathbf{x}_{12}\mathbf{y}_{12}}{\mathbf{r}_{12}^5}-\frac{3ik\exp(ik\mathbf{r}_{12})\mathbf{x}_{12}\mathbf{y}_{12}}{\mathbf{r}_{12}}\\&-\frac{k^2\exp(ik\mathbf{r}_{12})\mathbf{x}_{12}\mathbf{y}_{12}}{\mathbf{r}_{12}^3}.\end{aligned} \tag{B.22}$$

$$\begin{aligned}\mathbf{G}_{xz}(\mathbf{r},\mathbf{r}') =&\mathbf{G}_{zx}(\mathbf{r},\mathbf{r}')\\=&\frac{\exp(ik\mathbf{r}_{12})}{\mathbf{r}_{12}}+\frac{1}{k^2}(\frac{3\exp(ik\mathbf{r}_{12})\mathbf{x}_{12}\mathbf{z}_{12}}{\mathbf{r}_{12}^5}-\frac{3ik\exp(ik\mathbf{r}_{12})\mathbf{x}_{12}\mathbf{z}_{12}}{\mathbf{r}_{12}}\\&-\frac{k^2\exp(ik\mathbf{r}_{12})\mathbf{x}_{12}\mathbf{z}_{12}}{\mathbf{r}_{12}^3}.\end{aligned} \tag{B.23}$$

$$\begin{aligned}\mathbf{G}_{yz}(\mathbf{r},\mathbf{r}') =&\mathbf{G}_{zy}(\mathbf{r},\mathbf{r}')\\=&\frac{\exp(ik\mathbf{r}_{12})}{\mathbf{r}_{12}}+\frac{1}{k^2}(\frac{3\exp(ik\mathbf{r}_{12})\mathbf{z}_{12}\mathbf{y}_{12}}{\mathbf{r}_{12}^5}-\frac{3ik\exp(ik\mathbf{r}_{12})\mathbf{z}_{12}\mathbf{y}_{12}}{\mathbf{r}_{12}}\\&-\frac{k^2\exp(ik\mathbf{r}_{12})\mathbf{z}_{12}\mathbf{y}_{12}}{\mathbf{r}_{12}^3}.\end{aligned} \tag{B.24}$$

APPENDIX C: VECTOR FIELD TRANSMITTED BY A LIQUID CRYSTAL CELL

The Jones matrix represents of a liquid crystal cell, i, is given by [82]

$$T_i = R(-\alpha d_i) \begin{bmatrix} e^{-i\beta d_i/2} & 0 \\ 0 & e^{i\beta d_i/2} \end{bmatrix}, \tag{C.1}$$

where $R(-\alpha d_i)$ is a rotation matrix in the form of

$$R(\theta) = \begin{bmatrix} \cos\theta & \sin\theta \\ -\sin\theta & \cos\theta \end{bmatrix}. \tag{C.2}$$

Thus, the Jones matrix is a wave retarder of retardation βd_i with the slow axis along the x direction, followed by polarization rotator of angle θ. The vector field after passing through the liquid crystal cell, i, is given by

$$\begin{aligned} \begin{bmatrix} \boldsymbol{E}_{xi} \\ \boldsymbol{E}_{yi} \end{bmatrix} = T_i \begin{bmatrix} U_{Li} \\ 0 \end{bmatrix} &= R(-\alpha d_i) \begin{bmatrix} e^{-i\beta d_i/2} & 0 \\ 0 & e^{i\beta d_i/2} \end{bmatrix} \begin{bmatrix} U_{Li} \\ 0 \end{bmatrix} \\ &= R(-\alpha d_i) \begin{bmatrix} U_{Li} e^{-i\beta d_i} \\ 0 \end{bmatrix} e^{i\beta d_i/2}. \end{aligned} \tag{C.3}$$

As the input vector field is polarized along the x direction, the liquid crystal cell only introduces a phase shift in the x direction other than in the y direction. By

substituting the rotation matrix,

$$\begin{aligned}
\begin{bmatrix} \boldsymbol{E}_{xi} \\ \boldsymbol{E}_{yi} \end{bmatrix} &= \begin{bmatrix} \cos\theta & \sin\theta \\ -\sin\theta & \cos\theta \end{bmatrix} \begin{bmatrix} U_{Li}e^{-i\beta d_i} \\ 0 \end{bmatrix} e^{i\beta d_i/2} \\
&= \begin{bmatrix} U_{Li}e^{-i\beta d_i} & \cos\theta \\ -U_{Li}e^{-i\beta d_i} & \sin\theta \end{bmatrix} e^{i\beta d_i/2} \\
&= \begin{bmatrix} U_{Li}\cos\theta \\ -U_{Li}\sin\theta \end{bmatrix} e^{-i\beta d_i} e^{i\beta d_i/2} \\
&= \begin{bmatrix} U_{Li}\cos\theta \\ -U_{Li}\sin\theta \end{bmatrix} e^{-i\beta d_i/2} \\
&= \begin{bmatrix} E_{xi} \\ -E_{yi} \end{bmatrix} e^{-i\beta d_i/2}.
\end{aligned} \tag{C.4}$$

Therefore, $\theta = \tan^{-1}\frac{E_y}{E_x}$ is the angle of rotation. Figure below shows the relation between U and E_x and E_y.

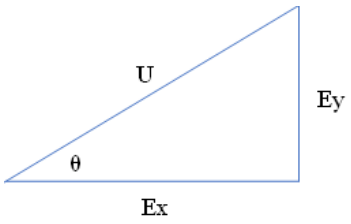

Figure C.1: Relation between U and E_x and E_y.

An additional lens array might be needed to compensate for the difference of phase

shift due to the thickness variations among different liquid crystal cells by

$$\begin{aligned}\begin{bmatrix} E_x \\ E_y \end{bmatrix} &= \begin{bmatrix} E_x \\ -E_y \end{bmatrix} e^{-i\beta d_i/2} e^{-i\beta \Delta d_i/2} \\ &= \begin{bmatrix} E_x \\ -E_y \end{bmatrix} e^{-i\beta (d_i + \Delta d_i)/2}.\end{aligned} \tag{C.5}$$

We can see that the vector field passing through the liquid crystal cells matches the calculated vector fields for realizing a polarized superoscillatory field in the aperture plane in Eq. (3.36). Here, we set orientation angle $\alpha = \alpha + \pi/2$ in the annulus regions of $\boldsymbol{E}_x$ to compensate the π phase shift in the annulus regions of $\boldsymbol{E}_x$.

APPENDIX D: DERIVATION OF A FAR-FIELD CSD

The CSD at distance z is given by substitute Eq. (4.10) into Eq. (4.12),

$$\begin{aligned} W(\mathbf{r}_1,\mathbf{r}_2;z) =& \frac{1}{(\lambda z)^2}\int \sqcap(v)d^{\mathrm{N}}v \\ & \iint S^*(\mathbf{r}_1')S(\mathbf{r}_2')e^{iv\frac{(r_2'^2-r_1'^2)}{\delta_u^2}}e^{-\frac{ik}{2z}(\mathbf{r}_1-\mathbf{r}_1')^2}e^{\frac{ik}{2z}(\mathbf{r}_2-\mathbf{r}_2')}d^2\mathbf{r}_1'^2d^2\mathbf{r}_2' \\ =& \frac{1}{(\lambda z)^2}\int \sqcap(v)d^{\mathrm{N}}v \\ & \int S^*(\mathbf{r}_1')e^{-ivr_1'^2/\delta_u^2}e^{-\frac{ik}{2z}(\mathbf{r}_1-\mathbf{r}_1')^2}d^2\mathbf{r}_1' \\ & \int S(\mathbf{r}_2')e^{ivr_2'^2/\delta_u^2}e^{\frac{ik}{2z}(\mathbf{r}_2-\mathbf{r}_2')^2}d^2\mathbf{r}_2'. \end{aligned} \tag{D.1}$$

For a vortex beam,

$$S(\mathbf{r}) = r^{|m|}e^{im\phi}e^{-r^2/2\sigma_s^2}. \tag{D.2}$$

By substituting Eq. (D.2) into Eq. (4.13),

$$\begin{aligned} W(\mathbf{r}_1,\mathbf{r}_2;z) =& \frac{1}{(\lambda z)^2}\int \sqcap(v)d^{\mathrm{N}}v\int r_1'^{|m|} \\ & e^{-im\phi_1'}e^{-r_1'^2/2\sigma_s^2}e^{-ivr_1'^2/\delta_u^2}e^{-\frac{ik}{2z}(\mathbf{r}_1-\mathbf{r}_1')^2}d^2\mathbf{r}_1' \\ & \int r_2'^{|m|}e^{im\phi_2'}e^{-r_2'^2/2\sigma_s^2}e^{ivr_2'^2/\delta_u^2}e^{\frac{ik}{2z}(\mathbf{r}_2-\mathbf{r}_2')^2}d^2\mathbf{r}_2'. \end{aligned} \tag{D.3}$$

The integral related with $\mathbf{r}_1'$ is expanded with polar coordinates as

$$\begin{aligned} \int f(\mathbf{r}_1')dr_1' =& \iint r_1'^{|m|+1}e^{-im\phi_1'}e^{-r_1'^2/2\sigma_s^2}e^{-ivr_1'^2/\delta_u^2}e^{-\frac{ik}{2z}r_1^2} \\ & e^{\frac{ik}{z}r_1'r_1\cos(\phi_1-\phi_1')}e^{-\frac{ik}{2z}r_1'^2}dr_1'd\phi_1' \\ =& e^{-\frac{ik}{2z}r_1^2}e^{im\phi_1}\int r_1'^{|m|+1}e^{-r_1'^2/2\sigma_s^2-ivr_1'^2/\delta_u^2-\frac{ik}{2z}r_1'^2}dr_1' \\ & \int_0^{2\pi} e^{i(-m)(\phi_1'-\phi_1)}e^{\frac{ik}{z}r_1'r_1\cos(\phi_1'-\phi_1)}d\phi_1'. \end{aligned} \tag{D.4}$$

As $J_n(z) = \frac{1}{2\pi i^n}\int_0^{2\pi} e^{iz\cos\phi}e^{in\phi}d\phi$,

$$\int f(\mathbf{r}_1')dr_1' = 2\pi i^{|m|} e^{-\frac{ik}{2z}r_1^2} e^{im\phi_1} \int r_1'^{|m|+1} e^{-r_1'^2(\frac{1}{2\sigma_s^2}+\frac{iv}{\delta_u^2}+\frac{ik}{2z})} J_{|m|}(\frac{kr_1r_1'}{z})dr_1'. \tag{D.5}$$

Define $\alpha = \frac{1}{2\sigma_s^2} - \frac{iv}{\delta_u^2} - \frac{ik}{2z}$,

$$\int f(\mathbf{r}_1')dr_1' = 2\pi i^{|m|} e^{-\frac{ik}{2z}r_1^2} e^{im\phi_1} \int r_1'^{|m|+1} e^{-\alpha^* r_1'^2} J_{|m|}(\frac{kr_1r_1'}{z})dr_1'. \tag{D.6}$$

As $\int x^{v+1} e^{-\alpha x^2} J_v(\beta x)dx = \frac{\beta^v}{(2\alpha)^{v+1}} e^{-\frac{\beta^2}{4\alpha}}$,

$$\int f(\mathbf{r}_1')dr_1' = 2\pi i^{|m|} e^{-\frac{ik}{2z}r_1^2} e^{im\phi_1} \frac{(kr_1/z)^{|m|}}{(2\alpha^*)^{|m|+1}} e^{-\frac{(kr_1/z)^2}{4\alpha^*}}. \tag{D.7}$$

Similarly, the integral of r_2' is simplified as

$$\int f(\mathbf{r}_2')dr_2' = 2\pi i^{|m|} e^{\frac{ik}{2z}r_2^2} e^{-im\phi_2} \frac{(-kr_2/z)^{|m|}}{(2\alpha)^{|m|+1}} e^{-\frac{(kr_2/z)^2}{4\alpha}}. \tag{D.8}$$

By substituting Eq. (D.7) and Eq. (D.8) into Eq. (D.3),

$$W(\mathbf{r}_1, \mathbf{r}_2; z) = \frac{4\pi^2}{(\lambda z)^2} (\frac{kr_1}{z})^{|m|} (\frac{kr_2}{z})^{|m|} e^{\frac{ik}{2z}(r_2^2 - r_1^2)} e^{im(\phi_1 - \phi_2)} \int \sqcap(v) \frac{1}{(2\alpha^*)^{|m|+1}} \frac{1}{(2\alpha)^{|m|+1}} e^{-\frac{(kr_1/z)^2}{4\alpha^*}} e^{-\frac{(kr_2/z)^2}{4\alpha}} dv. \tag{D.9}$$

APPENDIX E: FAR-FIELD CSD WITH LEVIN METHOD

A Levin method which was developed for numerical integration of functions with oscillatory kernels is implemented for simulating the far-field CSDs derived in Appendix A. Assume the integration is given by

$$I = \int_a^b f(v)w(v)dv = \int_a^b \langle f, w\rangle(v)dv, \tag{E.1}$$

where $f(v)$ is a n-vector non-oscillatory function and $w(v)$ is a n-vector rapidly oscillatory function. The idea of Levin method is to approximate the integrand, $\langle f, w\rangle$, by the derivative of the product of a polynomial function, p, and the oscillatory function, w, as

$$\langle f, w\rangle = \langle p, w\rangle', \tag{E.2}$$

so that the integration is simplified as the difference between the product of p and w at the two boundaries, as

$$I = \int_a^b \langle p, w\rangle'(v)dv = p^t(b)w(b) - p^t(a)w(a). \tag{E.3}$$

To identify the expression of the polynomial function, p, we expand $\langle p, w\rangle'$ as

$$\begin{aligned} \langle p, w\rangle' =& \langle p', w\rangle + \langle p, w'\rangle = \langle p', w\rangle + \langle p, Aw\rangle \\ &= \langle p' + A^t p, w\rangle = \langle f, w\rangle, \end{aligned} \tag{E.4}$$

where assume $w' = Aw$, A is non-rapidly oscillatory and A^t is the transpose of A. Then,

$$p' + A^t p = f. \tag{E.5}$$

Here, we approximate the n^{th} order polynomial $p^{(n)}(v)$ as

$$p^{(n)}(v) = \Sigma_{k=1}^{n} c_k v^k, \tag{E.6}$$

where coefficients, c_k, are determined by the collocation condition of Eq. (E.5):

$$\Sigma_{k=1}^{n} k c_k v_j^{k-1} + A^t \Sigma_{k=1}^{n} c_k v_j^k = f(v_j), \tag{E.7}$$

where $\{v_j\}_{j=1}^{n}$ are distributed in $[a, b]$. Finally, the integral of n-points approximation is

$$I_n = p^{(n)}(b)w(b) - p^{(n)}(a)w(a). \tag{E.8}$$

In this problem, according to Eq. D.9 the non-oscillatory function $f(v)$ is

$$\begin{aligned} f(v) = & \sqcap(v) \frac{1}{(2(\frac{1}{2\delta_s^2} - \frac{iv}{\delta u^2} - \frac{ik}{2z})^*)^{|m|+1}} \\ & \frac{1}{2(\frac{1}{2\delta_s^2} - \frac{iv}{\delta u^2} - \frac{ik}{2z})^{|m|+1}}. \end{aligned} \tag{E.9}$$

The oscillatory function $w(v)$ is

$$\begin{aligned} w(v) = & \exp\{-\frac{(kr_1/z)^2}{4(\frac{1}{2\delta_s^2} - \frac{iv}{\delta u^2} - \frac{ik}{2z})^*}\} \\ & \exp\{-\frac{(kr_2/z)^2)}{4(\frac{1}{2\delta_s^2} - \frac{iv}{\delta u^2} - \frac{ik}{2z})}\}, \end{aligned} \tag{E.10}$$

and

$$\begin{aligned} w'(v) = & \left[\frac{(kr_1/z)^2(i/\delta_u^2)}{4(\frac{1}{2\sigma_s^2} + \frac{iv}{\delta_u^2} + \frac{ik}{2z})^2} - \frac{(kr_2/z)^2(i/\delta_u^2)}{4(\frac{1}{2\sigma_s^2} - \frac{iv}{\delta_u^2} - \frac{ik}{2z})^2}\right] \\ & w(x) \\ & = Aw(x). \end{aligned} \tag{E.11}$$

By substituting A into Eq. (E.7), coefficients c_k can be calculated by solving n linear equations. Finally, $W(r_1, r_2)$ can be calculated by substituting $p^{(n)}(v)$ and Eq. (E.10) into Eq. (E.8).

APPENDIX F: SPECTRAL DENSITY PROFILE WITH NUMERICAL HANKEL TRANSFORM

The spectral density profile $S(\mathbf{r}; z)$ is given by

$$\begin{aligned} S(\mathbf{r}; z) =& \frac{1}{(\lambda z)^2} \iint W_0(\mathbf{r}'_1, \mathbf{r}'_2) e^{-\frac{ik}{2z}(\mathbf{r}-\mathbf{r}'_1)^2} e^{\frac{ik}{2z}(\mathbf{r}-\mathbf{r}'_2)^2} d^2\mathbf{r}'_1 d^2\mathbf{r}'_2 \\ =& \frac{k^2}{z^2} \iint W_0(\mathbf{r}'_1, \mathbf{r}'_2) e^{\frac{ik}{2z}(r'^2_2 - r'^2_1)} J_0(\frac{kr}{z} r'_1) \\ & J_0(\frac{kr}{z} r'_2) r'_1 r'_2 dr'_1 dr'_2. \end{aligned} \tag{F.1}$$

Numerical Hankel transform is applied to calculate $S(\mathbf{r}; z)$. According to Yu [83], a method is developed by approximating the input function by a Fourier-Bessel series over a finite integration interval. Here, we extend the original method from a one-dimensional transformation to a two-dimensional transformation. This method leads to a symmetric transformation matrix for the Hankel transform. The output matrix represents the CSD and diagonal elements represent the spectral density. Zero-order two-dimensional Hankel transforms are

$$f_2(u, v) = 2\pi \iint_0^\infty f_1(x, y) J_0(2\pi x u) J_0(2\pi y v) x y dx dy, \tag{F.2}$$

and

$$f_1(x, y) = 2\pi \iint_0^\infty f_2(u, v) J_0(2\pi x u) J_0(2\pi y v) u v du dv. \tag{F.3}$$

Expand $f_1(x, y)$ and $f_2(u, v)$ by zero-order Fourier-Bessel series and substitute $u = \frac{j_p}{2\pi X}$ and $v = \frac{j_q}{2\pi Y}$, $x = \frac{j_m}{2\pi U}$, and $y = \frac{j_n}{2\pi V}$,

$$\begin{aligned} f_2(\frac{j_p}{2\pi X}, \frac{j_q}{2\pi Y}) =& \frac{1}{\pi U^2 V^2} \sum_{n=1}^{\infty} \sum_{m=1}^{\infty} f_1(\frac{j_m}{2\pi U}, \frac{j_n}{2\pi V}) \\ & J_1^{-2}(j_n) J_1^{-2}(j_m) J_0(\frac{j_n j_p}{S_2}) J_0(\frac{j_m j_q}{S_1}), \end{aligned} \tag{F.4}$$

and

$$f_1(\frac{j_m}{2\pi U},\frac{j_n}{2\pi V}) = \frac{1}{\pi X^2 Y^2}\sum_{q=1}^{\infty}\sum_{p=1}^{\infty} f_2(\frac{j_p}{2\pi X},\frac{j_q}{2\pi Y}) \\ J_1^{-2}(j_q)J_1^{-2}(j_p)J_0(\frac{j_p j_m}{S_1})J_0(\frac{j_q j_n}{S_2}), \tag{F.5}$$

where j_m, j_n, j_p,and j_q are positive roots of the zero-order Bessel function, and $S_1 = 2\pi UX$ and $S_2 = 2\pi VY$. Define

$$F_1(m,n) = f_1(\frac{j_m}{2\pi U},\frac{j_n}{2\pi V})J_1^{-1}(j_m)J_1^{-1}(j_n)XY, \tag{F.6}$$

and

$$F_2(p,q) = f_2(\frac{j_p}{2\pi X},\frac{j_q}{2\pi Y})J_1^{-1}(j_p)J_1^{-1}(j_q)UV. \tag{F.7}$$

Then,

$$f_1(\frac{j_m}{2\pi U},\frac{j_n}{2\pi V}) = F_1(m,n)\frac{J_1(j_m)J_1(j_n)}{XY}, \tag{F.8}$$

and

$$f_2(\frac{j_p}{2\pi X},\frac{j_q}{2\pi Y}) = F_2(p,q)\frac{J_1(j_p)J_1(j_q)}{UV}. \tag{F.9}$$

Substitute Eq. (F.9) into Eq. (F.5) then Eq. (F.6),

$$F_1(m,n) = \frac{4}{S_1 S_2}\sum_{q=1}^{\infty}\sum_{p=1}^{\infty} F_2(p,q) \\ \frac{J_0(\frac{j_p j_m}{S_1})J_0(\frac{j_q j_n}{S_2})}{J_1(j_p)J_1(j_q)J_1(j_m)J_1(j_n)}. \tag{F.10}$$

Substitute Eq. (F.8) into Eq. (F.4) then Eq. (F.7),

$$F_2(p,q) = \frac{4}{S_1 S_2}\sum_{n=1}^{\infty}\sum_{m=1}^{\infty} F_1(m,n) \\ \frac{J_0(\frac{j_n j_p}{S_2})J_0(\frac{j_m j_q}{S_1})}{J_1(j_m)J_1(j_n)J_1(j_p)J_1(j_q)}. \tag{F.11}$$

Define

$$C_{pm} = J_0(\frac{j_p j_m}{S_1}) J_1^{-1}(j_p) J_1^{-1}(j_m), \tag{F.12}$$

and

$$C_{qn} = J_0(\frac{j_q j_n}{S_2}) J_1^{-1}(j_q) J_1^{-1}(j_n). \tag{F.13}$$

Finally, the Hankel transform pairs are expressed by a matrix transformation as

$$F_1(m,n) = \frac{4}{S_1 S_2} \sum_{q=1}^{Q} \sum_{p=1}^{P} C_{pm}^T F_2(p,q) C_{qn}, \tag{F.14}$$

and

$$F_2(p,q) = \frac{4}{S_1 S_2} \sum_{n=1}^{N} \sum_{m=1}^{M} C_{pm} F_1(m,n) C_{qn}^T. \tag{F.15}$$

To implement this method, we simply substitute $f_1 = S^*(r_1')S(r_2')\text{sinc}$ $(\frac{r_2'^2 - r_1'^2}{\delta_u^2}) \exp\{\frac{ik}{2z}(r_2'^2 - r_1'^2)\}$ for circularly coherent beams and $f_1 = S^*(r_1')S(r_2')$ $\exp\{\frac{ik}{2z}(r_2'^2 - r_1'^2)\}$ for coherent beams. For vortex beams of an azimuthal order, M, this method can be extended to the higher order by modifying the transformation matrix as

$$T_{pm} = J_M(\frac{j_p j_m}{S_1}) J_{M+1}^{-1}(j_p) J_{M+1}^{-1}(j_m). \tag{F.16}$$